Award Number: W81XWH-10-2-0101

TITLE: Design, Fabrication, Characterization and Modeling of Integrated Functional Materials

PRINCIPAL INVESTIGATOR: Pritish Mukherjee, Ph. D.

CONTRACTING ORGANIZATION: University of South Florida
Tampa, FL 33620

REPORT DATE: December 2015

TYPE OF REPORT: Final

PREPARED FOR: U.S. Army Medical Research and Materiel Command

Fort Detrick, Maryland 21702-5012

DISTRIBUTION STATEMENT:

   X Approved for public release; distribution unlimited

REPORT DOCUMENTATION PAGE

1. REPORT DATE December 2015	2. REPORT TYPE **Final**	3. DATES COVERED *(09-20-2010 to 09-19-2015)*
4. TITLE AND SUBTITLE Design, Fabrication, Characterization and Modeling of Integrated Functional Materials		5a. CONTRACT NUMBER *W81XWH-10-2-0101*
		5c. PROGRAM ELEMENT NUMBER
6. AUTHOR(S) **PI:** Pritish Mukherjee, Ph. D. **co-PIs:** Hariharan Srikanth, Ph.D.; Sarath Witanachchi, Ph. D.; George Nolas, Ph. D. email: pritish@usf.edu		5d. PROJECT NUMBER
		5e. TASK NUMBER
		5f. WORK UNIT NUMBER
7. PERFORMING ORGANIZATION NAME(S) AND ADDRESS(ES) University of South Florida 4202 East Fowler Avenue Tampa, FL 33620, USA		8. PERFORMING ORGANIZATION REPORT NUMBER
9. SPONSORING / MONITORING AGENCY NAME(S) AND ADDRESS(ES) U.S. Army Medical Research and Materiel Command Fort Detrick, Maryland 21702-5012		10. SPONSOR/MONITOR'S ACRONYM(S)
		11. SPONSOR/MONITOR'S REPORT NUMBER(S)

12. DISTRIBUTION / AVAILABILITY STATEMENT
Approved for public release; distribution unlimited

13. SUPPLEMENTARY NOTES

14. ABSTRACT

The dynamically evolving needs of the U.S. soldier in the battlefield in response to changes in the technology of warfare and associated threats require advances in multiple areas including biomedical diagnostics, chemical sensing, communication technology, efficient power generation without increased payload, and mobile refrigeration. These technological advances are critically dependent on the development of new and currently non-existing materials. This research addresses the directed development of novel materials towards long-term needs of the United States Army. In order to address specific areas of integrated functional materials targeted towards the needs of the U.S. soldier in the field we have initiated research efforts in three main areas which are diagnostics and sensing, communication and energy, and power generation and refrigeration. The specific three independent "Tasks" that have been undertaken are:

Task I: Nanostructured materials for biomedical diagnostics and chemical sensing
Task II: Multifunctional composites for communication and energy applications
Task III: Solid-state materials for power generation and refrigeration
The specific outcome of the research activities is expected to lead to new devices/systems/composite materials useful for the USAMRMC.

15. SUBJECT TERMS
Functional materials, integrated fabrication, nanobiotechnology, multifunctional, dimensional integration, nanocomposites, sensor technology, thermoelectrics, solar cells, photovoltaics, polypeptide multilayer films, multiferroics, biomaterials, biodetection

16. SECURITY CLASSIFICATION OF:			17. LIMITATION OF ABSTRACT	18. NUMBER OF PAGES	19a. NAME OF RESPONSIBLE PERSON USAMRMC
a. REPORT U	b. ABSTRACT U	c. THIS PAGE U	UU	98	19b. TELEPHONE NUMBER *(include area code)*

Design, Fabrication, Characterization and Modeling of Integrated Functional Materials
(Program Director and PI: Prof. Pritish Mukherjee, Department of Physics, USF, Tampa, FL)
(co-PIs: Profs. Hariharan Srikanth, Sarath Witanachchi and George Nolas)

Table of Contents

Page

<u>Design, Fabrication, Characterization and Modeling of Integrated Functional Materials</u>
(Program Director and PI: Prof. Pritish Mukherjee, Department of Physics, USF, Tampa, FL)
(co-PIs: Profs. Hariharan Srikanth, Sarath Witanachchi and George Nolas)

I. Introduction

The dynamically evolving needs of the U.S. soldier in the battlefield in response to changes in the technology of warfare and associated threats require advances in multiple areas including biomedical diagnostics, chemical sensing, communication technology, efficient power generation without increased payload, and mobile refrigeration. These technological advances are critically dependent on the development of new and currently non-existing materials. This research addressed the directed development of novel materials towards long-term needs of the United States Army.

Objective:

In addition to the integration of multiple functionalities with desirable properties (thermal, electrical, magnetic, mechanical, optical, etc.), the connection to real-world applications and devices also requires the seamless integration of dimensions (nano, micro, meso, macro) leading to integrated functional materials. We have initiated this Integrated Functional Materials Project at the Physics Department at the University of South Florida (USF) geared towards precisely addressing this grand challenge of dual integration. A series of targeted projects specifically addressed a spectrum of issues relevant to the needs of the U.S. soldier.

Specific Aims:

The Physics Department at the University of South Florida is home to a unique doctoral program in Applied Physics with an affiliated industrial practicum and nationally recognized research programs in physical and chemical materials synthesis and characterization of bulk materials, thin films and nanomaterials; crystal fiber growth; fundamentals of materials manufacturing processes and computational theoretical materials physics. This research synergistically coalesced existing expertise and leverages research infrastructure at USF in novel bulk materials synthesis, thin film growth, and nanotechnology. These goals were further addressed through multidisciplinary research and new infrastructure development. The basic purpose of this project was to develop the novel science base both in the areas of multi-scale dimensional integration as well as multiple functional integration leading to previously unattained integrated functional materials.

Study Design:

In order to address specific areas of integrated functional materials targeted towards the needs of the U.S. soldier in the field we directed the research efforts in three main areas which are diagnostics and sensing, communication and energy, and power generation and refrigeration. The specific three independent "Tasks", further subdivided into seven "Projects" were:

Task I: Nanostructured materials for biomedical diagnostics and chemical sensing
   (Technical Directors.: Drs. H. Srikanth and P. Mukherjee)
   - *Project 1*   Functional magnetic fluids for biomedical applications
   - *Project 2*   Nanoporous/nano-wire structures and polymer nanotemplates for sensing and molecular manipulation
   - *Project 3*   Carbon-nanotube based sensors
   - *Project 4*   Functional materials for affecting cell proliferation and locomotion

Task II: Multifunctional composites for communication and energy applications
   (Technical Director: Dr. S. Witanachchi)
   - *Project 5*   Tunable multifunctional nano- and heterostructures for RF and microwave applications
   - *Project 6*   Flexible photonic materials for solar-based energy sources

Task III: Solid-state materials for power generation and refrigeration
   (Technical Director: Dr. G. S. Nolas)
   - *Project 7*   High-performance nanofabricated thermoelectric materials for power generation and refrigeration

As described at the beginning of the next section, most of these projects were concluded by September 19, 2013 and the results detailed in the final report for Contract No. W81XWH-07-1-0708 dated October 31, 2013. The remaining milestones that were continued and completed during the approved 24-month no-cost continuation of Contract No. W81XWH-1020101/3349 through September 19, 2015 were:

- Synthesis of PEG, Dextran-coated nanoparticles and clusters for hyperthermia experiments and their structural and magnetic characterization.
- Measurements and comparative analysis of specific absorption rates and AC power losses of ferrofluids for magnetic hyperthermia applications.
- Magnetoimpedance measurements and sensing of biomolecules.
- Formation and delivery of functionalized artificial platelets for rapid cessation of internal bleeding.

These sub-tasks permitted us to continue interdisciplinary work on research towards the development of artificial platelets for delivery to promote coagulation at wound sites. This work relied on advances already made in designed magnetic nanoparticles and physical techniques for the fabrication of polymeric micro- and nano-structures. Supporting work on related magnetic nanostructures also continued as previously reported.

II. Technical Description of Research

This research project was funded initially by Contract No. W81XWH-07-1-0708 from September 20, 2007 to September 19, 2013 (on a one-year no-cost extension) as well as by the overlapping continuation Contract No. W81XWH-10-2-0101 from September 20, 2010 to September 19, 2013. The initial Contract No. W81XWH-07-1-0708 was concluded and a no-cost, two-year extension obtained for the continuation grant X81XWH-10-2-0101 until

September 19, 2015. Technical progress on the conducted research was provided throughout the duration of the grant through quarterly reports, annual reports and two product-line reviews.

Throughout the five-year period of the continuation grant, the following faculty members at the University of South Florida (USF), all Ph.D.s with current ranks noted parenthetically, received partial pay from the research effort: Hari Srikanth (Professor), Sarath Witanachchi (Professor) and Manh-Huong Phan (Research Associate Professor).

The four postdoctoral scientists supported by the grant include: Drs. Eunhee Cho, Anuja Datta, Hafsa Khurshid and Devajyoti Mukherjee.

The following graduate students received support from the grant: Daniel Denmark, Vijaysankar Kalapattil, Zohreh Nemati Porshokouh, Jagannath Devakota, Chaminda Hettiarachchi, Mahesh Hordagoda, Domingo Mateo-Feliciano and Marek Merlak. An undergraduate research student, Daniel Hromalik was also supported by the grant.

The remaining milestones for the extension outlined in the Introduction have been regrouped into two specific Tasks which are:

Task I: *Nanostructured materials for biomedical diagnostics and chemical sensing*
Task II: *Formation and delivery of functionalized artificial platelets for rapid cessation of internal bleeding*

The following discussion provides salient technical details of research performed on each of these Tasks.

Task I: Nanostructured materials for biomedical diagnostics and chemical sensing

The goal of this project has been to synthesize and characterize advanced magnetic nanoparticles and nanocomposites for high-performance sensor and biomedical applications

A. Magnetic nanoparticles for advanced hyperthermia

Magnetic hyperthermia is one of the most promising techniques for cancer treatment. It is based on the fact that magnetic nanoparticles, when subjected to an alternating AC magnetic field, produce a sufficiently high amount of heat to kill cancer cells locally, without damaging healthy cells [1]. In order to reduce the amount of nanoparticles needed for hyperthermia treatment, it is very necessary to provide nanoparticles with the best possible heating efficiency. The heating efficiency of the nanostructures (normally called the Specific Absorption Rate or SAR) is directly related to the area of the hysteresis loop measured in the presence of an AC field, and can be increased by tuning several parameters, such as the nanoparticles' size, saturation magnetization, or the effective anisotropy [2].

Precisely, one of the most promising ways of increasing SAR is through increasing the effective anisotropy by changing the shape of the magnetic nanoparticles. To this respect, Boubeta *et al.* [3] have shown that an improved magnetic response can be achieved in cube-shaped iron oxide nanoparticles, relative to their spherical counterparts. In our case, by using non-hydrolytic thermal decomposition methods, we have been able to synthesize highly crystalline iron oxide magnetic nanoparticles with controlled sizes and shapes.

For the hyperthermia experiments, both AC magnetometry and calorimetric methods were employed. In the calorimetric measurements, the evolution of the temperature for each sample was monitored while applying different AC magnetic fields (0-800 Oe) at a constant frequency (310 kHz). A 4.2 kW Ambrell Easyheat LI 3542 system was employed for these measurements. In order to estimate the SAR, the initial slope $\Delta T/\Delta t$ of each sample was determined. SAR values are derived from the following formula:

$$SAR = Cp \cdot \frac{\Delta T}{\Delta t} \varphi,$$

where φ corresponds with the concentration of magnetic material, C_p is the heat capacity of water, and $\Delta T/\Delta t$ is the initial slope. In AC magnetometry measurements, the SAR was directly determined from the area of the ac hysteresis loops measured durig the hyperthermia experiments. AC magnetometry experiments were performed in collaboration with Dr. E. Garayo and Prof. J.A. García, from the Dept. of Applied Physics at the University of Basque Country (Spain).

Motivated by their biocompatibility and colloidal stability, most research has focused on the use of small (< 20 nm) γ-Fe_2O_3/Fe_3O_4 superparamagnetic nanoparticles [3]. Due to their relatively small magnetic moments, however, it is challenging to obtain a sufficient rise in temperature throughout the entire volume of the tumor. Therefore, we have developed alternative strategies to improve the heating efficiency of the existing magnetic nanomaterials.

Magnetite nano-octopods with tunable sizes

We have focused on the study of magnetite nano-octopods (deformed cubes) for hyperthermia. These octopods show an even better SAR than cubic and spherical nanoparticles, especially in the high AC magnetic field region due to the increased shape anisotropy of nano-octopods compared to their cubic and spherical counterparts.

Iron oxide nanoparticles were prepared using non-hydrolytic thermal decomposition of iron-(III) acetylacetonate (Fe-acac) in the presence of surfactant and Ar+H gas. The mixture of precursor solution and surfactants (Oleic Acid, OA, and Oleylamine, Oy) was heated to 220˚C(nucleation) and kept there for between 30 to 60 minutes depending on the desired size . To obtain different sizes, the amount of precursor and nucleation time were adjusted accordingly. After nucleation the temperature was raised to 300˚C (reflux) in order to give the nanoparticles the desired shape and size. To obtain nano-octopods with sharp edges, the reflux time was kept below 40 minutes. The sample was cooled down to room temperature after reflux and coated with TMAH to make it soluble in water. In Figure 1 we present TEM images of the different sizes of nano-octopods obtained, from 17 to 47 nm.
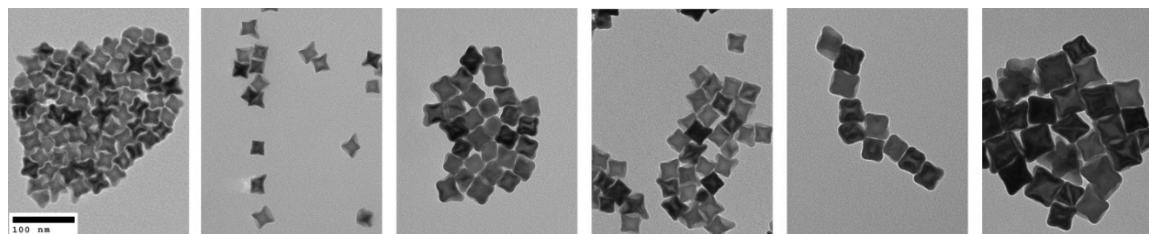

Figure 1: TEM images of different sizes of nano-octopods, from 17 nm (left) to 47 nm (right). All the images are at the same scale.

During the magnetic hyperthermia experiments, it was observed that the heating rate of the nanoparticles tends to increase with increasing nanoparticle size, and the therapeutic regime for hyperthermia treatment (40-45°C) can be easily reached after a few minutes of applying an AC field.
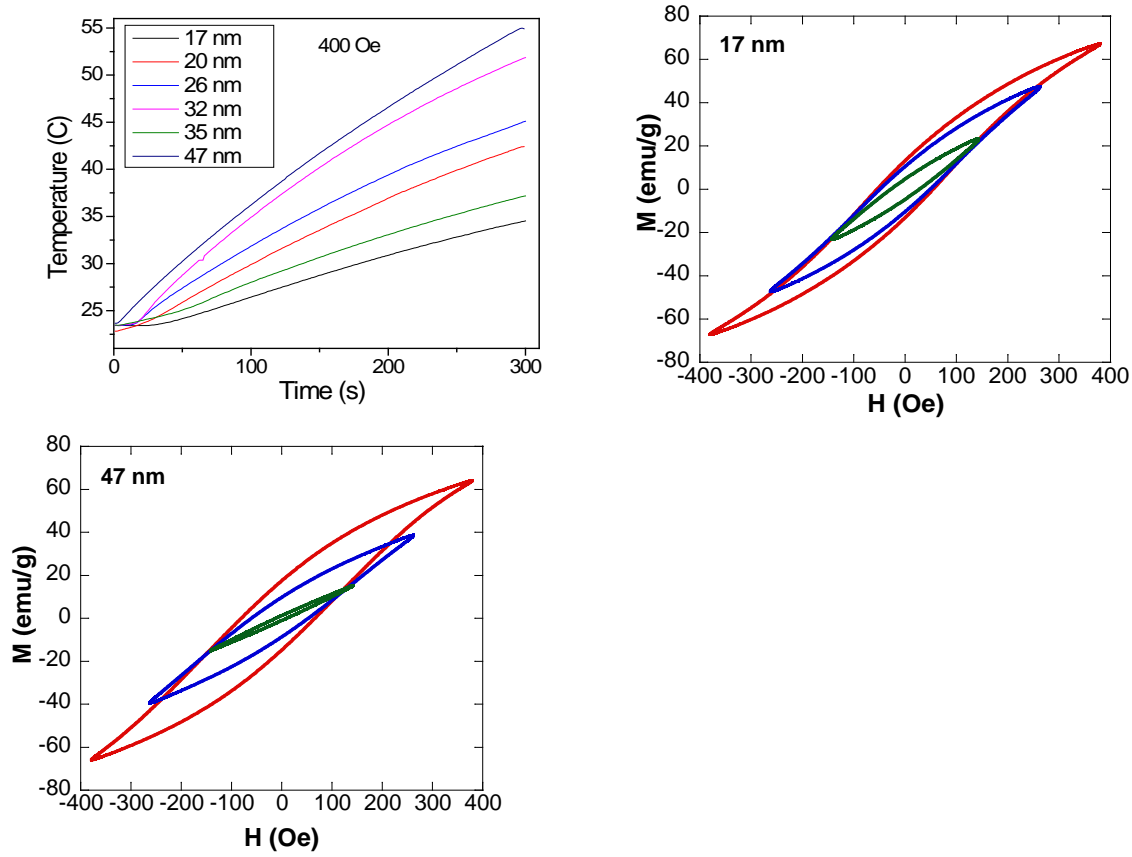
Figure 2: (a) Heating curves for the nano-octopods with different sizes measured at 400 Oe, and AC hysteresis loop measurements at room temperature with different AC fields field for the (b) 17 and (c) 47 nm samples.

Here, the AC hysteresis loops were directly measured using a home-made set-up, while varying the field between 0-400 Oe and keeping the frequency constant at 310 kHz. In this case, SAR is estimated from the hysteresis losses given by the area of the measured AC hysteresis loops, as represented in Figure 2 (b,c) (*SAR = Area* x *frequency*). As can be observed, at low fields (140 Oe) the area of the hysteresis loop is larger for smaller size nano-octopods. As the magnetic field increases, however, the hysteresis loops for the small octopods tend to saturate and keep a narrow shape, while for the bigger ones, it is clear that the coercivity is larger and the final area increases.

A better depiction of the evolution of the heating efficiency as a function of size can be seen in Figure 3. As observed, the SAR changes with increasing size and field, and the obtained values are higher than those reported for similar spheres and octopods (around 20% maximum increase). According to theoretical model developed by Hergt et al. [4], two maxima should be observed in SAR vs. size curves, one smaller for small sizes and a bigger one for bigger sizes. In this study, it has been observed that the evolution of SAR for different sizes of Fe_3O_4 nano-octopods follows a trend similar to that predicted by Hergt *et al.* Figure 3 shows the heating efficiency for different sizes of nano-octopods at different fields. It can be seen in low magnetic

field there are two maxima for SAR values for 20 nm and 32 nm nano-octopods. The heating efficiency for bigger sizes is considerably low. However, as the magnetic field increases, the bigger nano-octopods show a lager heating efficiency compared to smaller particles. This indicates that at low field the 20 nm nano-octopods show the best heating efficiency, while at higher fields the 47 nm nano-octopods have the best SAR.

Overall, we have observed that the heating efficiency of nano-octopods was greater compared to their spherical and cubic nanoparticles due the higher effective anisotropy. The experimentally observed evolution of SAR vs. size confirms for the first time the theoretical predictions proposed by Hergt *et al.* These findings are of great practical importance for tuning the properties of these nanoparticles for a wide range of biomedical applications.
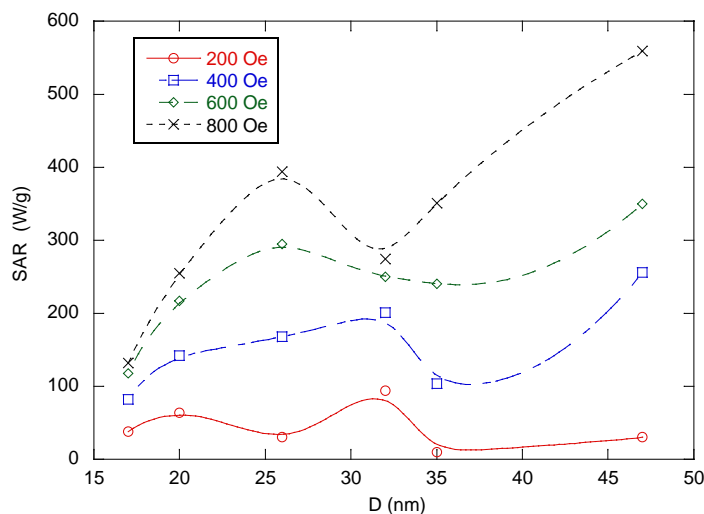

Figure 3: Evolution of SAR vs. size for different magnetic fields.

High aspect ratio magnetite nanorods

1D nanostructures have drawn considerable attention as having anisotropic morphologies due to their high surface to volume ratio, which drastically influences physical and chemical properties. Recently it was demonstrated that anisotropic nanostructures offer enhanced blood circulation time and prolonged retention in the tumour site when compared to spherical nanostructures [5]. However, to the best of our knowledge there are few reports on the synthesis of 1 D Fe_3O_4 nanoparticles [6,7]. And there are no reports on the details of magnetic and hyperthermia response of 1 D magnetite nanostructures. Here we report on the synthesis, magnetic properties, and hyperthermia response of Fe_3O_4 nanorods.

Iron oxide nanorods were synthesized using a previously reported method by Sun et al. [9]. In a typical synthesis 1.2 g of hexadecylamine and 6 mL of oleic acid were mixed in 16 mL of 1-octanol. The above solution was heated to 55 °C and stirred for 30 min to ensure formation of a clear solution. After that, the solution was cooled to room temperature, where 4 mL of iron pentacarbonyl was added and magnetically stirred for another 60 min. Then, the solution was transferred to a 40 mL autoclave with a Teflon lining and heated to 200 °C for 6 h under

autogenous pressure. After cooling to room temperature, the black precipitate was washed with ethanol thrice and transferred to hexane for storing. As-prepared oleic acid-coated iron oxide nanorods were dried in air. 100 mg of dried powder was dispersed in 10 mL ethanol containing 500 mg of tetramethyl ammonium hydroxide (TMAH). The above solution was sonicated for 30 minutes followed by washing with water. After washing the obtained nanorods were dispersed in water.

Characterization: Powder X-ray diffraction was carried out to check the crystalline phase of the material. Figure 4a shows the XRD pattern of Fe_3O_4 nanorods. The XRD pattern revealed the formation of single-phase cubic Fe_3O_4, as indicated by clear peaks. TEM images showed the formation of nanorods with diameter of 7 nm and length of 45-50 nm (Figure 4b). It can be seen from the TEM images that the particles have a very narrow size distribution.
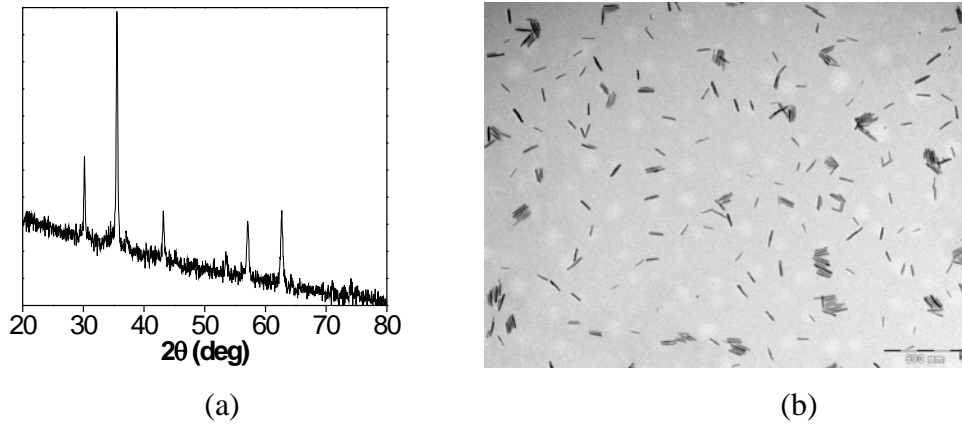

(a)   (b)

Figure 4: (a) XRD pattern and (b) TEM image of as-synthesized Fe_3O_4 nanorods.

Next, we did DC/AC magnetization measurements on the Fe_3O_4 nanorods. Temperature dependence of magnetization, $M(T)$, at an applied field of 20 Oe is shown in Figure 5a. The absence of a bifurcation point of ZFC and FC magnetization and hump in ZFC magnetization indicate that the blocking temperature of nanorods is higher than 325 K. The ZFC and FC magnetization curves showed a sharp change of magnetization at 110 K, which is the signature of the thermally activated first order Verwey transition. The Verwey transition in Fe_3O_4 is related to the structural transition from high temperature cubic to low temperature monoclinic structure. The presence of the Verwey transition in the $M(T)$ curve confirmed the good crystallinity of the Fe_3O_4 nanorods. Both real and imaginary parts of ac magnetization showed peaks at 25 K (not shown here) which could be associated with the competing interaction between magnetocrystalline anisotropy and the surface spin anisotropy of Fe_3O_4 nanorods.
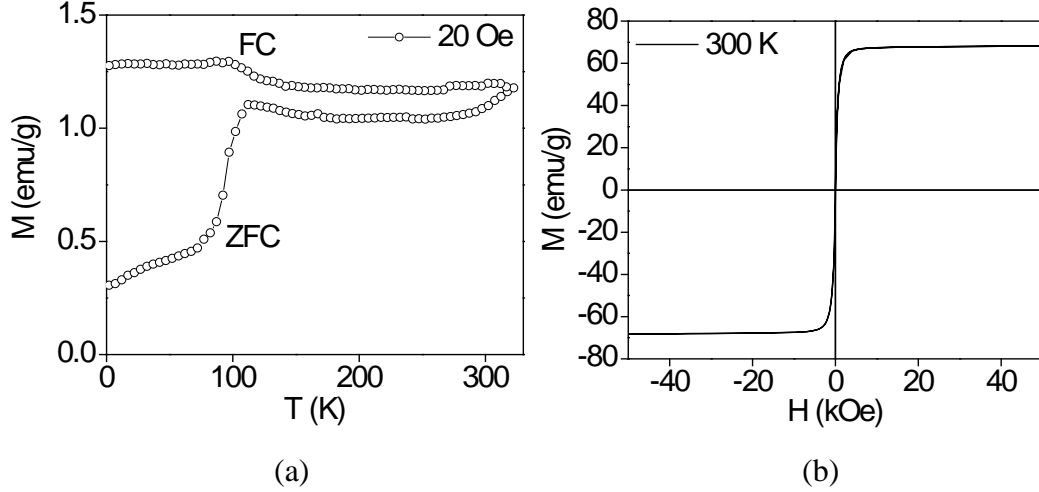
(a)   (b)

Figure 5: (a) Magnetization vs. temperature curve for Fe_3O_4 nanorods recorded in ZFC and FC protocols. (b) Magnetic loop of Fe_3O_4 nanorods at 300 K showing a superparamagnetic characteristic.

A room temperature magnetic hysteresis loop of Fe_3O_4 nanorods is shown in Figure 5b. The hysteresis loops of Fe_3O_4 nanorods at room temperature showed no notable coercivity and the saturation magnetization (M_S) value of ~ 70 emu/g. The high value of M_S is ideal for a wide range of biomedical applications. Our continuing efforts are to characterize magneto-inductive heating responses of these nanorods for possible applications in magnetic hyperthermia based cancer treatment. The high aspect ratio of the nanorods is being modified to optimize the heating effect for this type of material.
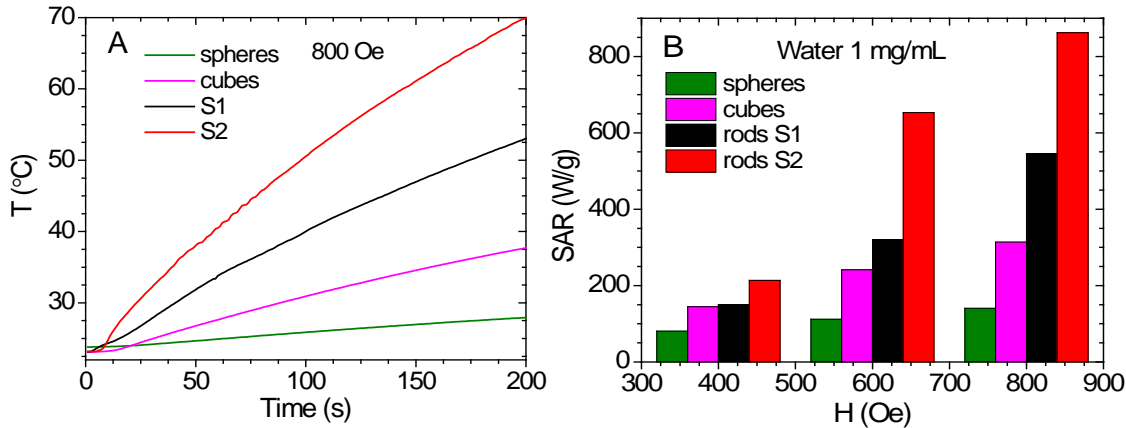
Figure 6: a) Heating curves for the Fe_3O_4 spheres, cubes and nanorods of similar volume (1mg/mL) in water measured at AC field of 800 Oe; b) SAR vs. field plot for the Fe_3O_4 spheres, cubes and nanorods of roughly the same volume (~2000 nm^3).

We have compared the SAR values of two Fe_3O_4 nanorods samples (S1 and S2, with aspects ratio 5 and 11) with those obtained in other forms of Fe_3O_4 nanostructures of similar volume (~2000 nm^3). As can be seen in Figure 6 a) and b), the SAR values of the nanorods (S1

and S2) are greater than those obtained for the spheres and cubes, especially in the high field region (> 600 Oe). At 800 Oe the SAR value is 862 W/g for the nanorods (S2), while it is only about 140 W/g and 314 W/g for the spheres and cubes, respectively. The nanorods yield greater heating efficiency because of their larger saturation magnetization and effective anisotropy, associated with their higher aspect ratio. This once again corroborates that the Fe_3O_4 nanorods are a very promising candidate for magnetic hyperthermia.

Novel exchange-coupled FeO/Fe_3O_4 nanoparticles

Spherical and cubic exchange-coupled FeO/Fe_3O_4 nanoparticles, with different $FeO:Fe_3O_4$ ratios, were prepared and their magnetic and heating properties have been studied systematically. The FeO/Fe_3O_4 nanoparticles were prepared by non-hydrolytic thermal decomposition of iron-(III)acetyleacetonate (Fe-acac), as was described for the nano-octopods.
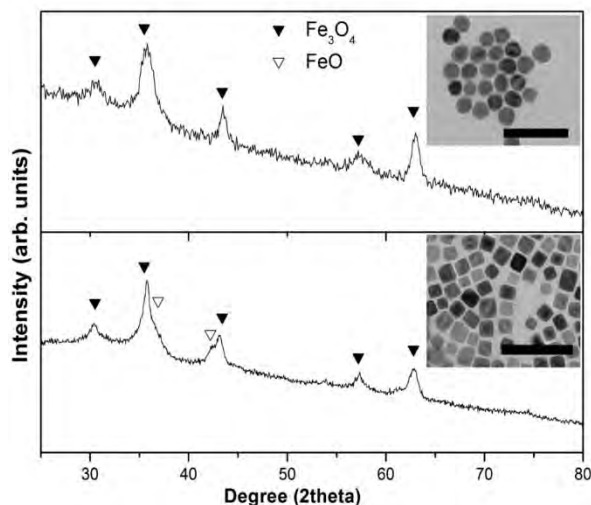
Figure 7: XRD data for the spheres (a) and cubes (b), used in this study. The open symbols represent FeO peaks and closed symbol represent Fe_3O_4 standard reflections. In the insets, TEM image of cubic and spherical particles are presented.

Figure 7 shows the XRD patterns of the FeO/Fe_3O_4 spheres and cubes. For both samples, the major peaks can be assigned to magnetite, while the small shoulders at ~36º and at 42º correspond to the FeO phase, as identified by a graphical X-ray line profile fitting program (XFIT). The FeO peaks are more pronounced for the cubes than for the spheres. In the insets to Figure 7, TEM images of (a) spherical and (b) cubic nanoparticles are presented. It can be seen that in contrast to the spheres, the cubes tend to self-assemble forming chains and similar structures, which modify the effective anisotropy of the system.

Figure 8: a) ZFC-FC curves of the spheres and cubes measured at 50 Oe. Hysteresis loops measured at b) 50 and c) 300 K for both samples. In the inset to b), the shifted hysteresis loop of the cubes after FC at 50 kOe is presented.
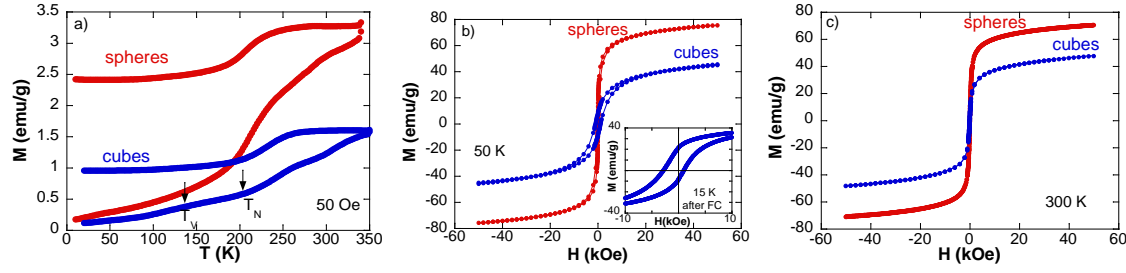
In Figure 8(a), we compare the ZFC/FC M-T curves measured at 50 Oe for the spheres and cubes. As can be observed, the magnetic behavior for both samples is very similar and resembles those reported earlier in similar FeO/Fe_3O_4 systems [8]. The magnetization increases with increasing temperature in the investigated temperature range, and the maximum in the ZFC M-T curve appears to be at $T > 350$ K, indicating that the nanoparticles are in a magnetically blocked state in all our measurements.

Table I: Magnetization, coercivity and normalized remanence at 300 K and 50 K, for cubes and spheres.

	Hc (50K)	Hc (300K)	Ms (50 K)	Ms (300 K)	Mr/Ms (50 K)	Mr/Ms (300K)
Spheres	60	5	75.4	70.7	0.11	0.00
Cubes	1050	60	45.4	47.6	0.21	0.05

Figure 8 (b,c) presents the hysteresis (M-H) loops for both samples at 50 and 300 K, which is below T_V and above T_N, respectively. It can be seen that the cubes have a lower saturation magnetization, M_S, but a higher coercivity, H_C, and a higher normalized remanence Mr/M_S, as compared to the spheres (see Table I). For the spheres, M_S is around 70-75 emu/g, while for the cubes it remains around 45-47 emu/g. As compared to the spheres, the smaller value of M_S for the cubes is consistent with the fact that this sample has a higher FeO/Fe_3O_4 proportion (as revealed by the above XRD analysis), where $M_S = 80$-100 emu/g for Fe_3O_4 nanoparticles and $M_S < 20$ emu/g for FeO nanoparticles. The higher amount of FeO also explains the larger H_C value for the cubes, especially at low temperatures, since an increase in the FeO/Fe_3O_4 interface area yields a higher anisotropic effect and therefore a larger coercivity.
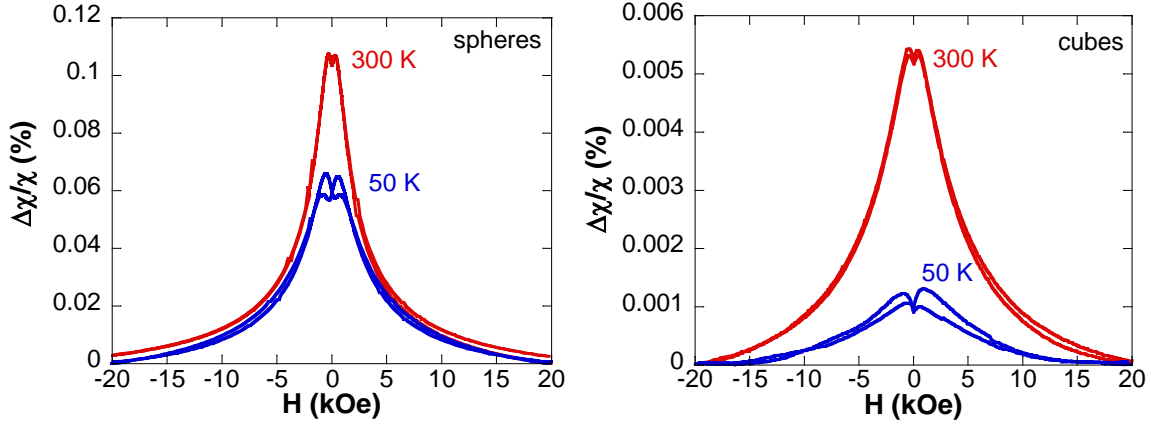
Figure 9: Transverse susceptibility measurements for a) nanospheres and b) nanocubes at 50 and 300 K.

To quantify the effects of effective anisotropy on the magnetic hyperthermia response, we have used a precise, self-resonant tunnel-diode oscillator based transversal susceptibility (TS) technique, which has been proven by us over the years as a direct probe of effective anisotropy fields in a wide range of magnetic materials [9,10]. Details of the technique and related theoretical models have been reported and discussed in our previous work [9].

Figure 9 shows the bipolar TS scans taken at 300 K and 50 K, where the magnetic field is swept first from positive to negative saturation and vice versa. As can be seen, the TS curves present two peaks, corresponding to the effective anisotropy fields ($\pm H_K$), and are quite broadened because of the distribution in particle size and anisotropy fields. At 300 K both TS scans are practically symmetric, and the peak positions (H_K) are determined to be ~295 and ~425 Oe for the spheres and the cubes, respectively. The larger value of H_K for the cubes as compared to the spheres is consistent with the M-H data. At 50 K, the peaks are no longer symmetric and there is a clear difference in peak height. A similar behavior has been observed in Co/CoO exchange-coupled nanoparticles [10], which has been related to the freezing of the magnetic moments of the antiferromagnetic material below T_N, thus inducing an additional anisotropy in the system

Therefore, at room temperature, close to the temperature range desirable for hyperthermia therapy (30 - 50 °C), we obtain: (i) H_k is ~1.5 times larger for the cubes and (ii) M_S is ~1.6 times larger for the spheres. These are expected to have different influences on the SAR of the nanoparticles.

To verify this, we have calculated the SAR values for both samples by using the calorimetric methods. The heating curves are presented in Figure 10 (a). As depicted, with increasing field the heating rate progressively increases. Therefore, by changing the field we can easily reach the desired 40-44°C range, where the cancer cells are more susceptible to heat than healthy ones. It can also be seen that the heating rate is higher for the cubes than for the spheres. This becomes more obvious by comparing the SAR values in Figure 10 (b). In connection with the TS data, we can infer that increasing the effective anisotropy yields a higher value of SAR in exchange-coupled FeO/Fe$_3$O$_4$ nanoparticles with reduced saturation magnetization, demonstrating the importance of magnetic anisotropy in magnetic hyperthermia. To better

evaluate the heating efficiency of the nanoparticles, we have also embedded them in agar dispersions that are known to mimic the higher viscosity of cancer cells, while restricting the physical rotation of the nanoparticles. In the inset to Figure 10 (b) we compare the SAR values obtained for the spheres, when they are in water (green column), and in agar (blue column). As observed, the SAR value decreases a bit (less than 10%) when the spheres are dispersed in agar, indicating a small contribution from the physical rotation of the nanoparticles to the heating efficiency. A similar result has also been obtained for the cubes.
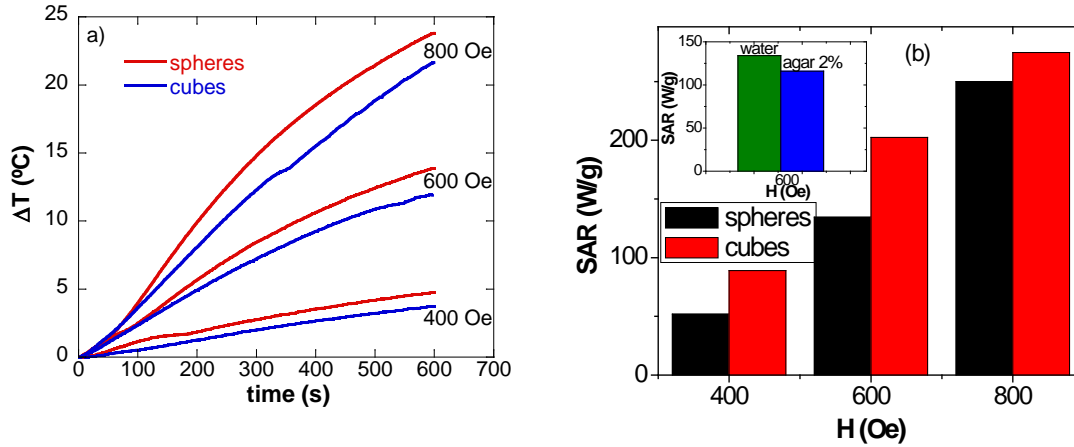

Figure 10: a) Heating curves for the spheres and cubes measured at 310 kHz and H = 400-800 Oe. b) SAR values obtained from the heating curves. In the inset, the SAR values (600 Oe) for the nanospheres in water and in agar are compared.

Novel FeCo nanowires with enhanced heating powers

Theoretical studies have predicted that the use of Fe or FeCo nanoparticles with larger magnetic moments and larger magnetic anisotropy would be more desirable than iron oxide nanoparticles, as the larger values of SAR can be achieved at smaller particle sizes [11,12]. As we saw before, chain-like magnetic nanostructures, such as magnetic nanorods, represent a very promising candidate for enhanced magnetic hyperthermia. Of particular interest, FeCo-based nanowires with high magnetic moments per volume can provide large forces and torques. They can also be electrodeposited in variable size templates ranging from nanometer to micrometer dimensions, thus spanning many relevant biological length scales, and their diameter and length can be independently tuned. Despite these previous studies, the effects of nanowire morphology on the SAR have not been yet investigated in detail.

Therefore, we have performed a systematic study of the effect of varying lengths (2-40 μm) and diameters (100 and 300 nm) on the magnetic and SAR responses of electrodeposited FeCo nanowires. Our study shows that these nanowires are a promising candidate for enhanced magnetic hyperthermia. Here, $Fe_{55}Co_{45}$ nanowires with different lengths (2-40 μm) and diameters (100 and 300 nm) were prepared by electrochemical deposition of Fe and Co in anodized alumina templates. We used commercially prepared AAO templates which had pore diameters of 100 nm (300 nm), an average center to center spacing of ~300 nm (700 nm) between the pores and a template thickness of 50 μm. Before electrodeposition, a 100 nm layer of Cu was sputtered on one side of the template to work as an electrode. The electrolyte

consisted of salts of 0.1 m solutions of $CoCl_2.6H_2O$ and $FeCl_2.xH_2O$ each. The electrodeposition was carried out for 50 minutes at room temperature using a dc voltage at an initial current density of 100 A/m^2 via a graphite electrode. A variation of current density indicates the deposition of Fe and Co within the AAO template. Diluted NaOH and H_2SO_4 were used to adjust the pH of the solution at the desired values. The length of the nanowires can be easily controlled by varying the deposition time. For structural characterization and hyperthermia experiments, the as-deposited nanowires were removed from the template by dissolving the template in a 1M NaOH solution.

Figure 11a shows the XRD micrographs of a typical sample of nanowires after etching out the template. All diffraction peaks correspond to the body-centered-cubic (bcc) FeCo phase. The calculation of crystalline size using Scherrer's formula indicates that these wires are polycrystalline with an average grain size of ~10 nm. A cross-sectional SEM image of an AAO template with arrays of nanowires is shown in Figure 8b. EDS analysis indicated that all samples had 55:45 % Fe:Co atomic ratios. The TEM images of the nanowires (Figure 11b and c) indicate that more than 80% of nanowires retained their original length after dissolving the template.
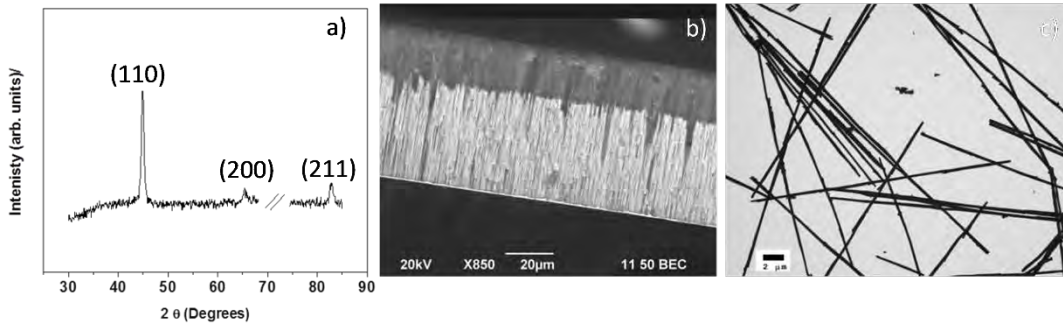

Figure 11: (a) Powder X- ray diffraction of the template-free FeCo nanowires on Si substrate. The (111) crystalline peak from Si wafer has been omitted by inserting a break in the 2 theta angle axis; (b) an SEM cross-sectional view of the FeCo nanowires embedded in the AAO template; and (c) a TEM image of the FeCo nanowires on a Cu grid.

Magnetic hysteresis measurements on the nanowires have revealed that dipolar interactions play an important role in determining the shape of the hysteresis loops and are, therefore, expected to contribute to the heating efficiency of the nanowires. To confirm this, we have studied the magnetic hyperthermia response of these nanowires. We observed that during hyperthermia experiments in water, the nanowires formed self-assembled arrays in the direction of applied fields above 200 Oe, which could be attributed to the effect of dipolar interactions. We present the heating curves for the nanowires in Figure 12a as a function of their length and diameter. With decreasing length and/or diameter of the nanowires, the heating rate decreases, but even for the smallest studied nanowires, 2 μm, their heating rate is still noticeable. As can be seen in the inset of Figure 12a, the obtained SAR values, at 300 Oe and 310 kHz, rapidly increase from 350 to 1500 W/g-$_{Fe3O4}$ when the length increases from 2 to 10 μm, and then the SAR increase slows down, reaching a maximum value of 1510 W/g for the 40 μm sample. On

the other hand, the SAR values decrease by 20% when the diameter is reduced from 300 to 100 nm, but they seem to follow a similar trend. The large values of SAR of the FeCo nanowires result mainly from their large saturation magnetization combined with their shape anisotropy and the effect of dipolar interactions between the FeCo nanowires. The dependence of SAR on wire length is mainly of magnetostatic origin (shape anisotropy). The saturation trend of SAR with wire length (inset of Figure 12a) might be correlated with the wire demagnetization factor's dependence on length and with the length at which two domains may appear along the length.
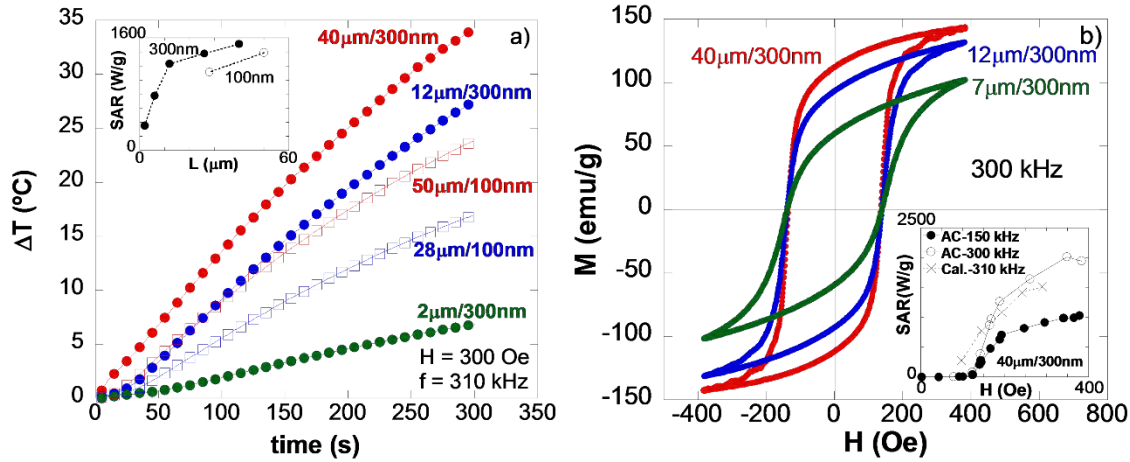
Figure 12: M-H curves as a function of (a) the length and (b) the diameter of the FeCo nanowires inside the AAO templates and aligned parallel to the magnetic field. The inset of (a) shows the coercivity as a function of the length, while the inset of Figure (b) shows the M-H loops measured in the parallel and perpendicular directions of the applied field.

To further probe the effect of wire alignment on the heating efficiency, we have embedded the nanowires in a 2%$_{weight}$ agar solution. This method enabled us to restrict the physical movement of the nanowires while simulating the viscosity of cancer cells. Figure 13 displays the SAR values obtained for the 40 and 2 μm nanowires with different configurations. As observed, for the largest nanowires, the SAR value slightly decreased (by 7%) as the nanowires were aligned with the magnetic field in agar, whereas a drastic reduction in SAR (by 40%) was observed as the nanowires were randomly oriented. This indicates that (i) the SAR is maximized when the nanowires are aligned in the direction of the field, and (ii) the physical movement contribution of the nanowires to the SAR is relatively small. On the other hand, reducing the size of the nanowires was found to result in a greater decrease in SAR (by 25%) for the aligned nanowires. This can be associated with a better alignment of the larger nanowires, as well as their stronger dipolar inter-wire interactions.

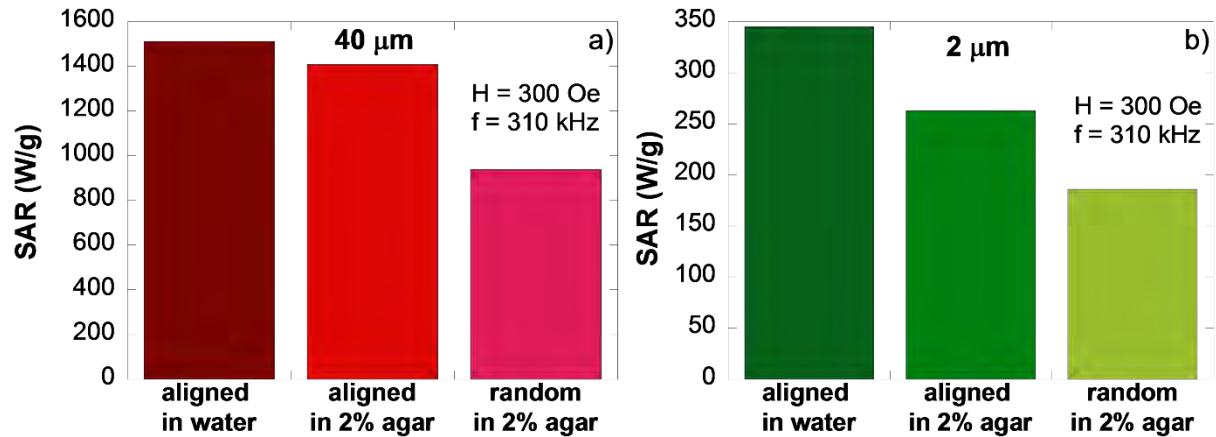Figure 13: SAR values for (a) the 40 μm and (b) 2 μm FeCo nanowires, when dispersed in water, or in a 2% weight agar solution with different orientations.

Surface-functionalized iron oxide nanoparticles

While magneto-inductive heating experiments have been extensively performed on Fe_3O_4 nanoparticles, a clear understanding of the effect of biomaterial coating on the inductive heating efficiency of these particles has remained elusive. Therefore, we have performed a systematic study of the magnetic hyperthermia response of surface-functionalized Fe_3O_4 nanoparticles. Here we have compared the heating efficiency of three samples (PLA-PEG coated Fe_3O_4 NPs; PLA-PEG-Cur coated Fe_3O_4 NPs; OCMCs-folate coated Fe_3O_4 NPs) as a function of the applied field and the concentration. We have also investigated the effect of embedding the nanoparticles in a viscous medium.

Fe_3O_4 nanoparticles were synthesized by the co-precipitation method. The nanoparticles were encapsulated by *O*-Carboxyl methylchitosan. The nanoparticles were then coated with PLA-PEG and finally Curcumin was loaded on them. The samples were provided by our collaborator (Prof. Phuc's research group in Vietnam).

Magnetic hyperthermia responses of the nanoparticles synthesized above are collected and we show here some of the representative results. It can be seen in Figure 14 (a,b) that the heating efficiency increases with an increase in the AC magnetic field. The curves are typical for this kind of material. The heating efficiency decreases with increasing concentration of the nanoparticles. SAR reached a maximum of ~220 W/g for an AC field of 800 Oe. These values are comparable with those reported for small spherical Fe_3O_4 nanoparticles. However, we note that in our case the nanoparticles were coated with different biomaterials, which are more desirable for applications in nanomedicine.
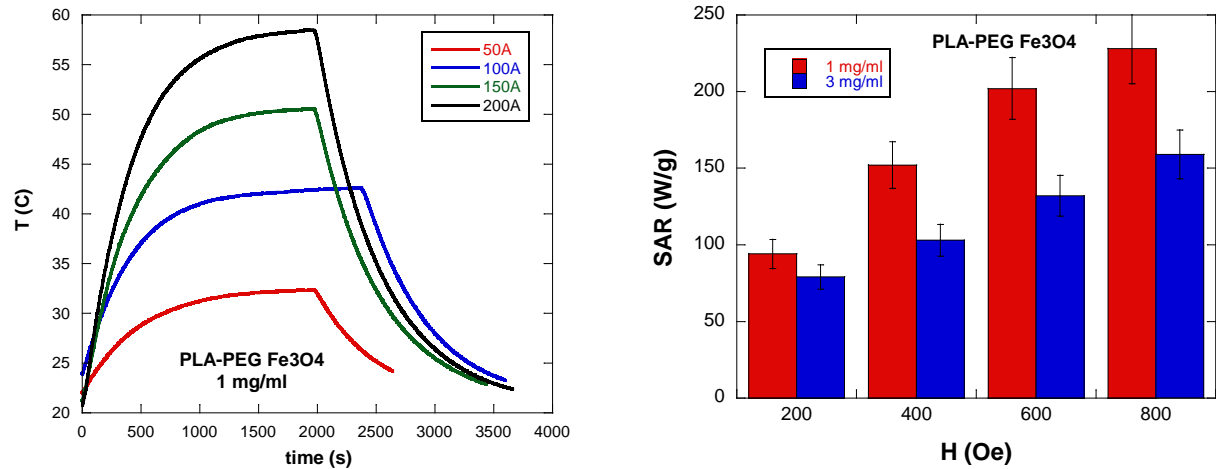
Figure 14: (a) Heating curves for the PLA-PEG coated Fe_3O_4 nanoparticles for different AC fields; (b) SAR values of the same sample for different applied AC fields.

We have also analyzed the time it takes for the heating curves to saturate. As can be seen, after ~15 min (Figure 2a) the temperature is close to saturation.
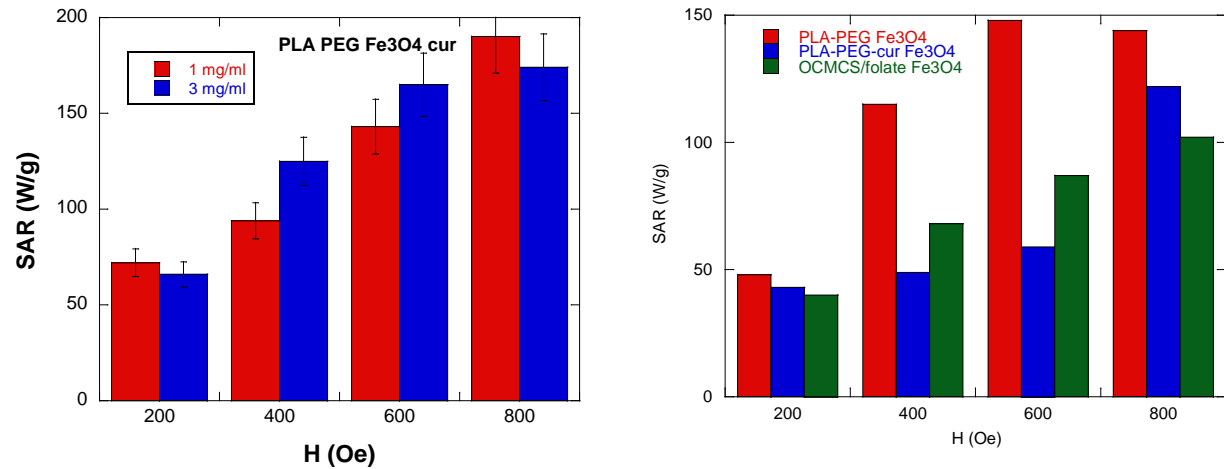
Figure 15: (a) SAR values of the PLA-PEG-Cur coated Fe_3O_4 nanoparticles for different AC fields; (b) SAR values of three different types of nanoparticles for different applied AC fields.

For PLA-PEG-Cur coated Fe_3O_4 nanoparticles, we have observed that the SAR values appreciably increase with AC magnetic field (Figure 15a). The largest SAR value was achieved to be ~190 W/g for an AC field of 800 Oe. The differences between the two concentrations analyzed here are within the error. This contrasts with the previous sample, for which the differences in concentration were more remarkable. The obtained SAR values are also slightly smaller than in the previous case, which is expected. For OCMCs-folate coated Fe_3O_4 nanoparticles, we note that while the SAR values increase as a function of the applied field, there is not much difference in the heating efficiency as a function of the concentration. The best SAR values are obtained for the sample with the lowest particle concentration. The SAR steadily increases up to 140 W/g with increasing applied field (Figure 15b). The SAR values are smaller

than those of the previous samples. We have also put the samples in 2% agar instead of water. By doing so, the medium becomes viscous and the physical rotation of the nanoparticles becomes restricted. With this, we could emulate the higher viscosity conditions of cancer cells in comparison with water. We have observed only a slight decrease in the SAR value (15%). This means that the contribution of physical rotation to the heating of these nanoparticles is not dominant, which is desirable for such applications.

Overall, we have demonstrated the different impacts of biomaterial coating on the magnetic heating efficiency of Fe_3O_4 nanoparticles. The effect of particle motion on the heating capacity is not significant. These findings are of practical importance in manipulating the properties of these nanoparticles for a wide range of biomedical applications.

Multifunctional $MnFe_2O_4$/graphene oxide nanostructures

Manganese doped ferrite nanoparticles (NPs) exhibit magnetic properties (high susceptibility and magnetization) ideal for biomedical applications such as contrast agents for magnetic resonance imaging (MRI), or drug delivery/magnetic hyperthermia agents [13]. On the other hand, graphene oxide (GO) is a two dimensional material with great application potential [14]. Its large specific surface area is ideal for the immobilization of a large number of substances, including biomolecules, drugs, and nanoparticles. It has been found that sheets of graphene oxide are apparently biocompatible without obvious toxicity, and very promising for applications such as drug delivery. This has led to an increasing interest in the realization of hybrid GO-NPs composed of magnetic nanoparticles attached to the surface of nanosheets of graphene oxide. For example, Bai et al. [15] have recently analyzed the heating efficiency of Fe_3O_4 nanoparticles deposited onto graphene oxide sheets for magnetic hyperthermia applications. In this context, we have performed the first study of the magnetic heating capacity and biodetection of $MnFe_2O_4$/graphene oxide nanostructures, which are expected to be very a promising candidate for advanced biomedical applications. We report below some of the main results from this study.

$MnFe_2O_4$ nanoparticles were decorated on the GO nanosheets by the co-precipitation method. Briefly, 5.41 g (0.02 mol) $FeCl_3 \cdot 6H_2O$ and 1.99 g (0.01 mol) $MnCl_2 \cdot 4H_2O$ were dissolved in the water and stirred under air in 10 min. The resulting mixture was mixed with GO suspension (0.6 mg/mL) while stirring for 30 min. Next, 20 mL of 0.5 M NaOH solution was added slowly to the solution of complex. The color of solution changed immediately from orange to dark brown after addition of NaOH indicating the formation of superparamagnetic $MnFe_2O_4$ nanoparticles. The precipitation reaction was then stirred at temperature about 80 C for 2 hours. The product of $MnFe_2O_4$-GO nanocomposite was separated from solution by external magnetic field and washed several times by deionized water and acetone.
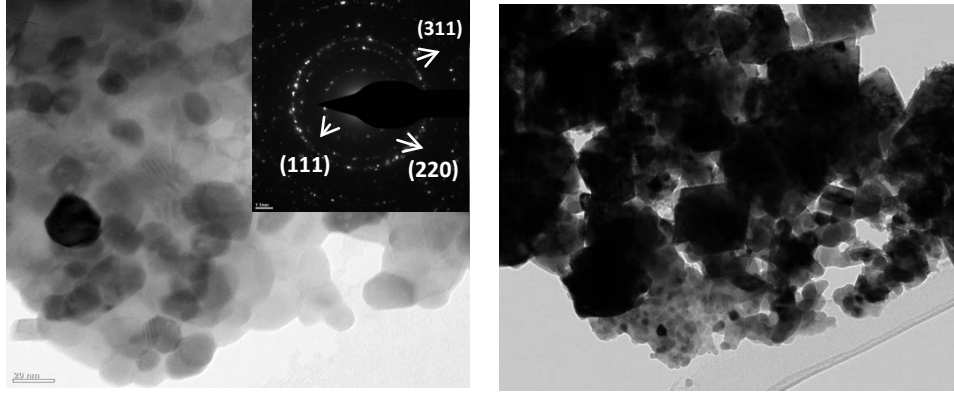
Figure 16: Bright field TEM images of the (a) $MnFe_2O_4$ nanoparticles and the (b) $MnFe_2O_4$ nanoparticles attached to the graphene oxide nanosheets. SAED image of the $MnFe_2O_4$ nanoparticles is shown in the inset of (a).

Bright TEM images (Figure 16 (a,b)) indicate the polyhedral nanoparticles, with elongated shape, and an average size of 12±2 nm. The cubic spinel ferrite structure of the nanoparticles was clearly reflected in the selected-area electron diffraction (SAED) patterns taken using TEM (inset of Fig 1(a)). The lattice spacing was measured to be approx. 0.25 and 0.3 nm, corresponding to the spacing of the (311) and (220) lattice planes. After the precipitation reaction, the nanoparticles are anchored to the surface of the GO nanosheets. All the XRD peaks were indexed as cubic spinel ferrite structure of $MnFe_2O_4$ (Jacobsite; JCPDS no. 10–0319).

The room temperature hysteresis loops measured for the $MnFe_2O_4$ nanoparticles, without and with graphene oxide, are plotted in FIGURE 2, after being normalized by the total sample mass (including also graphene oxide mass). Nearly zero coercivity and remanence are observed in the samples at 300 K, suggesting that the NFO nanoparticles exhibit SPM-like behavior at room temperature. To confirm this, we have fitted our hysteresis loops with a standard Langevin expression + a paramagnetic contribution:

$$M(H) = M_S \int_0^\infty L\left(\frac{\mu H}{k_B T}\right) f(D) dD + \chi H,$$

where D is the diameter of the nanoparticles, $f(D)$ corresponds with a Log-Normal size distribution, and $L(x) = \cotanh(x)-1/x$. χ corresponds with the susceptibility of the paramagnetic contribution. As can be seen in Figure 17(a,b), the fittings for $MnFe_2O_4$ and $MnFe_2O_4$+GO at 300 K are very good, although the apparent size obtained from the fittings is a little bit smaller than expected, if we compare these results with the size distribution previously obtained by TEM. In addition, it can be observed that for the $MnFe_2O_4$+GO sample, there is a noticeable increase of the high field slope due to the additional paramagnetic contribution (10% as seen in Table 1). This could be in principle attributed to the graphene oxide.
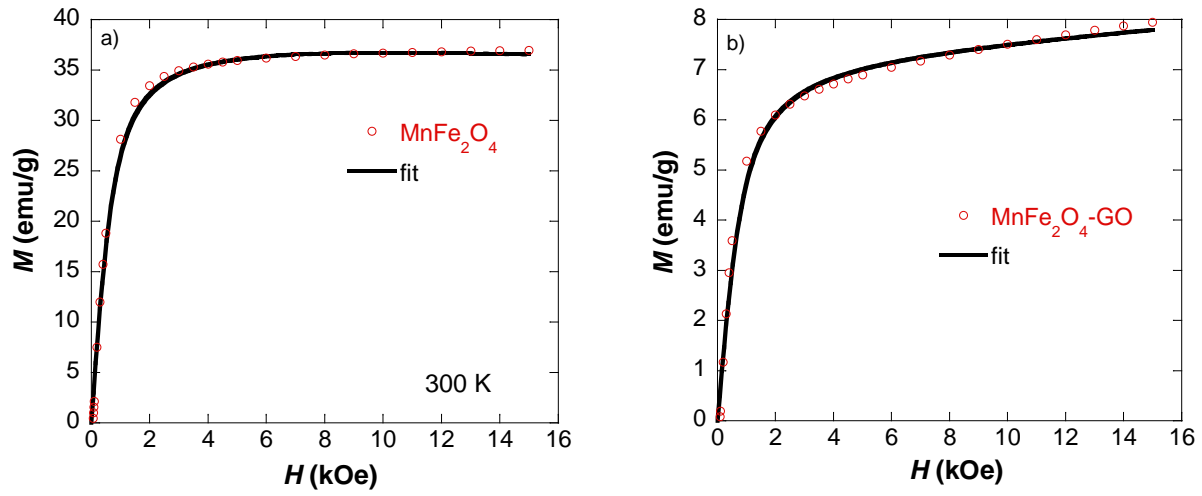
Figure 17: Room temperature hysteresis loops measured for the $MnFe_2O_4$ (a) and the $MnFe_2O_4$-GO (b) samples.

In order to perform the hyperthermia experiments, we prepared two samples, $MnFe_2O_4$ and $MnFe_2O_4$+GO, with the same concentration of magnetic nanoparticles: 1 mg/ml. To determine the mass concentration of $MnFe_2O_4$ NPs in the $MnFe_2O_4$+GO sample (~20%), the saturation magnetization values obtained from the previous magnetic measurements were used. The heating curves are presented in Figure 18.
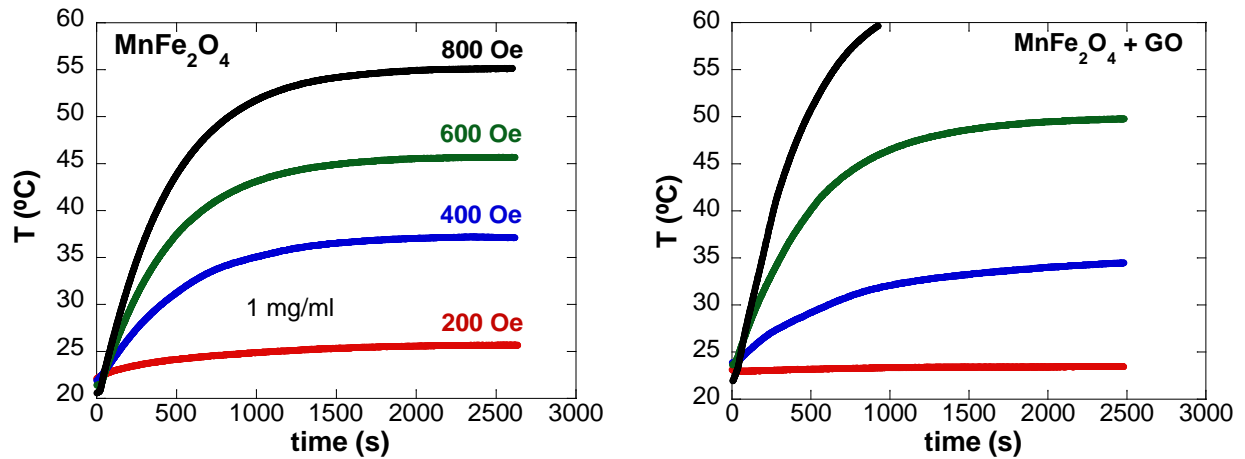
Figure 18: Heating curves for (a) $MnFe_2O_4$ and (b) $MnFe_2O_4$-GO nanoparticles at different fields $200 <, H < 800$ Oe and $f = 310$ kHz.

As can be seen, by changing the intensity of the applied field, the final reached temperature can be controlled, and the desired 40-44ºC range, where the cancer cells are more susceptible to heat than healthy ones, can be easily reached. It must be noted that the hyperthermia measurement at 800 Oe for the $MnFe_2O_4$+GO sample was stopped when reaching 60ºC, since our temperature probe calibration is no longer valid above 60ºC. It can also be seen

that the heating rate at this field for the MnFe$_2$O$_4$+GO sample increases appreciably. This becomes more obvious by comparing the SAR values in Figure 6.
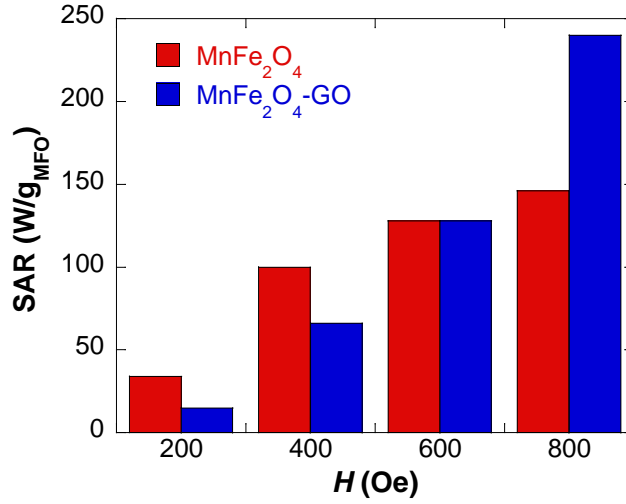
Figure 19: SAR vs field for the MnFe$_2$O$_4$ and the MnFe$_2$O$_4$-GO samples.

The SAR values have been derived from the following formula:

$$SAR = Cp \cdot \frac{\Delta T}{\Delta t} \phi \qquad (2)$$

where ϕ corresponds with the concentration of magnetic material, Cp is the heat capacity of water, and $\Delta T/\Delta t$ is the initial slope of the heating curves. The obtained SAR values are comparable with those reported for similar nanoparticle concentrations. As observed, the SAR vs H behavior tends to saturate in the case of the MnFe$_2$O$_4$ sample, while it keeps increasing for the MnFe$_2$O$_4$+GO sample.

From core/shell to hollow Fe/γ-Fe$_2$O$_3$ nanoparticles

Fe/Fe oxide core/shell nanoparticles are a very promising candidate material for a wide range of biomedical applications because the high magnetization of the core (Fe) and the chemical stability and biocompatibility of the shell (Fe oxide). An interesting byproduct of these systems is the exchange coupling across the core-shell interface that is frequently seen in the form of exchange bias (EB), a horizontal shift in the hysteresis loop [16]. The exploration of EB on core-shell nanoparticles has shown a promising approach to overcoming the superparamagnetic limit in nanoparticles, a critical bottleneck for magnetic data storage application. It has also been noted that in a core/shell nanoparticle the oxidization-driven migration of atoms from the core to the shell is likely to occur (via the so-called Kirkendall effect), thus producing vacancies at the core/shell interface that gradually coalesce into void to form the structure of core/void/shell or hollow nanoparticles [17,18]. We have performed the

first systematic study of the evolution of the static and dynamic magnetic properties including EB as the Fe/γ-Fe_2O_3 core/shell nanoparticles become core/void/shell and hollow, for two different sizes of 12 and 8 nm. We report here some of the main results from this study.

Fe/γ-Fe_2O_3 core/shell nanoparticles were synthesized by thermal decomposition of organometallic compounds, details of which have been reported in our previous work [19]. The microstructure of the samples synthesized was characterized by X-ray diffraction (XRD) and transmission electron microscopy (TEM). The XRD pattern shows the expected phases corresponding to those of Fe and γ-Fe_2O_3. Figure 20(a-c) shows conventional bright-field TEM images of the 12 nm core/shell, core/void/shell, and hollow nanoparticles, along with a representative histogram of the particle size. HRTEM images reveal the crystalline structure of both core and shell (Figure 20d,e). The Fe core is single crystalline, however, the shell of γ-Fe_2O_3 is composed of small crystallites, which are oriented randomly, as described in Figure 20(f). It is the formation of this structure that results in the complex magnetic behavior in this type of material.
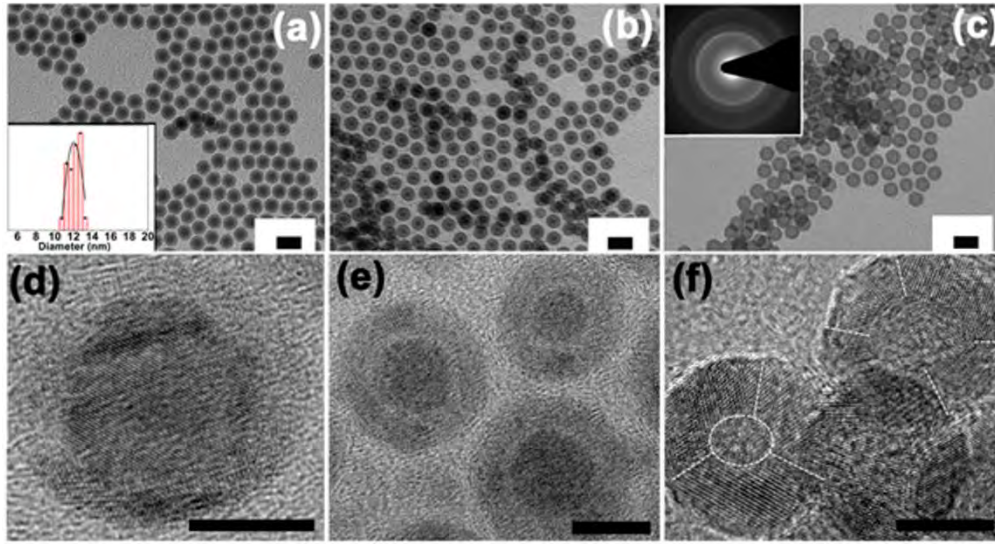
Figure 20: Bright-field TEM images of the 12 nm Fe/γ-Fe_2O_3 (a) core/shell, (b) core/void/shell, and (c) hollow nanoparticles; Inset of Figure 1(a) shows a histogram of the particle size populations for the 12 nm core/shell nanoparticles and inset of Figure 1(c) shows SAED pattern of hollow nanoparticles. HRTEM images of (d) core/shell, (e) core/void/shell and (f) hollow nanoparticles. The scale bar is 20 nm in Figure (a-c) and is 5nm in Figure (d-f). The discontinuous lines in 'f' shows grain boundaries of nanograins in hollow nanoparticles.

Figure 21(a) shows the M-H loops measured at 5 K under the FC (50 kOe) protocol. As observed, the M-H loops are shifted along both the horizontal and vertical directions. Figure 21 (b,c) shows the temperature dependence of the coercivity, H_C, and the EB field, H_{EB}, for the three samples after field cooling in 50 kOe. It can be observed that for all the samples both H_C and H_{EB} progressively decrease with increasing temperature. H_{EB} becomes close to zero above ~30 K, while H_C is still non-zero above this temperature. This indicates that for the three samples, below ~30 K, surface and interface atoms at the shell start to freeze, as supported by the increase in coercivity, behaving as pinning centers for the development of EB. This is also confirmed by the increase in the vertical shift of the hysteresis loops (Figure 21d). However, the hollow nanoparticles present a much larger EB, reaching values of ~7 kOe at low temperatures.

This indicates that the coupling between the central and surface atoms in each nanograin, together with the strong anisotropies and big size distribution of the nanograins in this shell, give rise to a remarkable EB effect that is not observed in the case of the core/shell and core/void/shell nanoparticles having a thinner shell. Therefore, the hollow nanoparticles are very promising for applications in EB-based spintronic devices and that the shell thickness is crucial in order to tune the EB effect in these systems.

Overall, we have systematically investigated the magnetic properties of Fe/γ-Fe$_2$O$_3$ core/shell nanoparticles and their transformation to core/void/shell and hollow morphologies. We have demonstrated the possibility of tuning the magnetic properties including the exchange bias effect in these nanostructures by tuning their morphology. We are in process of diluting such nanoparticles in a non-magnetic polymer matrix or coating the nanoparticles with a non-magnetic SiO$_2$ layer, in order to investigate the effect of dipolar inter-particle interactions on the magnetization dynamics and hence the EB in these nanostructures. A comprehensive understanding of these effects is essential to manipulate the magnetic functionality of these nanostructures for a wide range of biomedical applications.
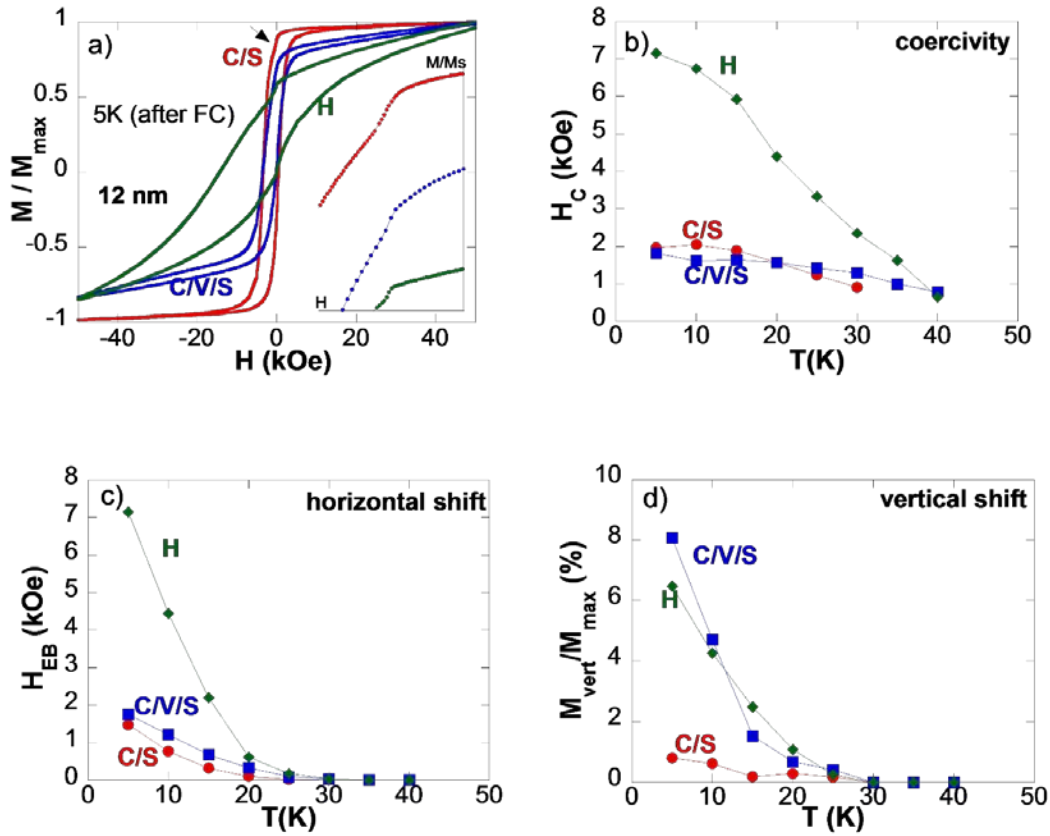
Figure 21: (a) Normalized M-H loops measured at 5 K under FC protocol, and the temperature dependence of the coercivity (b), the horizontal shift (c) and the vertical shift (d), for the 12 nm core/shell, core/void/shell and hollow nanoparticles. A zoom-in of the hysteresis loops region exhibiting the "jump" is shown in the inset of (a).

B. Magnetoimpedance-based biodetectors

The giant magnetoimpedance (GMI) effect of soft ferromagnetic materials has been proposed as a promising approach for magnetic biosensing of magnetically tagged bioanalytes [20-22]. The biosensors operate at room temperature and have ultrahigh sensitivity (detectable fields, ~100 pT), high thermal stability, high spatial resolution, low power consumption, and low cost [23]. We have developed a novel class of magnetic biosensors using the GMI effect of a micro-hole patterned ferromagnetic amorphous ribbon and demonstrated its high capacity for the detection of bovine serum albumen (BSA) proteins tagged to $Fe_3O_4@SiO_2@Au$ magnetic nanoparticles. We report below some of the main results from this study.
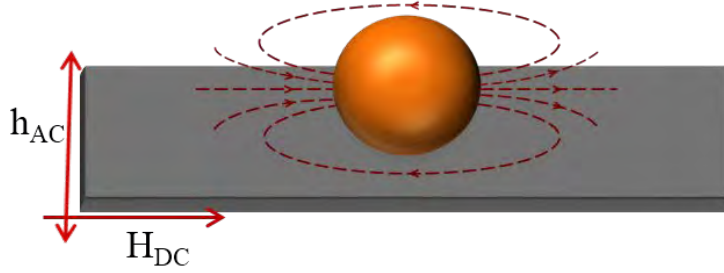
Figure 22: Schematic to demonstrate the working principle of a ribbon based GMI biosensor

The biosensors rely on the stray fields of the sensed magnetized nanoparticles to change the GMI ratio of a sensing element (in our study, it is a magnetic ribbon) for detection of cancer cells and biomolecules [20-22]. When a magnetic marker is present on the surface of the ribbon, it becomes magnetized and behaves as a magnetic dipole producing a stray field (Figure 22). Therefore the ribbon experiences a different resultant magnetic field and reaches a different permeability value, μ'_T, giving rise to a net GMI ratio. This allows us to evaluate the presence of the magnetic marker and hence the bioanalytes tagged to it by considering the difference between the GMI ratios of the ribbon with and without the magnetic marker. The GMI detection sensitivity is defined as the difference between their maximum values (at the anisotropy field, H_k) for the test sample (TS) and reference sample (ref), which is calculated as

$$\Delta\eta = [\frac{\Delta Z}{Z}]_{max,TS} - [\frac{\Delta Z}{Z}]_{max,ref} \, ,$$

where $[\frac{\Delta Z}{Z}]_{max}$ is the maximum values of the GMI ratio which is given as

$$\frac{\Delta Z}{Z} = \frac{Z(H) - Z(H_{sat})}{Z(H_{sat})} \times 100\%,$$

where H_{sat} is the minimum DC magnetic field along the length of the GMI element necessary to saturate its impedance.

Microhole-patterned GMI biosensor
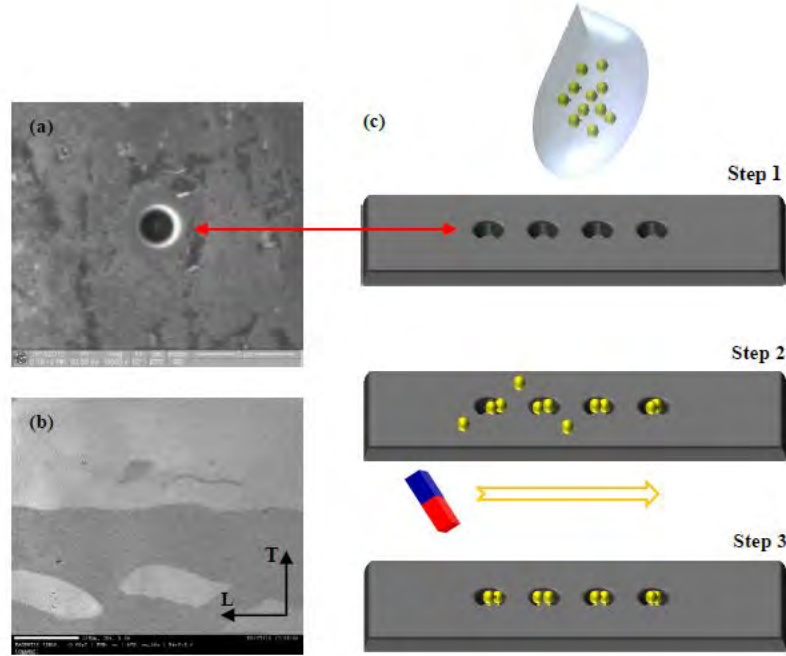
Figure 23: (a) SEM image of a microhole-patterned ribbon, (b) magnetic domain structure, and (c) schematic of a ribbon-based MI sensor element with magnetic markers drop-casted on its surface. Three major steps for each biodetection measurement.

The MI sensor probe was fabricated by using a $Co_{65}Fe_4Ni_2Si_{15}B_{14}$ ribbon. The ribbon was cut into the pieces of dimensions 20 mm × 2 mm × 0.015 mm, cleaned with ethanol and DI water followed by air jet flow. The central region of 9 mm of each piece was patterned by focused ion beam (FIB) lithography to create four micro-traps (2 µm diameter and 2 µm depth) in a row with a separation of 2 mm between consecutive holes. Figure 23 shows a microhole patterned by FIB technique (a), the magnetic domain of a piece of the ribbon (b) and the major steps for each detection experiment. Four copper electrodes were made so that the inner electrodes had a separation of 10 mm followed by outer electrodes at a distance of 2 mm. These electrodes facilitated for the measurement by a four probe method at which the voltage was measured across the inner electrodes for the current going through the outer electrodes.

Lipid Micellar Nanoparticles (LMNs) encapsulating the iron oxide nanoparticles (ILMNs) were prepared as described previously [24]. For cell uptake experiments, the LMNs were labeled with doxorubicin hydrochloride (DOX) as a fluorescent marker. LMNs encapsulating DOX and iron oxide (DILMNs) nanoparticles were prepared. Briefly, cells were seeded 24 h prior to nanoparticle addition. Various amounts of nanoparticles were added to each

well. After 4 hrs of incubation, the cells were washed with phosphate-buffered saline (PBS) and fixed using a 10% neutral buffered formalin solution. Nuclei of the cells were stained using DAPI. The cells were imaged using the multiphoton Olympus BX61W1 confocal microscope. Cellular uptake of MLMNs and ILMNs for the iron oxide detection experiments was performed in the same manner as that of DILMNs uptake studies. Various dilutions of the cells, the nanoparticles, and the magnetically labelled cells were prepared for GMI measurements. The data presented here is for a concentration of 0.05 mg/mL Fe_3O_4 MNPs in the cell medium and their encapsulation inside cells at a concentration of 8.25×10^4 cells/mL.
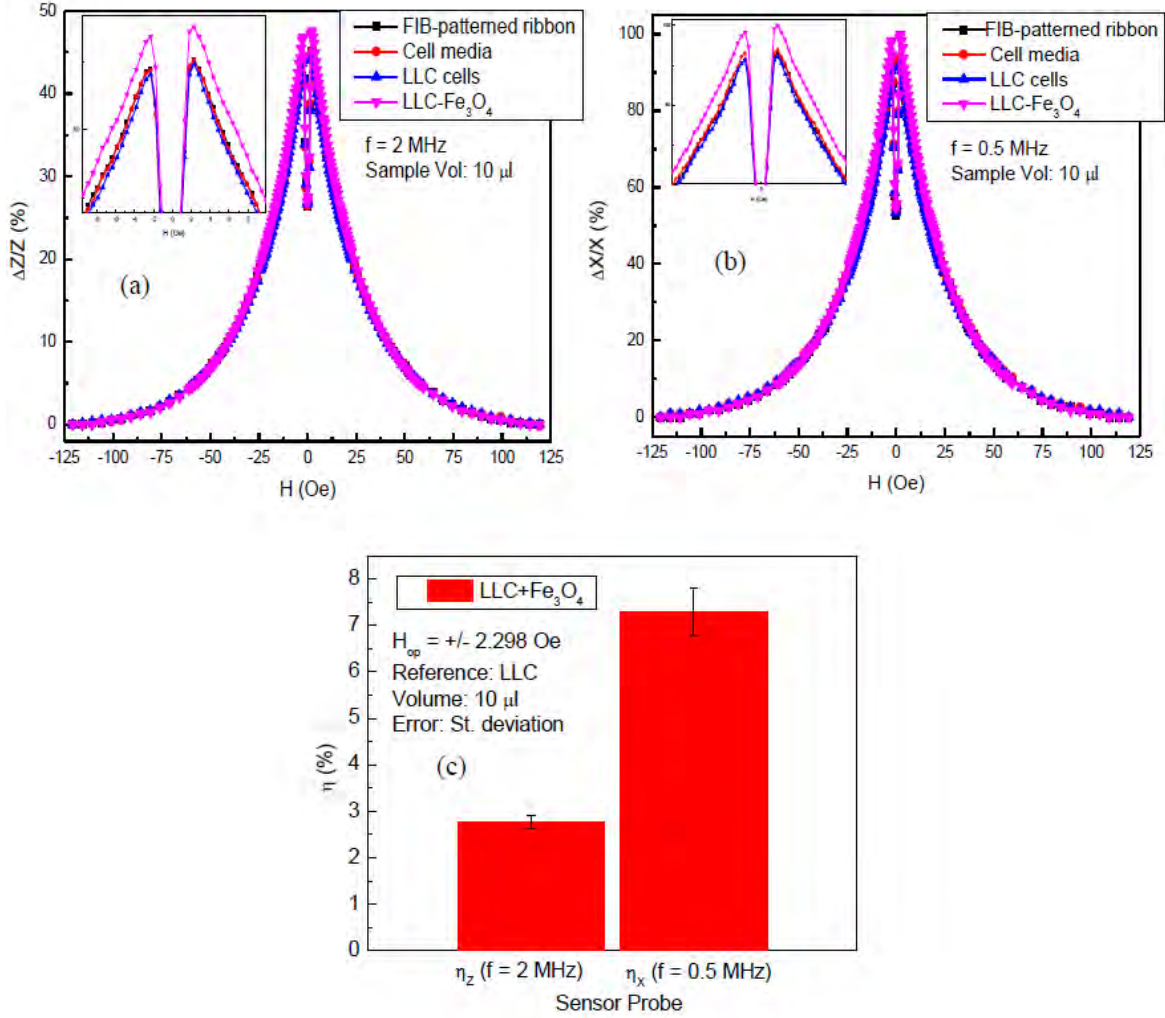
Figure 24: (a) MI and (b) MX probes of the ribbon and the ribbon with LLC cells and LLC cells that have taken up Fe_3O_4 nanoparticles. (c) Sensor detection sensitivities using the MI and MX probes, respectively.

Figure 24(a,b) shows the magnetic field dependence of the magneto-impedance (MI) and magneto-reactance (MX) probes measured at $f = 2$ MHz and 0.5 MHz, respectively, for the plain ribbon, and the ribbon with LLC cells and LLC cells containing Fe_3O_4 MNPs. Obviously the MI and MX ratios increased with magnetic field, reached a maximum at $H_k \sim 1.3$ Oe, then decreased and saturated for higher applied fields. The detection sensitivity was defined as the difference

between the MI or MX ratios, $\Delta\eta$, for the water and test samples. Figure 24(c) shows $\Delta\eta_z$ or $\Delta\eta_x$ reaches its maximum near H_k. The $\Delta\eta_z$ and $\Delta\eta_x$ were determined to be 2.6 % and 7.2 % for the LLC + Fe_3O_4 NPs, respectively. From these figures we see that the FIB-patterned probe successfully distinguished the ML-LLC cancer cells from unlabeled ones. The ML-LLC cells were detected by the MX probe with a higher sensitivity as compared to the MI probe. The measured MX-based detection sensitivity of the sensor was about 2.6 times higher than the MI-based detection sensitivity.

Soft ferromagnetic amorphous microwires for microwave energy sensing

Recently, we have developed a new method of using these microwires as a microwave absorber for fabrication of a fiber Bragg grating-based microwave energy sensor with improved sensitivity and less perturbation of the microwave field. As compared to a similar approach that uses gold to absorb electromagnetic radiation, the glass-coated amorphous microwire yields a device with greater sensitivity (~10 times at f = 3.25 GHz) relative to the perturbation of the microwave field. Nevertheless, the development of this type of sensor is still in infancy, and optimization of the overall performance in various applications requires a better understanding of the relationship between the magnetic properties, GMI, and microwave absorption effects in the microwires.

(a)   (b)
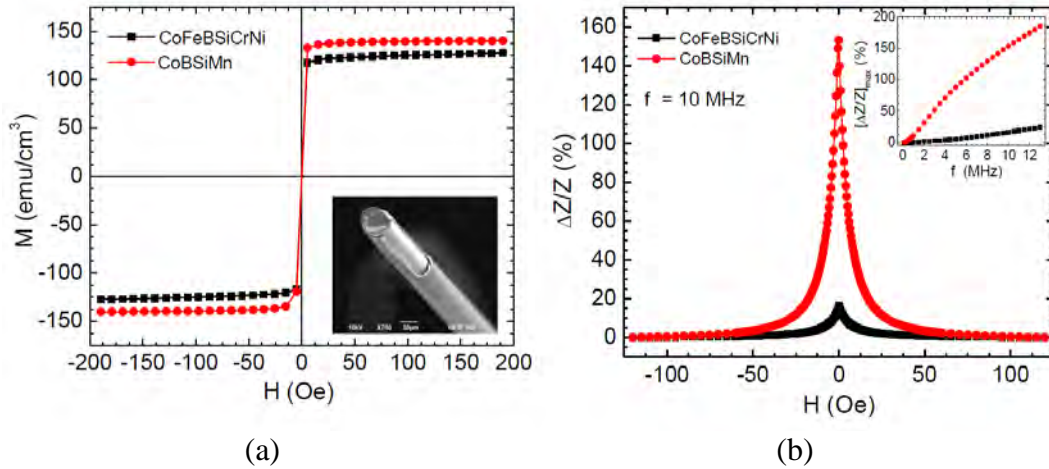
Figure 25: (a) Magnetic hysteresis loops of the CoFeBSiCrNi and CoBSiMn microwires. Inset shows a typical SEM image of a CoBSiMn microwire; (b) Magnetic field dependence of GMI ratio ($\Delta Z/Z$) for the CoFeBSiCrNi and CoBSiMn microwires at f = 10 MHz. Inset shows the frequency dependence of the maximum GMI ratio ($[\Delta Z/Z]_{max}$) for these microwires.

To address this outstanding issue, we have performed a comparative study of the magnetic parameters, magneto-impedance, and microwave characteristics of glass-coated amorphous $Co_{64.63}Fe_{4.97}B_{16}Si_{11}Cr_{3.4}Ni_{0.02}$ (CoFeBSiCrNi) and $Co_{68}B_{15}Si_{10}Mn_7$ (CoBSiMn) microwires. We have found that the $Co_{68}B_{15}Si_{10}Mn_7$ microwire possessing a softer magnetic property shows a larger GMI effect and is a better microwave absorber for fabrication of a new class of FBG-based microwave energy sensor. Our study highlights a correlation between the magnetic softness, GMI, and microwave absorption effects in the microwires.

The glass-coated microwires were prepared by the glass-coated melt spinning technique and supplied by the MicroFir Tehnologii Industriale. The average diameter of the metallic core and the thickness of the glass-coating layer are determined to 25.2 µm and 3.1 µm for the CoBSiMn microwire and 14.2 µm and 2.8 µm for the CoFeBSiCrNi microwire, respectively. A typical scanning electron microscope (SEM) image in the inset of Figure 25(a) shows the morphology of a CoBSiMn microwire. The magnetic properties of the microwires were characterized by a vibrating sample magnetometer (VSM). The magnetoimpedance of the microwires was measured by a four-probe technique on a HP4192A impedance analyzer over a wire length of 1 cm at room temperature. A driving current of amplitude 1 mA over the frequency range of 0.1 – 13 MHz was supplied along the wire axis, in the presence of axial dc magnetic fields of up to ±120 Oe. At a given frequency, the GMI ratio was calculated by

$$\frac{\Delta Z}{Z} = \frac{Z(H) - Z(H)_{ref}}{Z(H)_{ref}} \times 100\%,$$

where $Z(H)_{ref}$ is the impedance of a microwire taken as the reference to calculate the GMI ratio. In our case, the impedance at a maximum dc applied field ($H = 120$ Oe) was taken as the reference impedance. The microwire-based sensor probe was designed by attaching a microwire to an FBG cladding, which was then placed into a homemade 50 Ω microstrip transmission line, the so-called transverse electromagnetic (TEM) cell. Light from a broadband amplified spontaneous emission source (JDSU M/N BBS1560+1FP) was launched into an optical fiber that contained the FBG. Light transmitted through the optical fiber was monitored with an optical spectrum analyzer (HP M/N 70951B). The TEM cell is comprised of two parallel copper plates with the geometry chosen to produce a 50 Ω impedance. As microwave energy of different frequencies and powers was sent through the transmission line, the optical spectrum transmitted by the FBG was recorded. The microwaves were generated by an HP M/N 8703A, amplified by a Mini-Circuits M/N ZHL-42W, and monitored with an HP M/N E4419B. The HP M/N 8703A was connected to the TEM cell via a coaxial cable which was terminated with a 50 Ω load. First, the microwave scattering parameter S11 due to a section of ordinary optical fiber was recorded as a reference scan. This reference scan was subtracted from an S11 scan taken with the sensor probe in the TEM cell. For the S11 scans, care was taken to not disturb the setup while the optical fiber was being moved.

Figure 25(a) shows the magnetic hysteresis (M-H) loops taken at 300 K for the CoFeBSiCrNi and CoBSiMn microwires. It can be observed that both the microwires exhibit a soft ferromagnetic characteristic, with extremely small coercivity ($H_c \sim 0.5$ Oe) and high saturation magnetization ($M_s = 125$ emu/cm^3 and 150 emu/cm^3 for CoFeBSiCrNi and CoBSiMn microwires, respectively). It is noted that while the effective anisotropy field is almost identical ($H_k \sim 10$ Oe) for both of the microwires, the M_s of the CoBSiMn microwire is much higher that of the CoFeBSiCrNi microwire. As we show below, this difference in the M_s of these microwires influences their GMI response and microwave absorption. Figure 25(b) shows the magnetic field dependence of GMI ratio ($\Delta Z/Z$) at a measurement frequency of 10 MHz for the microwire samples. The inset shows the frequency dependence of the maximum GMI ratio (i.e. $[\Delta Z/Z]_{max}$) for both types of microwire. It can be seen that the maximum GMI ratio is much higher for the CoBSiMn microwire than for the CoFeBSiCrNi microwire in the investigated frequency range of 0.1 – 13 MHz. For instance, at $f = 10$ MHz $[\Delta Z/Z]_{max} = 153.32$ % for the CoBSiMn microwire, which is about 9 times higher than that for the CoFeBSiCrNi microwire ($[\Delta Z/Z]_{max} = 16.44$ %). To compare the field sensitivity of a GMI-based sensor using these two

microwires, we have calculated the field sensitivity of GMI (η) for both the microwires at 10 MHz via $\eta = \frac{2\left[\frac{\Delta Z}{Z}\right]_{max}}{\Delta H}$, where ΔH is the full width at half maximum of a GMI curve. We find that the η for the CoBSiMn microwire ($\eta = 34.10$ %/Oe) is about 10 times higher than that for the CoFeBSiCrNi microwire ($\eta = 3.43$ %/Oe). This result indicates that the CoBSiMn microwire is better suited for use in magnetic field sensors. To quantify the impedance change of the transmission line due to the presence of each microwire as a microwave absorber, we first measured the S-parameter (S11) as a function of microwave frequency in the range of 0.1 – 7.5 GHz. We then calculated the FBG wavelength (λ_{FBG}), which corresponds to the minimum of the observed S11 parameter, in response to microwave power delivered in the transmission line at various microwave frequencies. As an example, the variation in λ_{FBG} with microwave power for selected frequencies of 3.25 GHz and 5 GHz is depicted in Figure 26.
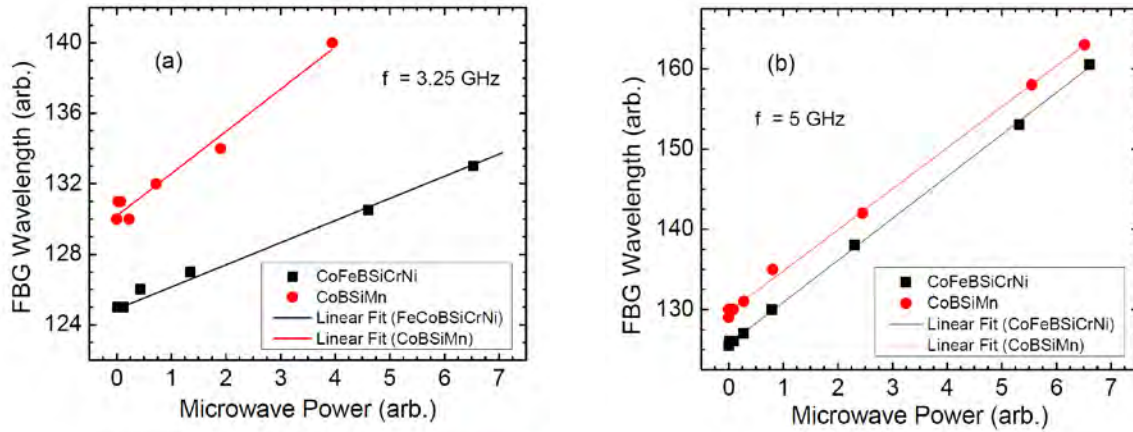
Figure 26: Bragg wavelength as a function of microwave power at two selected microwave frequencies of (a) 3.25 and (b) 5 GHz for the CoFeBSiCrNi and CoBSiMn microwires.

It can be observed that at a given frequency λ_{FBG} is shifted to a longer wavelength as the microwave power delivered to the microwave cell is increased. With increasing power, more of the microwave energy is absorbed by the microwire which begins to heat up, raising the temperature of the FBG and consequently shifting the λ_{FBG} to a higher value. The shift in λ_{FBG} increases linearly with the delivered microwave power at all frequencies. It is worth noting that in the investigated frequency range 0.1 – 7.5 GHz, the slope of the λ_{FBG} shift with microwave power is significantly larger for the CoBSiMn microwire compared to the CoFeBSiCrNi microwire, from which it can be inferred that the CoBSiMn microwire will exhibit superior microwave energy field sensing capabilities. To confirm this, we have computed a figure-of-merit (FOM) at a particular frequency for each microwire probe using the following relation:

$$FOM = \frac{\text{Linear slope of } \Delta\lambda_{FBG} \text{ vs. microwave power}}{10^{\left(S_{11}/10\right)}}.$$

The results of the FOM characterization of the microwire probes at various microwave frequencies are displayed in Figure 27. As expected, the probe using the CoBSiMn microwire as a heating element in the FBG sensor shows an improvement in FOM over the CoFeBSiCrNi microwire probe. Given that the thickness of the glass coating layer is almost identical for both types of wire ($\sim$ 3 μm) and that the measurements were carried out under the same conditions,

the larger values of $[\Delta Z/Z]_{max}$, η, and FOM achieved for the CoBSiMn microwire are likely attributed to the softer magnetic property of the material. These results point to a correlation between the magnetic softness, GMI, and microwave absorption in the microwires.
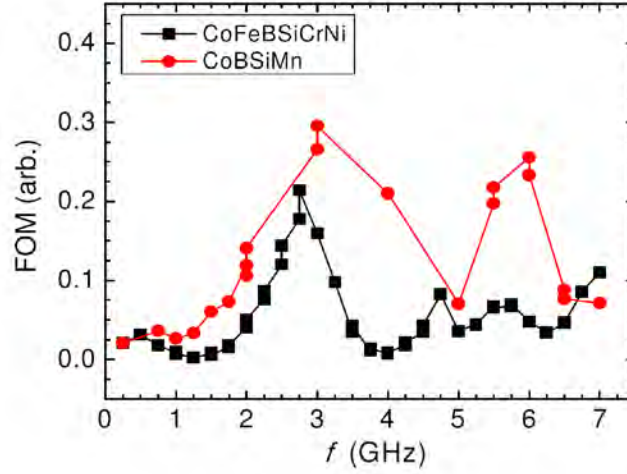
Figure 27: FOM of the microwire-based probes using the CoFeBSiCrNi and CoBSiMn microwires. The better performance of the probe using the CoBSiMn microwire is observed in the frequency range of 0.1 – 7 GHz.

2. A new type of multiwire-based sensors for magnetic sensing applications:

Recently, He *et al.* have used a Co-based amorphous microwire as a sensor core to improve sensitivity to a level that allows the relatively weak magnetic signals of a magnetic system to be detected. In this design the change in the inductance of the coil-system is driven by an ac current in the presence of an external dc magnetic field along the axis of the coil, producing a longitudinally excited magneto-inductance (LEMI) effect. There is a need for improved sensitivity in LEMI-based sensors in order to fulfill the increasing requirements of industrial and engineering applications.
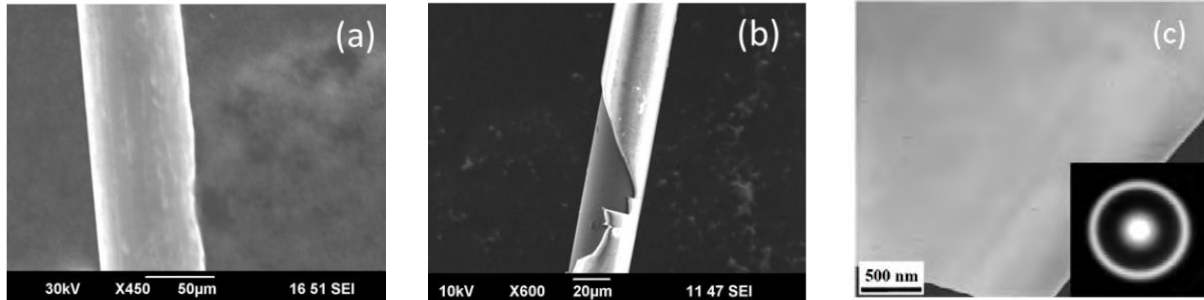
Figure 28: SEM images of (a) a melt-extracted $Co_{68.2}Fe_{4.3}B_{15}Si_{12.5}$ microwire and (b) a glass-coated $Co_{68}B_{15}Si_{10}Mn_7$ microwire; (c) a TEM image of the $Co_{68.2}Fe_{4.3}B_{15}Si_{12.5}$ microwire, with the corresponding SAED pattern shown in the inset.

We have proposed an effective approach to improve the sensitivity of inductance coil sensors by designing a sensor core that consists of multiple soft ferromagnetic microwires. A systematic study of the LEMI effect has been performed in a non-magnetic copper wire coil with

a filler composed of multiple Co-rich amorphous microwires. Melt-extracted microwires (MEW) of $Co_{68.2}Fe_{4.3}B_{15}Si_{12.5}$ and glass-coated microwires (GCW) of $Co_{68}B_{15}Si_{10}Mn_7$ with excellent soft magnetic properties were used for this study.

Figure 28 shows the SEM images of the MEW and GCW, along with a TEM of the MEW. SEM images taken on different segments of wire showed an average diameter d of ~50 µm for the MEW and ~25 µm for the GCW plus a Pyrex glass coating of the thickness ~3 µm. SEM, TEM and SAED data confirm the amorphous nature, morphology, and quality of the prepared microwires.
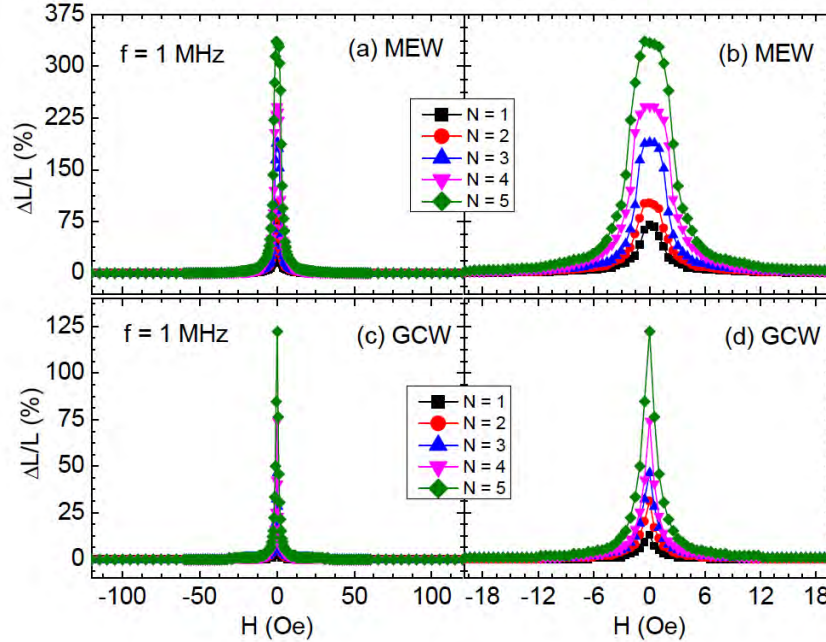
Figure 29: Magnetic field dependence of the inductance (L) of the coil measured at $f = 1$ MHz for (a, b) the MEW based core and (c, d) the GCW based core for N = 1 - 5. (b) and (d) show the enlarged portions of (a) and (c), respectively.

We have shown that the LEMI ratio and field sensitivity of an inductive coil depend strongly upon the filler-to-air ratio inside the coil, the magnetic softness, and the anisotropy axis distribution of the microwire. Relative to a single-microwire based sensor, the LEMI ratio and field sensitivity of a multi-microwire based sensor are enhanced by 3 to 4 times, when varying the number of microwires inside the inductive coil. The sensitivity of the sensor using four glass-coated $Co_{68}B_{15}Si_{10}Mn_7$ microwires in the core reaches a maximum value of 1957 %/Oe. Figure 29 shows the magnetic field dependence of the LEMI ratio ($\Delta L/L$) at a representative frequency of 1 MHz for both systems of wire. The LEMI ratio for N = 1 is 71.68 % (13.04 %) for the MEW (GCW) and increases with N to reach 337 % (122 %) for N = 5. From a sensor application perspective, the large enhancement of the LEMI ratio achieved for the sensor core composed of multiple soft ferromagnetic wires (as compared to that of a single wire) is ideal for developing highly sensitive magnetic sensors for detection of weak magnetic fields in engineering and biological systems. We have also found that the increase in $[\Delta L/L]_{max}$ with N was very large in the frequency range 0.1 MHz – 2 MHz and became less prominent at high frequencies ($f > 2$ MHz). This indicates that the frequency range of 0.1 MHz – 2 MHz would be the most suitable

choice for the operating frequency of sensors based on the LEMI/magnetic-wire-core design in this study.

Magneto-reactance based biosensor for detection of cancer cells and biomolecules

A combination of the GMI effect with functionalized magnetic nanoparticles (MNPs) has high potential for the development of a simple and reliable biosensing system that can be used as a quick detection technique before magnetic resonance imaging (MRI). In this study we demonstrate the capacity of detecting magnetically weak manganese oxide (MnO) nanoparticles and the Lewis lung carcinoma (LLC) cancer cells that have taken up these nanoparticles using a novel biosensor based on the MX effect of a soft ferromagnetic amorphous ribbon with a micro-patterned surface.
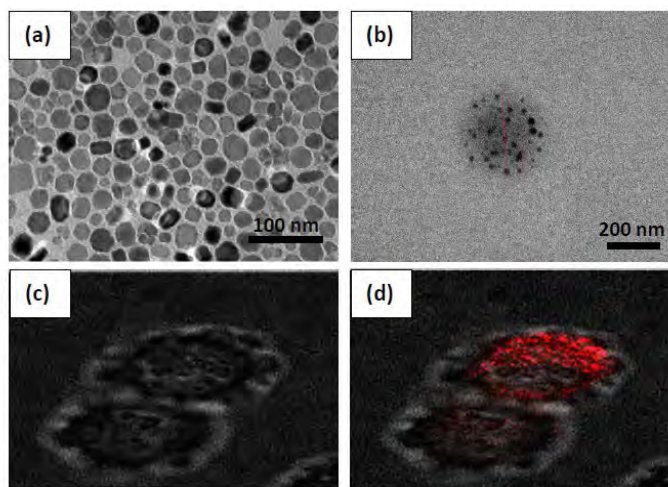
Figure 30: TEM images of the MnO MNPs (a) and MLMNs (b); Optical images of the LLC cells (c) and LLC cells that have taken up the MLMNs (d).

MnO nanoparticles and MnO MNPs incased in phospholipids (Manganese Oxide Lipid Micellar Nanoparticles or MLMNs) were prepared. Dichloromethane was added to improve the dispersibility of the nanoparticles. The nanoparticles were washed three times in acetone to remove excess surfactant and solvent. To encapsulate MnO nanoparticles, PEG-2000 PE, DC-cholesterol, and DOPE were added to chloroform and MnO nanoparticles were added to the solution. The chloroform was then evaporated in a vacuum oven and the dry film was heated at 80 °C. Water was added to the dry film and the solution was sonicated. For cell uptake experiments the MLMNs were labeled with DOX as a fluorescent marker. Doxorubicin hydrochloride (DOX) along with 4 M equivalents of triethylamine was added to chloroform and the mixture was sonicated to dissolve the DOX. Phospholipid micelles encapsulating DOX and MnO (DMLMNs) were prepared as previously described with some modifications. Cellular uptake of MLMNs for the MnO detection experiments was preformed in the same manner as those of the FMLMN uptake studies. Cells were seeded 24 h prior to transfection into a 35mm dish in 2ml of complete medium (DMEM containing 10% FBS, 2 mM L-glutamate and 1% penicillin/streptomycin). At the time of MLMNs addition, the medium in the dish was replaced with 1.5ml of fresh DMEM without FBS. Two milligrams of MLMNs, diluted in 50 µl DMEM with no FBS, was added the dish. After 24 h of incubation the cells were collected off of the dish

using 0.25% trypsin and counted. Various dilutions of the cells were prepared for the impedance measurments. Various dilutions of the MLMNs alone were also prepared for the impedance measurments. The magnetic hysteresis loop (M-H) of the MnO MNPs was measured at room temperature by a vibrating sample magnetometer (VSM).

Figure 30(a,b) shows the TEM images of the MnO MNPs and MLMNs. Figure 30(c,d) shows optical images of the blank LLC cells and the LLC cells that have taken up the MLMNs. TEM images of MnO MNPs showed spherical nanoparticles with a size range of $10 - 30$ nm. Analysis by dynamic light scattering (DLS) gave the hydrodynamic radius for the M-LMNs to be about 100-200 nm, which was confirmed by TEM images. Cellular uptake of the MLMNs was examined by labeling the particles with DOX. LLC cells were incubated with the DMLMNs for 4 h and the DOX was visualized by confocal microscopy (Figure 30(d)). DMLMNs were seen in the cytoplasm surrounding the nuclei of the cells.
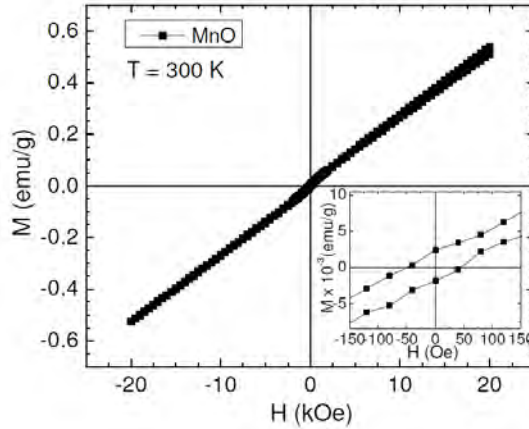
Figure 31: Magnetic hysteresis loop (M-H) of the MnO MNPs taken at room temperature.

Figure 31 shows the magnetic hysteresis (M-H) loop of the MnO MNPs measured at room temperature, with an inset showing an enlarged portion of the low-field loop. From the main panel of Figure 2, it appears that the MnO MNPs behave like paramagnetic particles whose magnetic moments often increase linearly with respect to an applied magnetic field. However, the inset of Figure 2 shows a small hysteresis with a coercivity of $H_c \sim 50$ Oe and a remanence magnetization of $M_r \sim 2.5 \times 10^{-3}$ emu/g in the low field range (± 100 Oe), which is characteristic of a weakly ferromagnetic material. These small values of M_r and H_c indicate a reversible magnetization process when the magnetic field is recycled. Such a behavior of the MnO MNPs is similar to that of superparamagnetic Fe_3O_4 MNPs, except that the former has a much smaller magnetic moment compared to the latter. In other words, a magnetic biosensor with higher detection sensitivity would be needed for detection of the MnO MNPs and the LLC cells that have taken up these MNPs.

Figure 32(a) and (b) show the field dependence of MI and MX ratios measured at f = 1.5 and 0.5 MHz, respectively for the etched ribbon with 10 μl of LLC, MLMNs, and LLC+MLMNs drop-casted on the ribbon surface. The operating frequencies for the MI and MX-based detection were chosen to be f = 1.5 and 0.5 MHz as the highest detection sensitivities were respectively

achieved at these frequencies.[2] As one can see clearly in Figure 32(a,b), the MI and MX profiles have a double-peak feature for all the samples. This double-peak feature has been typically attributed to the presence of transverse anisotropy in a Co-based ribbon. It has been shown that the peak position corresponds to the effective anisotropy field of the ribbon[5]. The MI and MX ratios were first measured with and without the blank LLC cells at the desired frequencies, showing a negligible influence of the cells on the MX or MI signal. The measurements were then repeated for equal volume and concentrations of the MLMNs and the LLC cells that have taken up the MLMNs. It is worth noting in Figure 32(a) that neither the MLMNs-embedded LLC cells nor the MLMNs themselves altered the MI ratio of the ribbon. However, the MX ratio of the ribbon was found to increase significantly in the presence of the MLMNs and the LLC+MLMNs (Figure 32(b) and its inset).
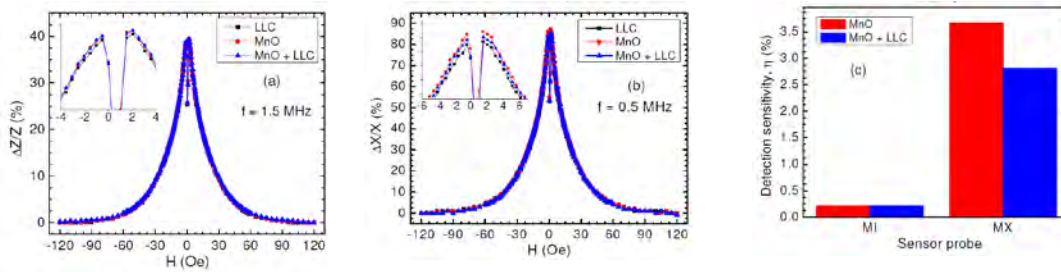
Figure 32: Magnetic field dependence of $\Delta Z/Z$ (a) and $\Delta X/X$ (b) ratios with LLC, MnO MNPs, and MnO-embedded LLC cells at f = 0.5 and 1.5 MHz, respectively; (c) A comparison of the detection sensitivity between the MI and MX sensor probes for detection of the MLMNs and MLMNs-embedded LLC (0.05mg/ml MnO and 8.25 x 10^4 cells/ml respectively).

To better illustrate the detection capacity of the MLMNs and the LLC cancer cells that have taken up the MLMNs, we have evaluated the detection sensitivity of the sensor using Eq. (3). The results are plotted in Figure 32(c). It can be seen that the MI ratios for both MLMNs and LLC+MLMNs reached at a similar level which is slightly higher (< 0.4%) than the LLC level. This indicates that the MI-based biosensor is not suitable for probing the MLMNs and the MLMNs-embedded LLC cells at the tested concentrations. However, the detection sensitivity reached much larger values of ~ 3.6% and 2.8 % for the bare MLMNs and the MLMNs-embedded LLC cells, respectively.

The variation in the original MX ratio of the ribbon due to the presence of the MLMNs and the MLMNs-embedded LLC cells can be explained by considering the disturbance of the applied dc longitudinal and ac transverse fields due to the presence of the fringe fields of the MLMNs on the surface of the ribbon. Although the magnetic moments of the MLMNs are small, microholes produced by the etching technique on the ribbon surface minimize their physical motion and make a stronger field disturbance effect. As a result, the MX value of the ribbon changes in the presence of the MLMNs or the LLC cells that have taken up these MLMNs. The detection sensitivity due to the presence of the MLMNs-embedded LLC cells is smaller than that obtained for the MLMNs themselves. This decrease in η can be explained by considering the fact that the effect of fringe fields decreases as the distance from the MLMNs to the ribbon surface is increased. In the present case, when the MLMNs are embedded in the LLC cells, the distance

from the MLMNs to the sensor surface increases. As a result, the magnetic disturbance effect becomes weaker, leading to a lesser influence on the original MX value of the ribbon.

C. High aspect-ratio magnetic nanostructures for novel biosensors and microwave device applications

There is an increasing need for the use of nanostructured materials with tunable and anisotropic magnetic properties. However, the ability to tune the magnetic anisotropy of magnetic nanoparticles to meet the needs of vastly different applications is a challenge. Recently we have introduced a new concept of incorporating superparamagnetic nanoparticles such as magnetite (Fe_3O_4) and cobalt ferrite ($CoFe_2O_4$) into a polymer matrix to create a new class of nanocomposite materials with tunable microwave response [25,26]. We propose that the microwave response can be further enhanced in high-aspect ratio magnetic nanostructures, such as carbon nanotubes (CNTs) filled with supermagnetic nanoparticles, where the magnetic anisotropy can easily be tuned by varying the size and density of magnetic nanoparticles inside CNTs. Previously, we have reported the synthesis and characterization of CNTs filled with magnetite, cobalt ferrite and nickel ferrite nanoparticles [27]. Interestingly, all ferrite-filled CNTs show enhanced interparticle interactions relative to the nanoparticles alone. Our results revealed the new possibility of tuning the magnetic properties of nanoparticle-filled CNTs for sensor and microwave device applications. In this project, we have successfully filled CNTs with

1. with superparamagnetic NiFeO nanoparticles
2. with core/shell structured $Fe/\gamma Fe_2O_3$ nanoparticles with anisotropic magnetic properties

In addition, we have developed a novel magnetic nanostructure composed of polymer thin films with Fe_3O_4 nanoparticle-filled nanoholes arrays. In the following sections, we will emphasize the main results of these studies.

Carbon nanotubes filled with $NiFe_2O_4$ nanoparticles

One-dimensional magnetic nanostructures composed of multiwalled carbon nanotubes (MWCNTs) filled with magnetic nanoparticles are very promising for a variety of applications ranging from electromagnetic interference shielding to water purification, and biomedical applications such as hyperthermia and targeted drug delivery [28-30]. The fabrication of uniform MWCNTs with reduced diameters (below 100 nm) is presently a challenging task. In our previous work, MWCNTs synthesized using commercially available templates were successfully filled with magnetite nanoparticles (Fe_3O_4) [27]. During that study, however, we found that commercial alumina templates used in MWCNT growth generally yield non-uniform magnetic properties due to poor uniformity in pore size throughout the template thickness. Synthesis of customized templates with better pore diameter control is essential to overcome these limitations.
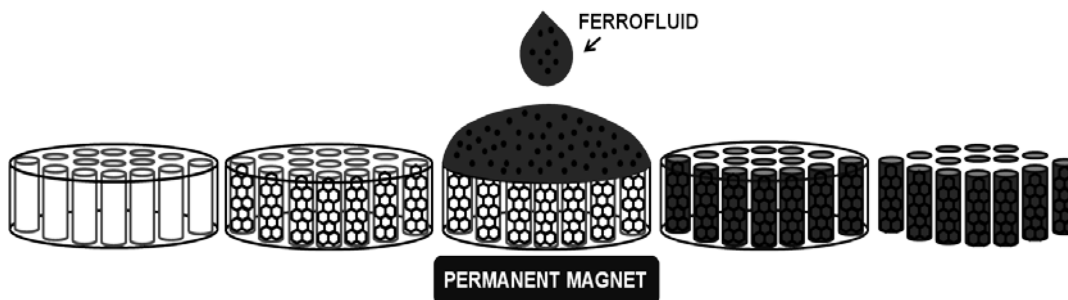
Figure 33: A schematic of the CNTs filling process with C/S NPs.

We present results from MWCNTs successfully synthesized using custom-made 80 nm pore-size alumina templates, filled with nickel ferrite (NFO) nanoparticles of 7.4 ± 1.7 nm in diameter. Detailed magnetic characterization was performed using DC and AC susceptibility experiments. $NiFe_2O_4$ nanoparticles were synthesized in-house using a thermal decomposition method. The final product was suspended in high-purity hexane to create a ferrofluid. Custom highly ordered anodic aluminum oxide (AAO) membranes were fabricated from high purity aluminum foil (99.999%) by electrochemical route using a controlled two-step anodization process. In this process, electrodes were placed on both sides of a degreased and electropolished high-purity aluminum foil in a 0.3 M oxalic solution at a voltage of 40 V and 4 ºC. This first anodization formed initial seeds for the membrane pores. The alumina obtained during the first step was chemically removed using a mixture solution of CrO_3 and H_3PO_4. The resulting surface was anodized again to obtain alumina templates with hexagonally ordered self-assembled nanopores. The remaining aluminum substrate was removed by a mixed solution of $CuCl_2 \cdot 2H_2O$ and HCl. In order to obtain pores with openings at both sides, the alumina barrier layer was chemically etched by an H_3PO_4 solution. These membranes were later used as templates for MWCNT synthesis and filling. MWCNTs were synthesized using a catalyst-free method via chemical vapor deposition. Prior to MWCNT growth, an alumina template was heat-treated at 640° C to avoid warping during synthesis. The heat-treated template was then placed at the heat source and heated to 620° C under the flow of argon gas. Once at the reaction temperature, helium and ethylene gas were introduced at flow rates of 70 and 30 sccm, respectively, and the flow of argon gas was terminated. This ratio was maintained for 5.5 hours, before the MWCNT-filled alumina template was allowed to cool (see Figure 33).
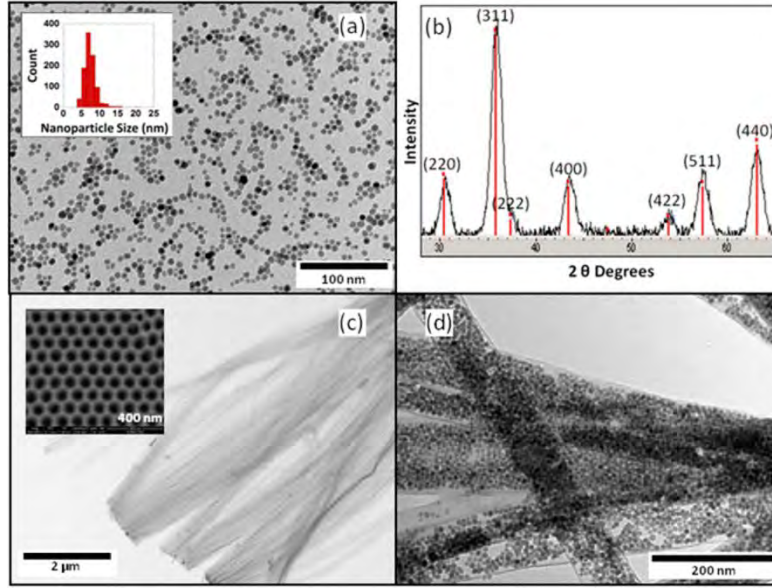
Figure 34: TEM image of nickel ferrite nanoparticles with histogram inset showing particle size distribution (a); XRD plot showing peaks for inverse spinel structure of nickel ferrite nanoparticles (b); TEM image of free-standing MWCNTs with inset showing SEM of hexagonally-ordered pores in the alumina membrane (c); TEM image of nickel-ferrite-filled MWCNTs (d).

Following synthesis, MWCNTs were filled with nanoparticles. The alumina template containing MWCNTs was filled with nanoparticles using a magnetically-assisted capillary action. The MWCNT-rich alumina template was placed atop a permanent magnet ($\mu_0 H = 0.5$ T), and the previously synthesized ferrofluid was slowly dropped on to the surface of the alumina template so that the nanoparticles were able to coat the inner walls of the MWCNTs. Finally, the alumina template was dissolved by gently crushing the nanoparticle-filled alumina template and sonicating in an 8 molar solution of sodium hydroxide and vacuum filtering through a polyester nucleopore membrane (pore size, ~200 nm). After filtration, the resulting nanoparticle-filled-MWCNTs were collected and stored in isopropanol for further structural and magnetic characterization by TEM and PPMS.

In Figure 34 (a) we present the TEM image of the as-synthesized NFO nanoparticles. As observed, all of the nanoparticles exhibit spherical shape and a relatively narrow size distribution with an average size of 7.4 ± 1.7 nm, as inferred from the histogram in the inset. It can also be seen that the surfactants were employed effectively, avoiding nanoparticle agglomeration. The XRD plot obtained for the NFO nanoparticles exhibits clear diffraction peaks (Figure 34(b)) indicating that we obtained highly crystalline nanoparticles, despite their small size; they have been successfully indexed with the inverse spinel structure (AB_2O_4) characteristic of the $NiFe_2O_4$ phase. An SEM image of one of the custom-made AAO membranes is presented in the inset to Figure 34(c). It is clear to see that the AAO membranes present a well-defined and homogeneous hexagonal array of pores, with an average diameter of 80 nm and inter-pore distance of 105 nm; membrane thickness is 40 µm. Un-filled MWCNTs prepared using these membranes are imaged in Figure 34(c). They present an outer diameter of approximately 80 nm and lengths of up to 11 µm. Finally, in Figure 34(d) we present an image of the NFO-filled

MWCNTs. It is observed that no nanoparticles remain outside of the MWCNTs, and that the nanoparticle packing within the MWCNTs is quite uniform. Our past studies have revealed that whenever there is a high degree of non-uniformity and agglomeration of particles into random clusters, the magnetic properties are often irreproducible from batch to batch so this uniform packing is crucial for reproducible magnetic response needed for applications.
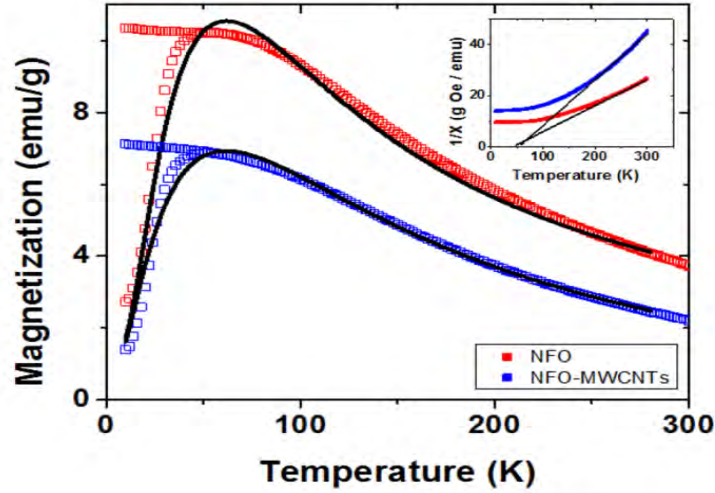
Figure 35: M-T curves using the zero-field cooled and field-cooled protocols (H=100 Oe) along with fittings of the ZFC curves; inset shows Curie-Weiss fitting using ZFC curves.
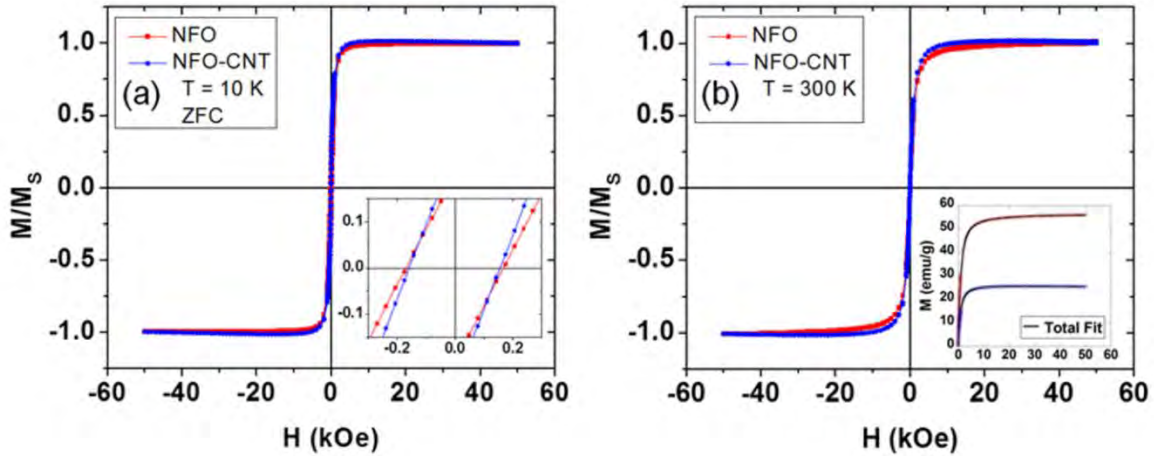
Figure 36: Magnetization vs. Magnetic Field curves at 10 K under the zero-field cooled protocol for nickel ferrite and nickel ferrite-filled MWCNTs with inset showing hysteresis (a); Magnetization vs. Magnetic Field curves at room temperature for nickel ferrite and nickel ferrite-filled MWCNTs with inset showing Langevin-function fit of each hysteresis curve (b).

In Figure 35 we present zero-field-cooled/field-cooled (ZFC-FC) curves normalized by the mass of the samples for the NFO nanoparticles and the NFO-filled MWCNTs (NFO-CNTs). As can be seen, the curves for NFO and NFO-CNTs share a similar shape with ZFC curves presenting a defined maximum around T_B ~52 K associated with the blocking process of the nanoparticles. The irreversibility temperature (T_{irr}), where the ZFC and FC curves separate,

occurs nearly at T_B, indicating monodispersity of the nanoparticles, as confirmed by TEM. No shoulder or additional maximum at very low temperatures is observed, as has been reported in similar NFO nanoparticle systems and ascribed to surface spin freezing and glassy behavior [11]. This indicates that the surface spin disorder in our nanoparticles is negligible. To probe superparamagnetic properties of our sample, we have fit the ZFC M-T curves using an appropriate expression based on the Stoner-Wohlfarth model:

$$M_{ZFC} = \int_0^{V_c} M_{ZFC}^{SPM} f(V)dV + \int_{V_C}^{\infty} M_{ZFC}^{bl} f(V)$$

where V is the volume of the nanoparticles, $f(V)$ is the size distribution of the nanoparticles, which we have assumed to be Log-Normal; $V_c(\text{T}) = 25k_BT/ K_{eff}$ is the critical volume of the nanoparticles, which marks the limit between superparamagnetic and blocked nanoparticles, K_{eff} is the effective anisotropy; finally M_{ZFC}^{SPM} and M_{ZFC}^{bl} are the magnetic contribution of the nanoparticles in a superparamagnetic and blocked state, respectively. The details of the analysis can be found in Ref. 13. In principle, this model was designed for non-interacting nanoparticles, but in a first approximation it can be considered that the presence of the interparticle interactions will mainly affect the effective anisotropy value, K. As observed, a very nice fitting is obtained in nearly the entire range of temperatures analyzed. From the fitting, we obtain an average particle size of 7.9±1.8 and 7.1±1.9 nm for the NFO and NFO-CNT samples, respectively, which are in very good agreement with TEM analysis. The effective anisotropy values are of 4.9×10^5 and 6.9×10^5 erg/cc for NFO and NFO-CNTs samples. The average particle size and effective anisotropy values for NFO-CNTs are one order of magnitude larger than the bulk magnetocrystalline anisotropy (-7×10^4 erg/cc). As depicted in the inset of Figure 35, a good fitting to the Curie-Weiss Law is found above 200 K with T_C close to 50 K and positive, indicating weak ferromagnetic-like interactions.
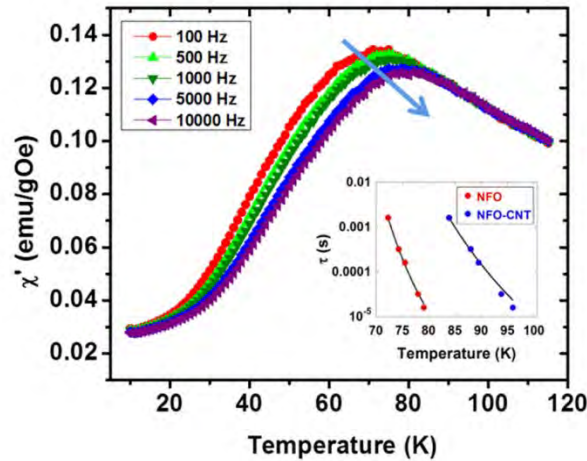
Figure 37: AC Susceptibility measurement for nickel ferrite nanoparticles used for filling with inset showing a fitting of the peaks for both the nickel ferrite and nickel ferrite-filled MWCNTs to the Vogel-Fulcher model.

Figure 36 shows M-H loops for the NFO and NFO-CNT samples at 10 K and 300 K. Note that the decrease in magnetization in the NFO-CNT sample is due to the fact that the mass includes that of the MWCNTs in addition to the NFO nanoparticles. At 10 K, the coercivity (H_C) is relatively small, 167 Oe and 155 Oe with a normalized remanence (M_R/M_S) of 0.20 and 0.22 for NFO and NFO-CNTs, respectively. No coercivity or remanence is observed in the samples at

300 K, suggesting that the 7.4 nm NFO nanoparticles exhibit SPM-like behavior at room temperature. As seen from the inset of Figure 3(b), the fittings for NFO and NFO-CNTs at 300 K are very good, although the apparent size obtained from the fittings is a little bit bigger than expected, 8.5-9 nm, which is likely due to the effect of dipolar interactions, which although weak, cannot be neglected.

Ac susceptibility measurements were systematically performed on the samples by applying a 10 Oe AC field within a frequency range of 100 Hz to 10 kHz. The peak shift values are 0.05 and 0.07, for the NFO and NFO-CNTs, respectively, which are close to the values expected for super-spin glass systems. Figure 37 shows the real part, χ', of the AC susceptibility. Since we established earlier that there are weak dipolar interactions, we fit results from both samples to the Vogel-Fulcher model:

$$\tau = \tau_{VF} \exp\left(\frac{E_a}{k_B(T-T_0)}\right)$$

$E_a = K_{eff} V$ is defined as the anisotropy energy barrier and τ_{VF} is defined as the relaxation time of each magnetic nanoparticle. A relatively good fitting is obtained in both cases, giving values for the relaxation times around 10^{-11}-10^{-12} s; the K_{eff} values are found to be 2.2 x10^5 and 5.6x10^5 erg/cc, and T_0 ~ 52 and 40 K, for the NFO and NFO-CNTs, respectively. These values are slightly smaller than those obtained in the ZFC/FC fitting because in that fitting, the effect of the interactions is reflected in K_{eff}, however, here it is reflected in T_0. These results confirm a super-spin-glass-like behavior mediated by dipolar interactions for these samples at low temperatures (< 50 K). The slightly higher K_{eff} and lower T_0 for the NFO-CNTs, could be related to a slight weakening of the interactions when the nanoparticles are inside the CNTs.

Carbon nanotubes filled with core/shell Fe/γFe$_2$O$_3$ nanoparticles:

Core/shell (C/S) structured Fe/γFe$_2$O$_3$ nanoparticles are interesting because they are hybrid nanostructures of two different materials [31]. These particles have shown very interesting magnetic behavior, such as exchange bias, super spin glass state and collective magnetic behavior, owing to their unique morphology and enhanced inter-particle and intera-particle interactions. We have successfully fabricated CNTs filled with Fe/γFe$_2$O$_3$ nanoparticles and investigated their magnetic properties. The core/shell nanoparticles were synthesized by thermally decomposing iron-pentacarbonyl using a home-build chemical synthesis setup.
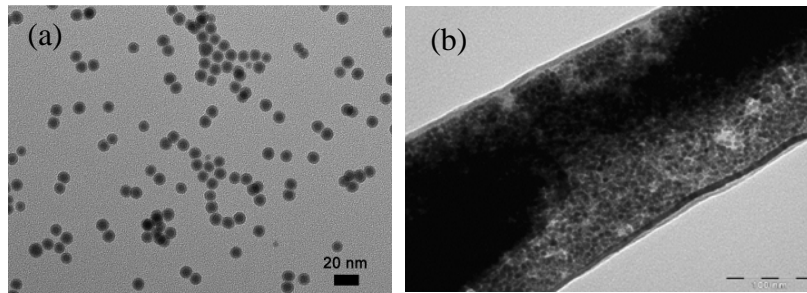
Figure 38: A TEM image of C/S Fe/γFe$_2$O$_3$ nanoparticles along with a nanoparticle-filled CNT.

Figure 38 shows the TEM image of 12.2±0.7 C/S NPs. As reported earlier, the core is made up of metallic Fe$^{(0)}$ and the shell is composed of randomly oriented grains of γFe$_2$O$_3$. With the variation of average particle size, core size varies whereas shell thickness remains same (~ 2nm). Continuing our study on nanoparticle-filled CNTs, we filled multi-walled CNTs with the

core/shell Fe/γFe$_2$O$_3$ nanoparticles described above. The filled-CNT synthesis method is outlined in the schematic below. The CNTs were synthesized using an alumina template-assisted chemical vapor deposition growth method [27]. No catalyst was used in the synthesis of these CNTs. The alumina template, with pore size ranging from 200-350 nm, is placed vertically in the CVD furnace and gasses are flowed through it at a rate of 70 sccm for helium and 30 sccm for ethylene.

Magnetic measurements in Figure 39 indicate that the C/S NPs have a blocking temperature of 92 K, as shown from the ZFC curve. The nanoparticles display no coercivity at room temperature, indicating a superparamagnetic nature. Coercivity at 20 K, ZFC measurement is 130 Oe. The magnetic measurements of NP-filled CNTs reveal that the blocking temperature of the C/S NPs (when encapsulated within the CNTs) increased to 145 K, which is indicative of enhanced inter-particle interactions. The M(H) measurement at 300 K, once again shows no coercivity, indicating that the nanoparticles are still in the superparamagnetic regime. From the M(H) measurement under the ZFC protocol at 20 K, the coercivity is 150 Oe. The enhanced coercivity below blocking is also indicative of enhanced inter-particle interactions. It is worth noting that relative to C/S NPs, the saturation magnetization (M_s) is greatly enhanced in the CNTs filled with C/S NPs. This is very beneficial for the use of these novel nanostructures in biomedical applications such as hyperthermia and MRI. However, the origin of this increase in M_s remains to be investigated.
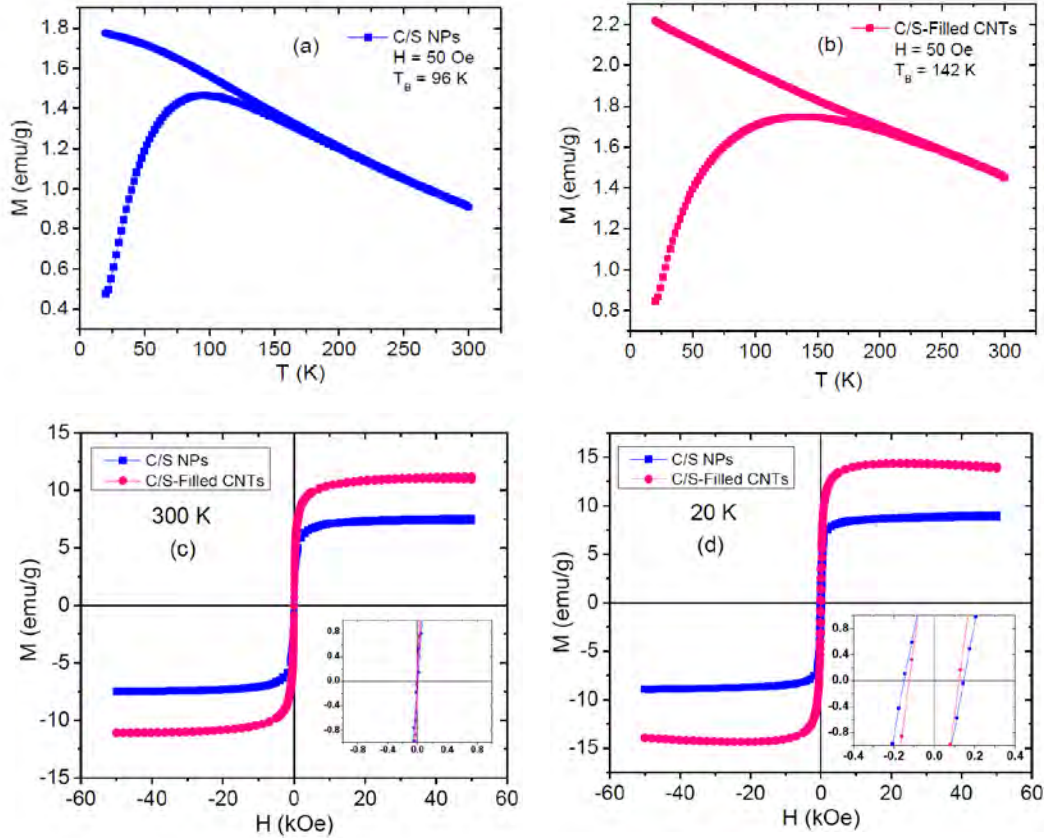
Figure 39: Temperature dependence of ZFC and FC magnetization of (a) C/S NPs and (b) C/S NPs -filled CNTs; (b,c) M-H curves taken at 300 K and 20 K for these samples.

Future work on this system includes taking ac susceptibility data and incorporating the filled-CNTs into polymer nanocomposites to meet the needs of vastly different applications. We are planning to systematically investigate magnetic anisotropy that plays a key role in controlling the magnetic properties in nanoparticle assemblies. In addition to the standard dc and ac magnetization measurements with the PPMS, we plan to conduct resonant radio-frequency (RF) transverse susceptibility and magneto-impedance measurements on magnetic nanoparticle-filled CNTs.

Highly ordered magnetite nanoparticle-filled nanohole arrays for biomedical applications

Nanoarchitecturing of thin films has emerged as a straightforward and effective way to engineer materials' properties at the nanometer level. Currently, there is an increasing need for the use of nanostructured materials with tunable and anisotropic magnetic properties. However, the ability to tune the magnetic anisotropy of magnetic nanoparticles to meet the needs of vastly different applications is a challenge [32]. Recently, the sub-100 nm nanohole arrays have been successfully fabricated from a pre-ceramic polymer mold using spin-on nanoprinting (SNAP) [33]. If these nanohole arrays can be filled with magnetic particles to create a new class of novel high-aspect ratio magnetic nanocomposites, the challenge raised above can be resolved. With this motivation, we present a simple and high throughput method to develop an array of Fe_3O_4 nanoparticle-filled nanoholes and demonstrate the unique magnetic properties of the material for a variety of applications.
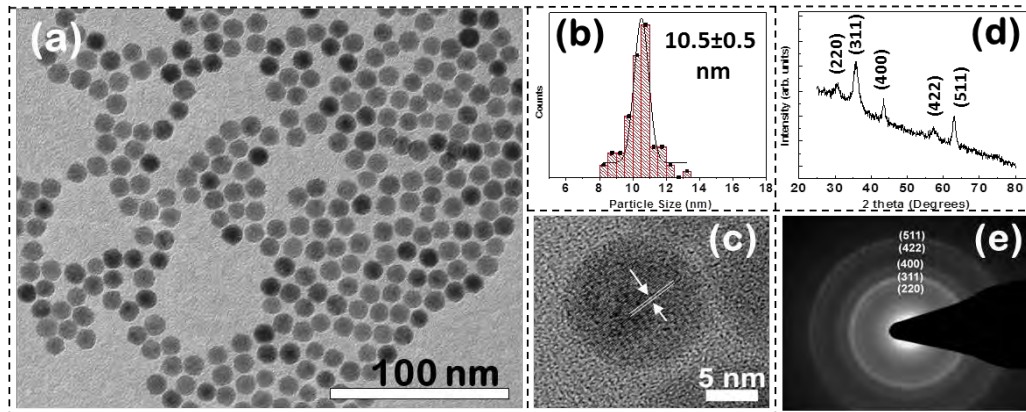
Figure 40: Bright-field TEM image of as-synthesized Fe_3O_4 nanoparticles (a), the corresponding particle size distribution (b), HRTEM image of a single Fe_3O_4 nanoparticle (c), XRD pattern (d) and SAED image of the Fe_3O_4 nanoparticles (e).

Figure 40(a) shows a bright-field TEM image of the synthesized Fe_3O_4 nanoparticles. The nanoparticles are spherical, with an average diameter of 10.5±0.5 nm determined by fitting the distribution obtained after counting more than 200 particles (Figure 40b). The HRTEM image of the nanoparticles (Figure 40c) evidences that the nanoparticles are single crystalline, as the lattice fringes continues without interruption. The calculated distance between the lattice planes in Figure 2c is 2.1 Å, which corresponds to the (400) planes of Fe_3O_4. Figure 40d shows the XRD pattern of the nanoparticles. All peaks are indexed to the characteristic reflections of Fe_3O_4 crystal planes. The average crystalline size, as determined from peak widths using the modified Scherrer's formula, is about 9 nm. This size is very close to that determined from the

TEM, confirming the single crystalline nature of the synthesized particles. Figure 40e shows a selected area electron diffraction (SAED) image of the nanoparticles. All diffraction rings correspond to those of Fe_3O_4, which is consistent with the measured XRD pattern.

These synthesized Fe_3O_4 nanoparticles were then filled inside nanoholes patterned in a polymer film, using a novel magnetic drag and drop procedure. Figure 41a and b show SEM images of the printed nanohole arrays before and after filling with the magnetite particles. As shown in Figure 41c, uniform distribution of Fe_3O_4 nanoparticles still reside in the nanoholes after washing and removing stray particles on the patterned surface. To examine the diameter and depth of the nanoholes, we studied the SEM and AFM images obtained and the average diameter of the nanoholes observed from AFM and SEM were in good agreement. A careful data analysis of the AFM topography images indicated a distribution in diameter that is centered around 95 nm, while SEM images indicates 80 nm.

(a)　　　　　　　　　　(b)　　　　　　　　　　(c)
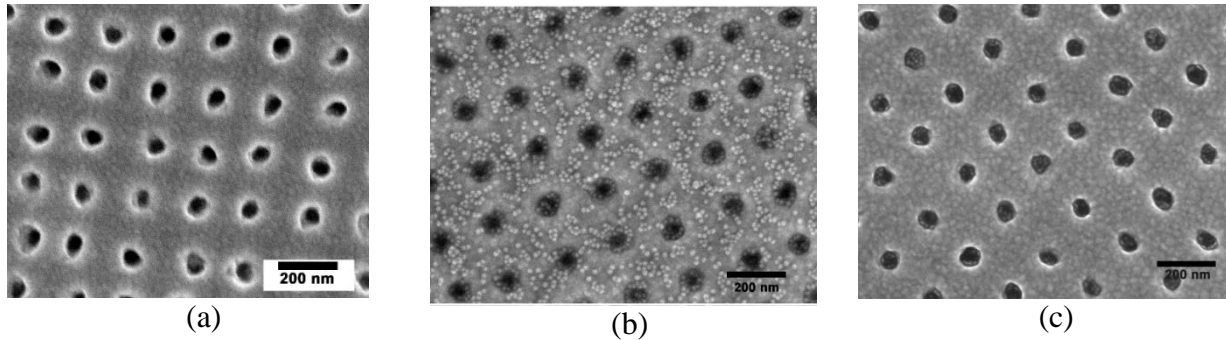
Figure 41: SEM images show arrays of nanoholes (a) before and (b) after filled with Fe_3O_4 nanoparticles and (c) after removing stray particles.

Magnetic measurements were performed on these magnetic nanostructures using the physical property measurement system (PPMS). We have observed that for the as-synthesized Fe_3O_4 nanoparticles, the M-H curves at 300 K do not show any hysteresis (zero coercivity, H_C, and no remnant magnetization, M_r), whereas a clear hysteresis with a coercivity of H_C ~53 mT is observed at 10 K. This is characteristic of the sample of nanoparticles being superparamagnetic at room temperature and entering a ferromagnetic (blocked) state at low temperature, which results in the opening up of the hysteresis loop. However, the case is very different for the Fe_3O_4-filled nanohole film. The M-H curve of this sample at 300 K shows a clear hysteresis, with values of H_C ~30 mT and M_r/M_S ~ 0.2. Our results suggest that other factors in addition to enhanced inter-particle interactions are also important in governing the magnetism of the Fe_3O_4-filled nanohole film.

To confirm this, MFM profiling was performed on the region of the Fe_3O_4-filled nanohole film presented in Figure 42. In our MFM measurements, the constant magnetization of the tip and its oscillation above the sample constitute a force gradient directed perpendicular to the plane of the film. The contrast seen in the MFM image (Figure 42a) can be attributed to an out-of-plane component of the magnetization, which oscillates in up and down directions to reduce the magnetostatic energy, creating magnetic poles of alternating signs that give rise to the lower and higher phase of the tip oscillation. As one can see in this figure, the MFM pattern

evidences the presence of both diametric and in-axis magnetic moments. A signal with higher intensity, shown in white here, from the diametric magnetic moment (white lobes) clearly stands out. To quantify the strength of the magnetic moments, MFM profiles (vertical/horizontal directions) across five holes in Figure 42a were collected. The sharp spike (few nm to 30nm in width) at the center of the line profiles shows the in-axis magnetic moment (Figure 42b). Note that given the small size of the sharp spike, it is difficult to create a profile crossing the spikes in each hole. MFM profiles collected from the planar region across the white lobes at the center of the square matrix are shown in Figure 42c. The strength of the in-axis and diametric magnetic moments collected from the four scan diametric lines in the center of Figure 42a is shown in Figure 42d. It is worth noting that the strength of the magnetic moments is stronger for the "vertical" case (Figure 42b) than for the "diagonal" case (Figure 42d). This can be attributed to the nanohole-nanohole interactions that appear to be stronger at shorter distances between the Fe_3O_4-filled nanoholes in the former case. These findings point to a significant impact of long-range dipolar magnetic interactions between the Fe_3O_4-filled nanoholes on the magnetism of the Fe_3O_4-filled nanohole array, and provide an important understanding of the origin of the enhanced coercivity, as well as the room temperature ferromagnetic-like behavior observed in this novel magnetic nanostructure.
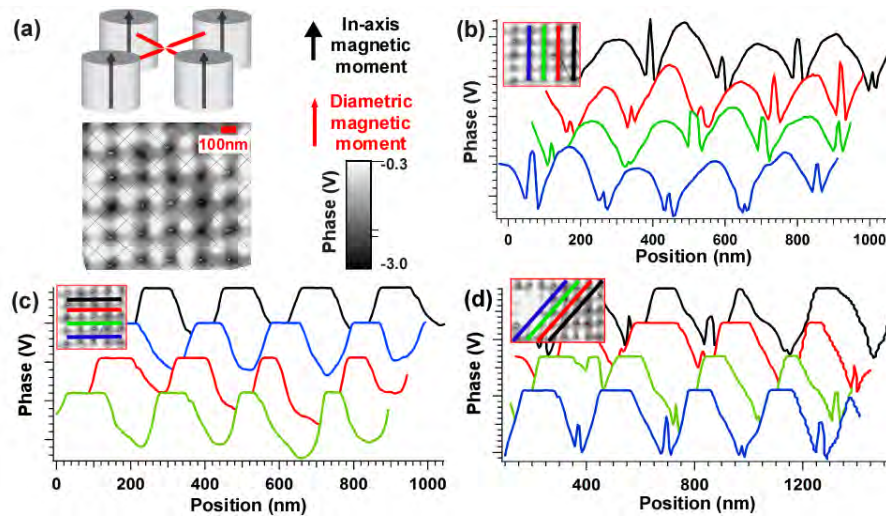
Figure 42: (a) MFM map of about 1µm×1µm area of the sample with nanoholes filled with Fe_3O_4 nanoparticles. The corresponding magnetic moments of interest are depicted in the inset (top: red arrow for the diametric magnetic moment, black arrow for the in-axis magnetic moment). (b-d) Profiles extracted from the MFM image (a): (b) vertically across the nanoholes, (c) horizontally across the white lobes and (d) diagonally across the nanoholes. The locations are depicted in the respective insets (color coded black, red, green, blue).

From a magnetic devices application perspective, the enhancements in H_C and H_K achieved in the highly ordered Fe_3O_4 nanoparticle-filled nanohole arrays are desirable for their use as the magnetic media in high-density magnetic recording applications. A large enhancement of the microwave response is also expected in these highly ordered Fe_3O_4 nanoparticle-filled nanohole arrays, the coercivity and magnetic anisotropy can easily be tuned by varying the size and density of magnetic nanoparticles inside nanoholes. This makes the present nanocomposite

an attractive candidate for high-performance RF sensor and microwave device applications. Recently, the magnetic anisotropy of Fe_3O_4 nanoparticles has also been exploited to improve the detection capacity of single nanoparticles using the MFM technique. In this regard, the use of a highly ordered Fe_3O_4 nanoparticle-filled nanohole array with tunable magnetic anisotropy seems more favorable for biodetection, as each Fe_3O_4 nanoparticle-filled hole can act as a sensing probe and hence detection of multiple different biomarkers/biomolecules can be achieved simultaneously using this array of patterned multi-holes.

In summary, we have developed a new type of magnetic nanostructure using the combined chemistry and SNAP techniques. This novel nanostructure can be ideally used for a wide range of applications, including their use as a biosensing probe for detection of multiple different biomarkers/biomolecules in nanobiomedicine. The main findings of the work have been reported in the journal *Small*, 2014. Our next targets will be to fill nanohole-arrayed films with functional core-shell and hollow iron-oxide nanoparticles, as well as integrating these nanostructures with the radio-frequency magnetoimpedance technology to make a novel biosensing system for applications in biodetection.

Task II: Formation and delivery of functionalized artificial platelets for rapid cessation of internal bleeding

In recent years there has been a surge of interest in the use of multifunctional nanocarriers for improving the efficiency of different biomedical applications [34-45]. When properly engineered, these multifunctional nanocarriers, besides carrying the therapeutic agent (e.g. drugs, genes, donor cells, etc.), can demonstrate a combination of various advantageous properties/functions [35,43]. More specifically, in the field of drug delivery, nanotechnologists combine the carrying capability and stimuli-responsive nature of certain hydrogels with the properties of magnetic nanoparticles (MNPs) to obtain a product that gives both targeted and remote delivery of therapeutic agents. The targeted delivery aspect of the product comes from the force of attraction felt by the MNPs in a static magnetic field, and remote delivery aspect of the product is a consequence of the temperature increase in the vicinity of the MNPs when exposed to an alternating magnetic field (AMF) [46,47]. This temperature increase then leads to a volume phase transition (VPT) of the thermoresponsive polymer prompting it to release the therapeutic payload [34,37].

Thermoresponsive hydrogels such as poly(N-isopropylacrylamide) (PNIPAM) exhibit reversible shrinking or swelling when heated; this makes them attractive candidates for a wide range of controlled release applications like drug delivery and oil separation [48-52]. Biocompatible PNIPAM has a lower critical solution temperature (LCST) of approximately 32 °C due to the presence of both hydrophilic amide and hydrophobic isopropyl and acrylic groups in its monomer structure, NIPAM. Below the LCST, enthalpy dominated PNIPAM is in its hydrophilic conformation and disperses easily in water. However, as the temperature increases the hydrogen bonds responsible for PNIPAM's stability in solution weaken and, above the LCST, PNIPAM precipitates (shrinks) out of solution, being dominated now by entropy [53]. This VPT manifests as an increase in the turbidity of the solution above the LCST (cloud point temperature). The triggering of VPT in PNIPAM is sensitive to changes in the polymer concentration (as long as the concentration is beneath the critical micelle concentration) and the pH (via addition of NaCl, KOH, etc.) of the solution [54, 55].

Practical applications such as drug delivery require remote triggering of PNIPAM hydrogels which can be realized by the heating of magnetic nanoparticles (MNPs) (dispersed in the hydrogel solutions) by exposing them to external radio-frequency (RF), alternating magnetic field (AMF). Typically, the heat generated by MNPs is related to hysteresis losses which are proportional to the magnetic hysteresis loop area described by the magnetic moments of the nanoparticles when exposed to the AMF [56]. Heat generation using biocompatible IO MNPs has been widely studied for efficient magnetic heating (temperature range 40-45 °C) in hyperthermia applications due to their desirable magnetic and inductive heating properties [57-60]. In contrast to the hyperthermia applications where heat damage is initiated by exposing diseased tissue to elevated temperatures for a period of time, drug delivery applications using MNPs embedded in thermo-responsive polymers require controlled heating (temperature change of 4-10 °C) in short time intervals. This is particularly challenging since any excessive heating of the polymer (PNIPAM) can degrade its structural integrity and consequently destroy its reversible VPT behavior.

For most biological applications, it is considered that the suitable size of the IO MNPs should be less than 100 nm [61]. The optimal size is further reduced when considering that larger particles in this range tend to aggregate potentially causing emboli and that they have shorter half-lives in the blood stream due to a triggering of the immune response [62]. Considering this, the use of non-aggregating superparamagnetic IO MNPs (SPIONs) has been favored for biomedical applications [61-63]. Superparamagnetic behavior can be inferred from RT hysteresis loops with a Langevin-like shape showing that there is no coercivity or remanence. For SPIONs, the heat generation under RF fields is primarily attributed to susceptibility losses [56,64]. The magnetic moments of IO MNPs spontaneously reverse direction under the influence of an AMF and in the process transfer the heat energy to the surrounding environment.

Currently the field is somewhat deficient in studies that systematically investigate the VPT of linear PNIPAM when heated by MNPs responding to an AMF. There has been, for example, a study by Zadrazil et. al, in which the release of entrapped oil from PNIPAM hydrogels in response to AMF heating was observed [65]. Similarly, Cejková et. al demonstrated the release of vitamin B12 from PNIPAM microdroplets [66]. However, a pure examination of PNIPAM's VPT in response to AMF heating is missing in these studies, and an emerging important question is how the heating efficiency of MNPs would change once the MNPs are embedded in PNIPAM. Such knowledge is essential to tailor the dual functional response of MNP-embedded PNIPAM composites for a wide range of biomedical applications, including targeted drug delivery.

To address these important issues, we have performed a thorough study on the evolution of the LCST of PNIPAM loaded with SPIONs in response to the remotely triggered heating by a variable AMF. We have analysed the evolution of the LCST as a function of both the polymer and the nanoparticle concentration, and we have also examined the effect of the different ion concentration (ph modification) on the thermal response of PNIPAM.

Materials and Methods

Aqueous solutions were prepared by mixing desired amounts of high purity PNIPAM (99.9 %, mol. wt. 10,000 g/mol, Sigma Aldrich) powder and IO MNPs (99.5 % pure, US Research Nanomaterials, Inc.) in deionized water (DIW) or water that had adjusted KOH dissolved therein at a 0.10 M concentration. Transmission electron microscopy (TEM) of the MNPs dispersed in hexane and drop cast onto Cu grids was carried out with a FEI Morgani system operated at 60 kV acceleration voltage. The MNPs were homogeneously dispersed in the solutions by repeated ultrasonication in ice-bath (to avoid any extrinsic heating). Raman spectra of the prepared solutions (before and after heating) were acquired using a Horiba Jobin Yvon T64000 Advanced Research Raman System equipped with an argon laser operated at 514 nm.

For transmission measurements, 2.0 mL of the dispersed solution was transferred to a polystyrene optical cuvette that was suspended in the RF heating coil. The turbidity change of solution associated with the VPTs in the PNIPAM/IO MNP solutions was detected using a home-made setup (see Figure 43).

Transmission measurements were carried out with a 25 mW He-Ne laser (CW Radiation, Inc.) of 633 nm wavelength. The laser was aligned so as to pass between the loops of the coil and through the optical cuvette as shown in Figure 43. The transmitted laser beam was incident on a

cadmium-sulfide photodetector and the change in resistance was measured as a function of time using a Keithley 2100 Multimeter and LabView programmed for data acquisition. The PNIPAM/IO MNP solutions, within the cuvette, were heated using an AMF at an optimum amplitude of 740 Oe using an Ambrell EasyHeat LI heating system operating at a frequency of 307 kHz. The photodetector and RF heating coil are separated by more than 10 cm so that the
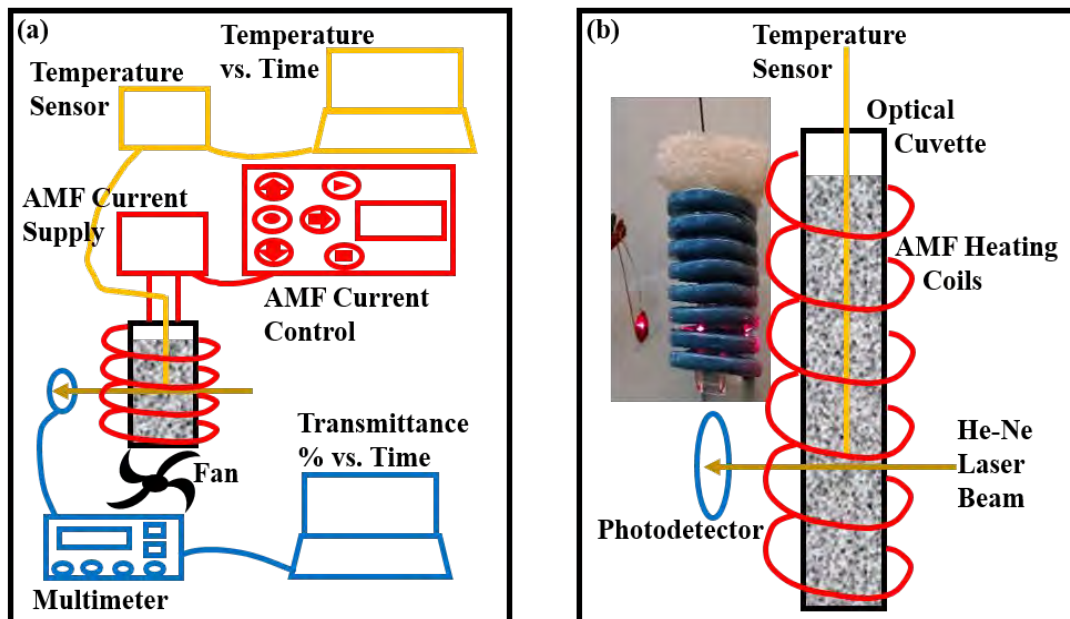
Figure 43: (a) In this custom-built experimental setup, the turbidity of a solution as a function of time can be probed and synchronized with the solution's temperature as a function of time, all while the solution, containing PNIPAM and IO MNPs dispersed in DIW, is subject to an AMF. (b) Note that the He-Ne laser, seen in the inset photograph passes through the AMF heating coils and cuvette to land on the photodetector, probes the solution in proximity to the placement of the temperature sensor so as to ensure the turbidity data correlates to the temperature data.

effect of the AC magnetic field on the photodetector is negligible. The temperature evolution of a given solution was measured as a function of time. Temperature changes in the solution, induced by the RF heating system, were monitored by an optical temperature sensor (Photon Control) with an accuracy of +/- 0.05°C.

Generally, in hyperthermia experiments, there are two sources of heat generated in a sample. What is of interest is the heat generated by the MNPs as a result of their exposure to the AMF. However, systems like the one used in this work employ water cooling of the RF heating coil to reduce the unintentional heating of the sample due to convective heating from the coil. Despite this measure there is still some unintentional heating of the sample that must be corrected for. One established method for calibrating data involves running control trials involving samples of the solvent only and subtracting that heating curve from that of the sample that includes both the solvent and the MNPs [67]. This method, however, is insufficient for the experiments discussed herein. Samples containing PNIPAM are necessarily influenced by the convective heat generated by the RF heating coil. That effect cannot be corrected for

mathematically; it must be physically removed from the experimental system. The setup, therefore, was augmented by the addition of a fan beneath the RF heating coil to supply it with a continuous flow of air which provided additional removal of heat from the coil (see Figure 43). This gave an effective zero slope heating curve when measuring the water background.

Results and Discussion

Characterization of PNIPAM and IO MNP

The size and morphology of IO MNPs was investigated by TEM. The commercially purchased MNPs are shown in Figure 44(a). As can be seen, they are polydisperse and non-uniform in
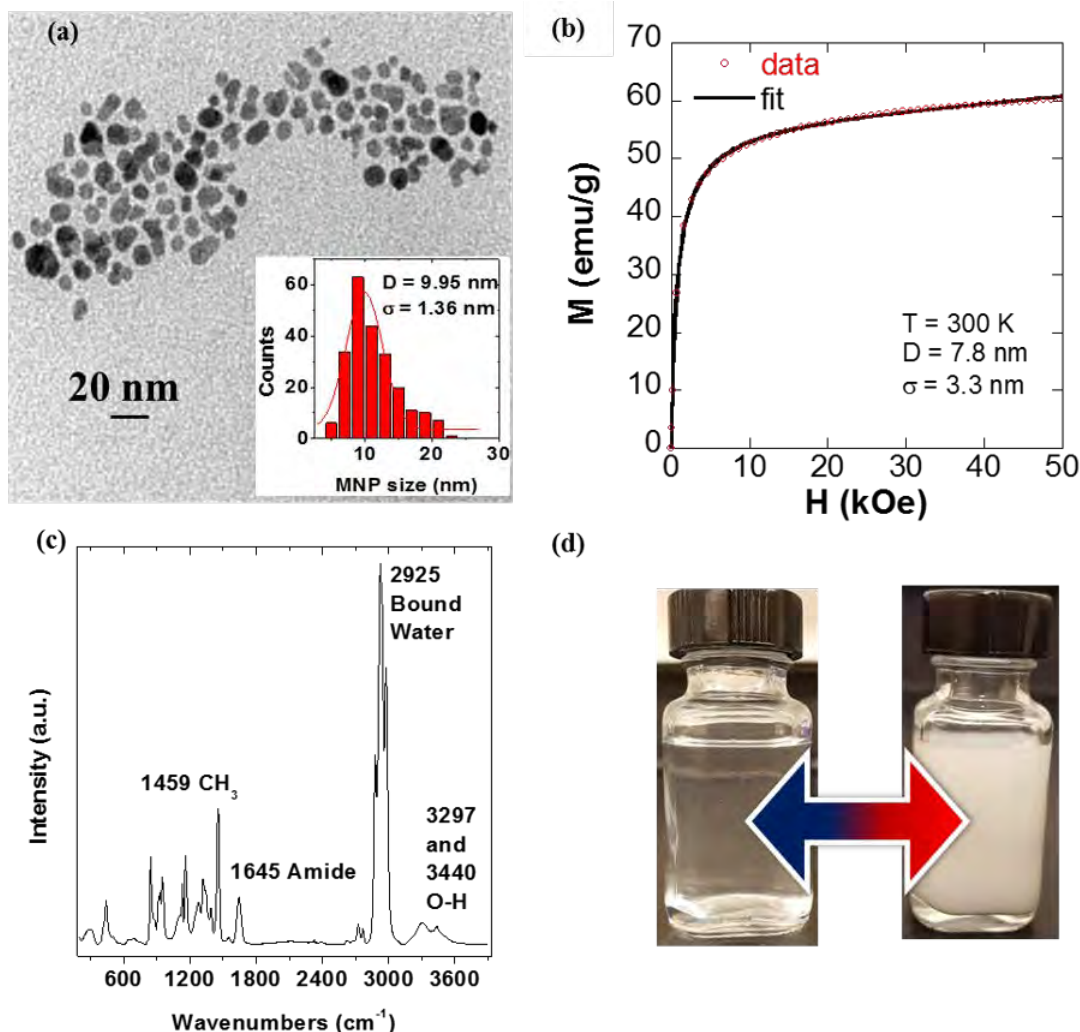
Figure 44: (a) TEM of commercially purchased IO MNPs which have an average size of 9.95 ± 1.36 nm. (b) Magnetization data obtained at 300 K reveals the superparamagnetic nature of the IO MNPs and an average size of 7.8 ± 3.3 nm. (c) Raman spectroscopy of PNIPAM after being subjected to 10 trials of AMF heating reveal the polymer was undamaged during the trials. (d) A 1.0 wt. % aqueous solution of PNIPAM below the LCST appears clear, while the same solution appears turbid when it is heated above its LCST.

shape with an average size of 9.9 ± 1.4 nm. It can also be observed that the nanoparticles are not aggregated, as desired for biomedical applications. In Figure 44 (b) we have plotted the magnetization as a function of applied magnetic field, recorded at room temperature. No coercivity or remanence is observed suggesting that the nanoparticles exhibit a superparamagnetic-like behavior at room temperature.

To confirm this, we fit our hysteresis loops to a standard Langevin expression:

$$M(H) = M_S \int_0^\infty L\left(\frac{\mu H}{k_B T}\right) f(D) dD \,, \tag{1}$$

where D is the diameter of the nanoparticles, $f(D)$ corresponds with a Log-Normal size distribution, and $L(x) = \mathrm{cotanh}(x)-1/x$. As seen from Figure 44 (b), the fitting result is very good, although the apparent size obtained from this fit is a little bit smaller than expected, 7.8 nm. This is likely due to the effect of surface spin disorder which effectively reduces the apparent magnetic size of the nanoparticles. Surface spin disorder is also believed to result in a significantly reduced total magnetization of our MNPs (M_S ~60 emu/g) relative to bulk Fe_3O_4 (M_S ~90 emu/g).

The Raman spectrum of the samples was recorded, and is shown in Figure 44 (c), both before and after ten heating trials to confirm that the PNIPAM was not damaged after several heating/cooling cycles and to establish that the phase change is reversible. Peaks like the one at 1459 cm^{-1} are indicative of the hydrophobic isopropyl part of the monomer while the ones like the peak at 1645 cm^{-1} indicate the hydrophilic amide part of the monomer. The peaks at 3297 cm^{-1} and 3440 cm^{-1} indicate the water is H-bonded to the oxygen atom on the amide. The three most prominent peaks around 2925 cm^{-1} are instructive of the hygroscopic nature of PNIPAM [68].

Finally, in Figure 44 (d) we present an image of the PNIPAM hydrogel before (left) and after (right) the VPT. When the temperature of PNIPAM is less than the LCST the Gibbs free energy is enthalpy dominated, H-bonding between the DIW and amide section is stable allowing the polymer to dissolve in solvent, and the sample appears clear like the left image in Fig. 2(d). On the other hand, if the temperature of PNIPAM rises above the LCST, then the entropy dominated Gibbs free energy leads to disruption of the H-bonding so that the polymer precipitates out of solution, which causes the sample to appear turbid like the right image in Figure 44 (d).

AMF Heating with IO MNPs

Preliminary AMF heating experiments focused on finding the optimum IO MNP concentrations to use in the transmittance experiments discussed in the next two sections. Five samples were prepared in optical cuvette, as described above, with differing IO MNP to DIW mass so that the concentrations investigated ranged from 1 to 5 mg/mL. The change in temperature as a function of time for each of these five concentrations is given in Figure 45 (a). The average of ten trials for each sample is given here. As expected, the higher the concentration of MNPs in solution the more effective the heating of the entire sample is. For example, at 1 mg/mL the solution in cuvette experienced a nearly 7.5 °C temperature increase after being exposed to an AMF for 280 s. At the other end of the IO MNP concentration range, at 5 mg/mL the sample increased nearly 25 °C under the same AMF conditions. However, this data only reports on the global heating of the sample.
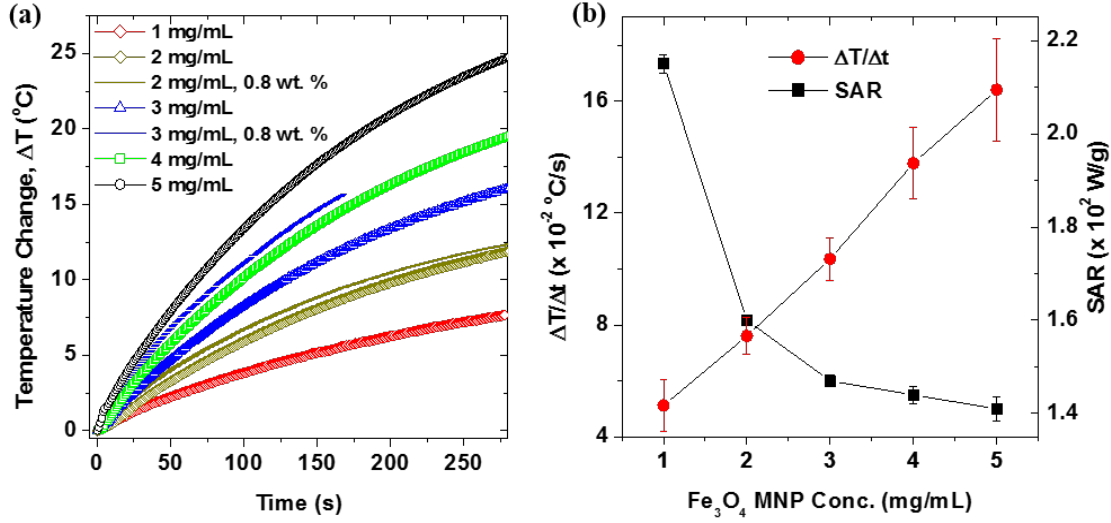
Figure 45: (a) Heating curves of solutions containing IO MNPs dispersed in DIW at concentrations ranging from 1 to 5 mg/mL. Also shown, are the heating curves for a 2 and 3 mg/mL solution that also contains 0.8 wt. % PNIPAM. (b) A comparison of initial linear heating rates and SARs as a function of IO MNP concentration.

In order to comment on the heating efficiency of the nanoparticles one must calculate the specific absorption rate (SAR) which is given by

$$SAR = \frac{c_{sol} m_{sol}}{m_{MNP}} \left(\frac{\Delta T}{\Delta t} \right). \qquad (2)$$

where c_{sol} is the specific heat of the solution, m_{sol} the mass of the solution, m_{MNP} the mass of the nanoparticles, and $\Delta T/\Delta t$ the initial slope of the heating curves. The initial, linear slope of the heating curve and SAR of all five concentrations is plotted as a function of IO MNP concentration in Figure 45 (b). Again, the initial heating rates of the entire sample increases as IO MNP concentration increases. Nevertheless, the SAR decreases with increasing IO MNP concentration. This reduction in the heating efficiency with increasing concentration has been consistently reported in the literature [69] and attributed to the higher aggregation of the nanostructures as their concentration increases, which tends to negatively affect their heating capacity. Considering these results, we decided to focus on the concentration around the crossover region of Figure 45 (b). 2 mg/ml, for our experiments. Selecting 2 mg/mL allows for effective heating of the local environment and relatively slow heating of the sample. In addition, we have also studied the results for the samples with 3 mg/mL IO MNP concentration, which provides for relatively fast heating of the sample, but reduced efficacy of local environment heating, in order to see the differences with respect to 2 mg/ml.

One question that could be raised is how the heating efficiency of the nanoparticles would change once they are embedded in PNIPAM instead of just DIW. To shed light on this, we have measured the heating curves, Figure 45 (a), for samples that contained both IO MNPs and 0.8 wt. % PNIPAM in solution with DIW. Both of these samples showed increased heating

rates as compared to their corresponding sample that had no PNIPAM within it. This suggests that the presence of PNIPAM in solution facilitates the dispersal and disaggregation of IO MNPs leading to a slightly improved heating efficacy. If the PNIPAM had caused the MNPs to aggregate, the samples would have exhibited reduced heating efficiency. This is further supported by Figure 45 (b) in which more concentrated (and thereby, more aggregated) solutions of MNPs are shown to have reduced SAR values.

Probing the LCST of PNIPAM heated with AMF

Figure 46 (a), and 46(b) show the temperature-dependent transmission characteristics at wavelength of 633 nm obtained for two aqueous solutions of PNIPAM with 2 mg/ml and 3 mg/ml of MNPs at various polymer concentrations ranging from 0.3 to 1.0 wt. %. From the data it is evident that the inflection point where the transmittance drops from 100 % to 0 % can be changed by tuning the PNIPAM concentration. The LCSTs for PNIPAM/IO MNP aqueous solutions were determined from maxima of the modulus of the derivatives of transmittance percent (see Figure 46 (d)). When comparing Figure 46 (a) and 46(b), the change in smoothness of the transmission curves can be attributed to the difference in heating rates. At 2 mg/ml, the heating rate is slower than at 3 mg/ml, as was shown in Figure 45 (a) but the transmittance drop takes place in a more abrupt way. This suggests that in order to get a more defined VPT, the heating rate of the nanoparticles must not be too high, and validates our choice of 2 mg/ml as ideal MNP concentration for the experiemen. If we consider that the temperature increment necessary for the VPT to take place to be around 10-15ºC (starting at 25ºC), it can be seen that, according to Figure 46(a), it takes around 150-250 s for the VPT to be completed, depending on the final concentration of MNPs and PNIPAM.

In addition, as shown in Figure 46 (c) a monotonic decrease in the LCST values with increasing PNIPAM concentrations is observed for both 2 mg/mL and 3 mg/mL concentrations of IO MNPs. Thus, this suggests that the rate at which PNIPAM samples are heated by AMF does not affect the LCST. The decreasing trend in the LCST of PNIPAM solutions with increasing concentration is consistent with earlier reports on direct heating (i.e. non-RF heating) of PNIPAM solutions [70]. We have further tested this by determining the LCST of PNIPAM solutions heated using a hot bath rather than AMF heating. This more conventional method of heating PNIPAM yields transition temperatures that are consistent with those of the samples heated with dispersed MNPs that respond to an AMF. This result indicates that the VPT of PNIPAM is not affected by the use of MNPs as a heating source, and therefore confirms them as viable candidates for the remote triggering of the thermal reponse of the PNIPAM.

The concentration dependent variation in PNIPAM's LCST is a consequence of the fact that critical micelle concentration (CMC) has not been reached. This is demonstrated by Figure 46 (d) in which the derivative of transmittance percent as a function of temperature is given for a 1.0 wt. % versus a 0.3 wt. % PNIPAM/IO MNP solution. Note that the lowest PNIPAM concentrations exhibit a change in state that is poorly defined; it is spread over a wide range of temperature and time. Contrast this with highest PNIPAM concentration in which the phase transformation is more narrow and pronounced; it occurs over a narrow range of temperature and time. As the concentration of the polymer increases, the CMC is approached, beyond which the LCST is constant. Unfortunately, with the experimental setup described above, higher concentrations of PNIPAM could not be investigated. This was due to the fact for higher

concentrations, the samples became opaque to the He-Ne laser making transmittance percent data acquisition impossible.
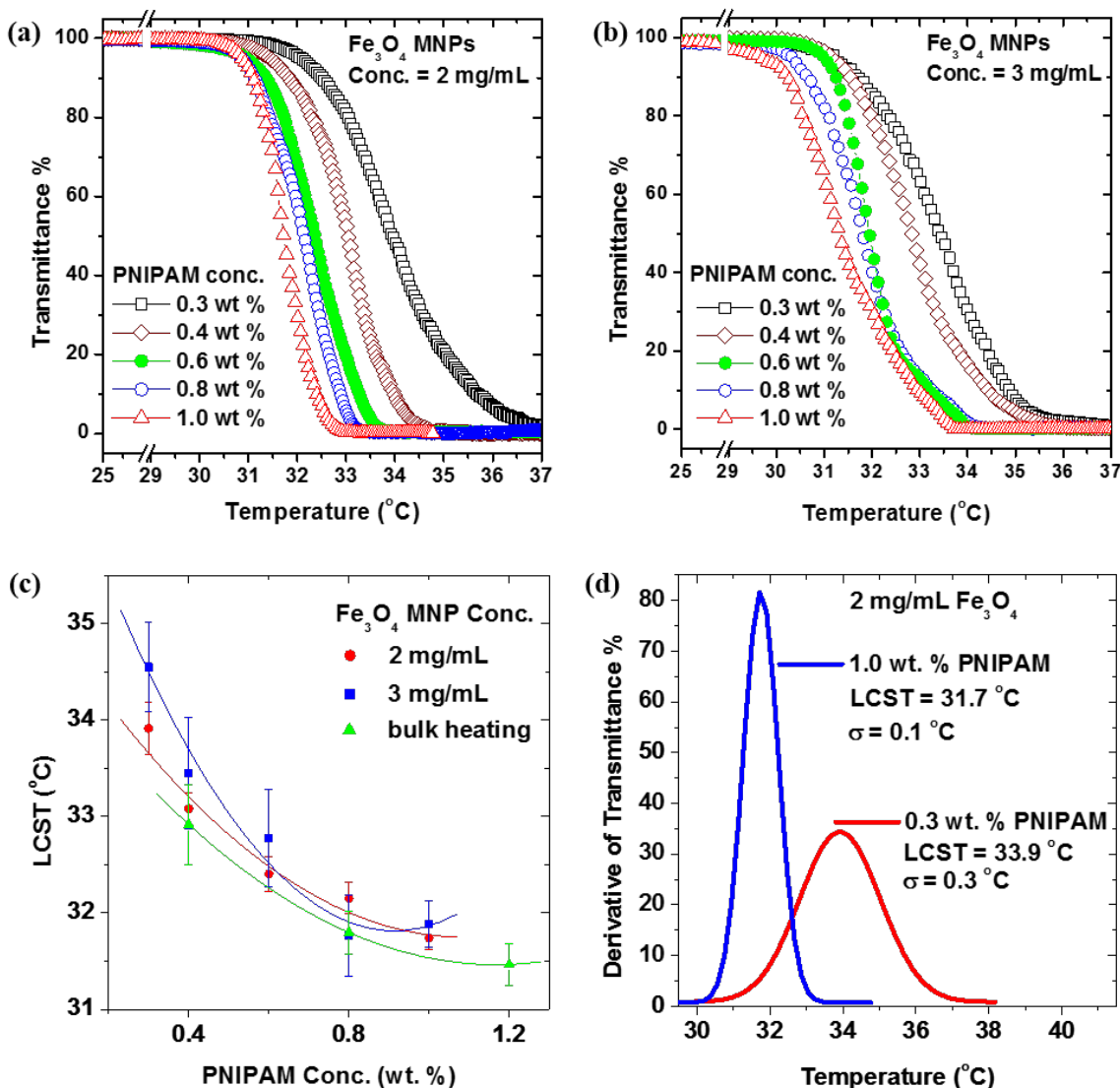
Figure 46: (a) Aqueous PNIPAM concentration study of transmittance percent as a function of temperature for solutions ranging from 0.3 to 1.0 wt. % polymer content and also containing 2 mg/mL IO MNP content. (b) The same as in (a) only with 3 mg/mL IO MNP content for a relatively faster heating rate of PNIPAM. (c) A comparison of the LCSTs found by relatively slow AMF heating (2 mg/mL IO MNP content), relatively fast AMF heating (3 mg/mL IO MPN content), and bulk heating (non-AMF) as a function of PNIPAM concentration. (d) A comparison of the definiteness of the LCST of a 0.3 wt. % versus a 1.0 wt. % aqueous PNIPAM solution.

Effect of Ions on the LCST of PNIPAM Heated with AMF
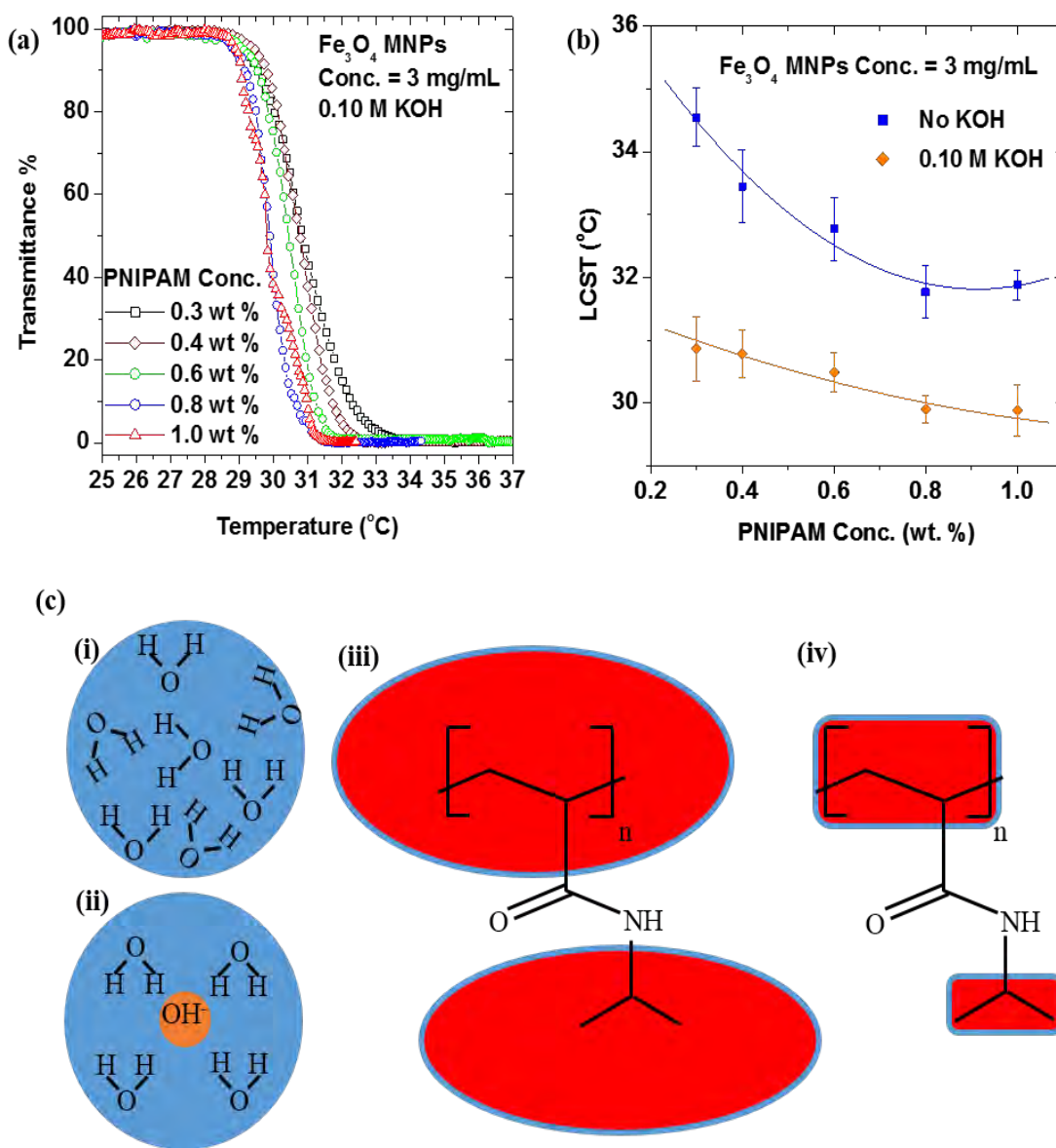
Figure 47: (a) Aqueous PNIPAM concentration study of transmittance percent as a function of temperature for solutions ranging from 0.3 to 1.0 wt. % polymer content and also containing 2 mg/mL IO MNP content.

Blood is known to contain several different ions in solution to facilitate osmotic balance of blood cells. In order to simulate this aspect of blood, adjusted KOH pellets were dissolved into the initial DIW solvent and then PNIPAM and IO MNPs were added to the solution as described previously. This gave the samples, in the experiments described in this section, a 0.10 M KOH concentration. Figure 47 (a) shows the transmittance percent as a function of temperature for PNIPAM concentrations ranging from 0.3 to 1.0 wt. % and a constant IO MNP

concentration of 3 mg/mL. As in the previous section, these samples contained PNIPAM in amounts below the CMC and the decrease in LCST with increasing polymer content is the result. However, compared to the 0 M KOH concentration, Fig. 4 (b), when we increase the KOH concentration to 0.10 M, both the LCST values and the change in LCST as a function of polymer concentration become smaller. This can be even more clearly seen in Figure 47 (a). In Figure 47 (b), the LCSTs in the presence of OH- ions are compared to those, from the previous section in which ions are not present, at the same 3 mg/mL IO MNP concentration. There is an apparent 2-3°C decrease in the LCST of PNIPAM/IO MNP solutions at every PNIPAM concentration when the OH⁻ ions are in solution. This is understood in terms of the "structure maker" influence that OH⁻ ions have on water molecules. The schematic in Figure 47 (c) depicts how water molecules behave in the presence of OH⁻ ion and the implications this has on the thermoresponsive polymer. When no ions are present, water molecules are free to randomly orient themselves. The negative charge of OH⁻ ions make manifest an electric field that the polar water molecules must align themselves within. For an aqueous PNIPAM solution that contains no OH⁻ ions the hydration shells around the hydrophobic acrylic and isopropyl parts of the monomer are relatively swollen since the water molecules are randomly oriented. On the other hand, when the ions are present those same hydration shells are relatively shrunken due to the ordered arrangement of water molecules.

There are two ways in which this can be used to explain the reduced LCST [71]. First consider an isopropyl (or acrylic) section of a NIPAM monomer in solution with OH⁻ ions. Having a smaller hydration shell means less thermal energy is necessary to bring a neighboring isopropyl in proximity. The association of these hydrophobic sections is what ultimately leads to the precipitation of the polymer out of solution. So if this occurs at a reduced thermal energy then the LCST has effectively been reduced. Alternatively, a consideration of the entropy of the system can explain the early onset of LCST. Supposing the hydration shell around the hydrophobic section experiences reduced entropy due to the presence of ions, then the entire system (i.e. the solution) necessarily ends up with increased entropy. This means that the Gibbs free energy of the system becomes entropy dominated earlier as the system heats. Thus the LCST is reduced.

Time Lapse Photographs of Samples Correlated to Transmittance and Temperature Data

In order to further demonstrate the phase transformation of aqueous PNIPAM/IO MNP solutions, time lapse photography of the sample was employed and synchronized with both transmittance percent and temperature as a function of time, as shown in Figure 48 (a) and (b) respectively. This was accomplished with an aqueous 0.8 wt. % PNIPAM and 2 mg/mL IO MNP solution. The camera was focused on a logo which was submerged just beneath the surface of the solution. Images from this sample during the trial are shown in Figure 48 (c). For comparison purposes a control sample, containing no PNIPAM and 2 mg/mL IO MNPs, was prepared and its corresponding images are shown in Figure 48 (d).

Note that at the first marked data point (approximately 20 seconds) virtually all of the He-Ne laser passes through the solution. At this same time the sample is approximately 24 °C and the logo appears clear and centered in the frame. This is because the PNIPAM is below its LCST and is in solution with the DIW. Next, at approximately 120 seconds into the trial, the laser has begun to be blocked to around 90 % of its original intensity. This occurs at almost

31°C (below the LCST) causing the logo to appear slightly hazy and to shift down and to the right in the frame. The image shift is a consequence of the change in refractive index associated with PNIPAM's VPT [72]. The blurring of the logo is due to the increase in the solution's
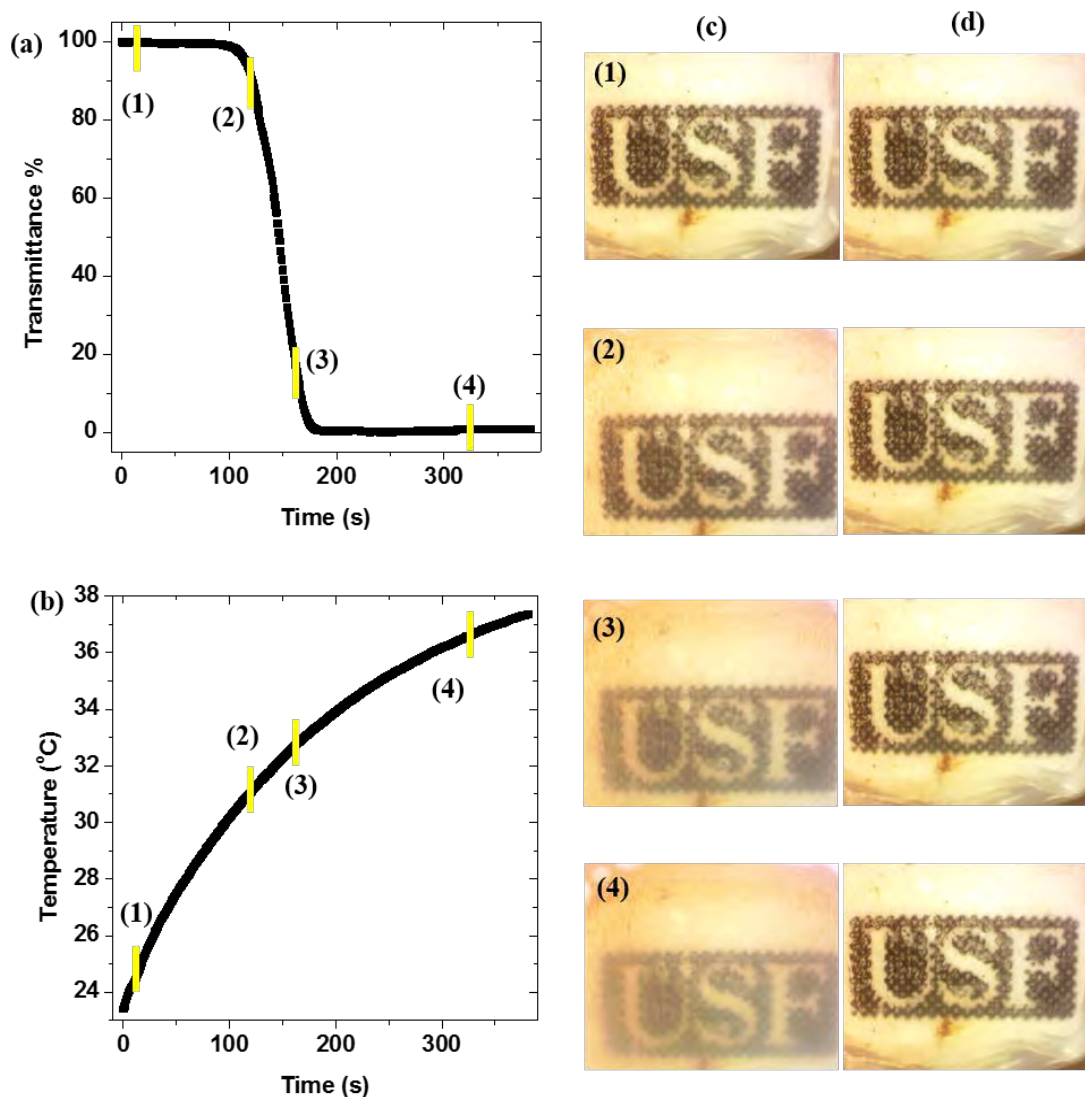
Figure 48: (a) Transmittance percent versus time of a 0.8 wt. % aqueous PNIPAM solution with 2 mg/mL IO MNPs dispersed therein. (b) Temperature as a function of time of the same solution as it is subject to an AMF. (c) Time lapse photographs of a logo submerged beneath the surface of the solution which was taken at the corresponding marked time in the two data sets. (d) Images of the same logo dispersed in a sample that contained no PNIPAM at the same time intervals.

turbidity as the polymer begins to fall out of solution. Then, at nearly 160 seconds, the fraction of He-Ne laser landing on the photodetector is approximately 10 %. At this time the solution is almost 33 °C (above the LCST) which causes the logo to be further obscured. Now most of the polymer has fallen out of solution increasing its turbidity. Finally, at almost 325 s, the laser is fully blocked and the sample has now reached approximately 36 °C (well above the LCST). The logo appears even more turbid than before since now all of the polymer has fallen out of

solution. Note that the control solution exhibits no change in turbidity or refractive index since there was no PNIPAM in the solution and so no VPT takes place.

Conclusions

We have carried out a thorough study of the thermal response of linear PNIPAM when heated by IO MNPs in the presence of an AMF. By comparing the heating rate and SAR curves, the optimal concentration of 10 nm Fe_3O_4 MNPs was determined to be around 2 mg/ml. This concentration was shown to provide a smooth VPT in the range of temperatures around 31-36 ºC for the LCST. When increasing the concentration to 3 mg/ml, the LCST is reached faster, but the transition becomes wider and worse defined. In addition, we have shown that the specific point of LCST can be easily tuned by changing the PNIPAM concentration: a monotonic decrease in the LCST values with increasing PNIPAM concentrations is observed for both 2 mg/mL and 3 mg/mL concentrations of IO MNPs, thus suggesting that the rate at which PNIPAM samples are heated by AMF does not affect the LCST. We have also shown, by introducing OH^- ions into the solution the LCST can be made to decrease by 2-3 $°$ C since the hydration shells around the hydrophobic parts of the polymer are reduced in size. Finally, time lapse photography was utilized to further demonstrate the VPT of PNIPAM. The work described here provides a more solid foundation for the field of targeted biotherapeutic delivery by exploring the VPT behavior of the stimuli responsive polymer prior to its hybridization with the IO MNP.

III. Key Research Accomplishments

Two research tasks were pursued under the two-year extension of the project. The following bulleted items describe the significant research accomplishments for these tasks:

Task 1

- Demonstrated the different impacts of biomaterial coating on the magnetic heating efficiency of Fe_3O_4 nanoparticles. The effect of particle motion on the heating capacity is not significant. These findings are of practical importance in manipulating the properties of these nanoparticles for a wide range of biomedical applications.

- Magnetic properties of $Fe/\gamma-Fe_2O_3$ core/shell nanoparticles and their transformation to core/void/shell and hollow morphologies have been investigated. The possibility of tuning the magnetic properties including the exchange bias effect in these nanostructures by tuning their morphology has been demonstrated. Incorporation of such nanoparticles in a non-magnetic polymer matrix or coating the nanoparticles with a non-magnetic SiO_2 layer has enabled the investigation of the effect of dipolar inter-particle interactions on the magnetization dynamics and hence the EB in these nanostructures.

- An effective approach to improve the sensitivity of inductance coil sensors by designing a sensor core that consists of multiple soft ferromagnetic microwires was attempted. A systematic study of the LEMI effect has been performed in a non-magnetic copper wire coil with a filler composed of multiple Co-rich amorphous microwires. Melt-extracted microwires (MEW) of $Co_{68.2}Fe_{4.3}B_{15}Si_{12.5}$ and glass-coated microwires (GCW) of $Co_{68}B_{15}Si_{10}Mn_7$ with excellent soft magnetic properties were used for this study.

- A new type of magnetic nanostructure using the combined chemistry and SNAP techniques (Spin-on nanoprinting) was developed. This novel nanostructure can be ideally used for a wide range of applications, including their use as a biosensing probe for detection of multiple different biomarkers/biomolecules in nanobiomedicine. The main findings of the work have been reported in the journal *Small*, 2014.

Task II

- Remote triggering of the polymer-magnetic nanoparticle (MNP) aqueous solutions ($PNIPAM/Fe_3O_4$) using RF heating of the constituent Fe_3O_4 MNPs was successfully demonstrated. Optimum MNP size for producing the highest specific absorption rate (SAR) was determined. Controlled remote triggering of the LCST in PNIPAM using Fe_3O_4 MNPs as reported here will be of interest to researchers studying thermo-responsive polymers for targeted and controlled release in drug delivery.

- Possibility of altering the sol-to-gel transition (Lower Critical Solution Temperature) by adding KOH was investigated. Ability to change LCST is important in order to adjust the transition temperature within the range of tolerable temperatures for biological systems.

- The mechanism of heat generation by MNP in presence of an alternating magnetic field, such as RF radiation, was investigated. We found that the PNIPAM/Fe$_3$O$_4$ MNP composites exhibit constant Néel relaxation and increased Brownian relaxation with increasing polymer concentration. Therefore, Néel relaxation dominates the Brownian relaxation of PNIPAM/Fe$_3$O$_4$ MNP heating. These results will be interesting to researchers who require controlled heating of drug delivery composite materials.

- Time lapse photography was utilized to further demonstrate the volume phase transition (VPT) of PNIPAM. The work provides a more solid foundation for the field of targeted biotherapeutic delivery by exploring the VPT behavior of the stimuli responsive polymer prior to its hybridization with the IO MNP.

IV. Reportable Outcomes

The following sections list book chapters, publications, presentations, patent-related activity, professional activities, students graduated, student awards/scholarships and impact of grant-funded research acknowledging support from CIFM through grant USAMRMC W81XWH-07-1-0708 and/or continuation grant USAMRMC W81XWH1020101/3349 (participating CIFM faculty and postdoctoral contributors are shown in bold, while CIFM student contributors are italicized):

Book chapters:

1. *K. Stojak*, **H. Srikanth**, **P. Mukherjee**, **M.H. Phan** and N.T.K. Thanh, Size- and Shape-Variant Magnetic Nanoparticles: Synthesis and Characterisation for Biomedical Applications, in **Metal Nanoparticles of Complex Morphologies, Bottom up Synthesis to Applications**, (2012) Ed. Tapan K. Sau and Andrey L. Rogach, Wiley, Chapter 6.

2. "Laser Ablation for Multiferroic Heterostructures", **D. Mukherjee**, **S. Witanachchi**, and **P. Mukherjee**, in *Laser Ablation: Fundamentals, Methods and Applications*, NOVA Publishers (in press).

Journal Publications:

1. "Magneto-reactance based detection of MnO nanoparticle-embedded Lewis lung carcinoma cancer cells," *J. Devkota*, M. Howell, S. Mohapatra, **P. Mukherjee**, **H. Srikanth**, **M.H. Phan**, *Journal of Applied Physics* **117**, 17D123 (2015)

2. "Superparamagnetic properties of carbon nanotubes filled with $NiFe_2O_4$ nanoparticles" - *K. Stojak Repa*, J. Alonso, **M.H. Phan**, **H. Srikanth**, E. M. Palmero, M. Vazquez, *Journal of Applied Physics* **117**, 17C723 (2015)

3. "Anisotropy effects in magnetic hyperthermia: A comparison between spherical and cubic exchange-coupled FeO/Fe_3O_4 nanoparticles," **H. Khurshid**, **J. Alonso**, *Z. Nemati*, **M.H. Phan**, **P. Mukherjee**, M. L. Fdez-Gubieda, J. M. Barandiarán, and **H. Srikanth,** *Journal of Applied Physics* **117**, 17A337 (2015)

4. "FeCo nanowires with enhanced heating powers and controllable dimensions for magnetic hyperthermia," **H. Khurshid**, **J. Alonso**, *V. Sankar*, *Z. Nemati*, **M.H. Phan**, **H. Srikanth**, E. Garayo, J.A. García, *Journal of Applied Physics* **117**, 17D113 (2015)

5. "From core-shell to hollow $Fe/\gamma\text{-}Fe_2O_3$ nanoparticles: evolution of the magnetic behavior", *Z. Nemati*, **H. Khurshid**, **J. Alonso**, **M.H. Phan**, **P. Mukherjee**, **H. Srikanth**, *Nanotechnology* **26**, 406705 (2015)

6. "A novel approach for detection and qualification of magnetic nanomarkers using a spin valve GMR-integrated microfluidic biosensor," *J. Devkota*, G. Kokkinis, T. Berris, S. Cardoso, F. Cardoso, **H. Srikanth**, **M.H. Phan**, I. Giouroudi, *RSC Advances* **5**, 51169 (2015)

7. "Spin-glass-like freezing of inner and outer surface layers in hollow alpha-Fe_2O_3 nanoparticles," **H. Khurshid**, *P. Lampen-Kelley*, Òscar Iglesias, **J. Alonso**, **M.H.**

Phan, M.L Saboungie, Chengjun Sun, and **H. Srikanth**, *Nature Publishing Group: Scientific Reports* **5**, 15054 (2015)

8. "Intrinsic Anomalous Ferroelectricity in Vertically-Aligned $LiNbO_3$-type $ZnSnO_3$ Hybrid Nanoparticle-Nanowire Arrays", **D. Mukherjee**, A. Datta, C. Kons, *M. Hordagoda*, **S. Witanachchi** and **P. Mukherjee**, *Applied Physics Letters,* 2014. (*accepted*)

9. "Evidence of Superior Ferroelectricity in Structurally Welded $ZnSnO_3$ Nanowire Arrays", A. Datta, **D. Mukherjee**, C. Kons, **S. Witanachchi** and **P. Mukherjee**, *Small* **10**, 4093 (2014).

10. "On-the-surface photoconductive response of pelletized thin In_2S_3 nanosheets", A. Datta, **D. Mukherjee**, **S. Witanachchi** and **P. Mukherjee**, *Materials Research Bulletin*, **55**, 176-181 (2014).

11. "Hierarchically-Ordered Nano-Heterostructured PZT Thin Films with Enhanced Ferroelectric Properties", A. Datta, **D. Mukherjee**, **S. Witanachchi** and **P. Mukherjee**, *Advanced Functional Materials* **24**, 2638-2647 (2014).

12. "Enhanced magnetism and ferroelectricity in epitaxial $Pb(Zr_{0.52}Ti_{0.48})O_3$ /$CoFe_2O_4$ / $La_{0.7}Sr_{0.3}MnO_3$ multiferroic heterostructures grown using dual-laser ablation technique", **D. Mukherjee**, *M. Hordagoda*, P. Lampen, **M. H. Phan**, **H. Srikanth**, **S. Witanachchi**, and **P. Mukherjee**, *Journal of Applied Physics* **115**, 17D707 (2014).

13. "Enhanced Magnetism in Highly Ordered Magnetite Nanoparticle-filled Nanohole Arrays" - B. Duong, **H. Khurshid**, P. Gangopadhyay, *J. Devkota*, *K. Stojak*, **H. Srikanth**, L. Tetard, R. Norwood, N. Peyghambarian, **M.H. Phan**, and J. Thomas, *Small* **10**, 2840 (2014)

14. "Tuning Exchange Bias in $Fe/\gamma Fe_2O_3$ Core-Shell Nanoparticles: Impacts of Interfacial Frozen and Surface Spins" - **H. Khurshid**, **M.H. Phan**, **P. Mukherjee**, **H. Srikanth**, *Applied Physics Letters* **104**, 072407 (2014)

15. "Synthesis, inductive heating, and magnetoimpedance-based detection of multifunctional Fe_3O_4 nanoconjugates" *J. Devkota*, T.T.T. Mai, *K. Stojak*, P.T. Ha, H.N. Pham, X.P. Nguyen, **P. Mukherjee**, **H. Srikanth**, and **M.H. Phan**, *Sensors and Actuators B: Chemical* 190, 715 (2014)

16. "Exchange bias effect in Au-Fe_3O_4 Composite Nanoparticles" - *S. Chandra*, N. A. Frey, **M.H. Phan**, S. Srinath, Y. Lee, C. Wang, S. Sun, M. A. Garcia, and **H. Srikanth,** *Nanotechnology* 25, 055702 (2014)

17. "Magneto-impedance Based Probe of Various Concentrations of Corrosive Chemicals" - *J. Devkota*, N.T. Huong, **H. Srikanth**, and **M.H. Phan**, *IEEE Transactions on Magnetics* **50**, 4004404 (2014)

18. "Impact of coating amorphous and crystalline cobalt ferrite films on the magneto-impedance response of a soft ferromagnetic amorphous ribbon," **D. Mukherjee**, *J. Devkota*, *A. Ruiz*, **S. Witanachchi, P. Mukherjee, H. Srikanth,** and **M.H. Phan,** *Journal of Applied Physics* **116**, 123912 (2014)

19. "A highly sensitive magnetic biosensor for detection and quantification of anticancer drugs tagged to superparamagnetic nanoparticles" - *J. Devkota*, *J. Wingo*, T. T. T. Mai, X. P. Nguyen, N. T. Huong, **P. Mukherjee**, **H. Srikanth**, and **M.H. Phan**, *Journal of Applied Physics* **115**, 17B503 (2014)

20. "Tailoring magnetic and microwave absorption properties of glass-coated soft ferromagnetic amorphous microwires for microwave energy sensing" - *J. Devkota*, P. Colosimo, A. Chen, V.S. Larin, **H. Srikanth**, and **M.H. Phan,** *Journal of Applied Physics* **115**, 17A525 (2014)

21. "Impacts of surface spins and inter-particle interactions on the magnetism of hollow γ-Fe_2O_3 nanoparticles" - **H. Khurshid**, *Z. N. Porshokouh*, **M.H. Phan**, **P. Mukherjee**, and **H. Srikanth**, *Journal of Applied Physics* **115**, 17E131 (2014)

22. "Sensing RF and microwave energy with fiber Bragg grating heating via soft ferromagnetic glass-coated microwires" - P. Colosimo and A. Chen, *J. Devkota*, **H. Srikanth**, and **M.H. Phan**, *Sensors and Actuators A: Physical* **210**, 25 (2014)

23. "A soft ferromagnetic multiwire-based inductance coil sensor for advanced sensing applications" - *J. Devkota*, L. Trang, J. Liu, F. Qin, J. Sun, **P. Mukherjee**, **H. Srikanth**, and **M.H. Phan**, *Journal of Applied Physics* (2014, to be published)

24. **H. Khurshid**, *S. Chandra*, W. Li, G. C. Hadjipanayis, **P. Mukherjee**, **M.H. Phan**, and **H. Srikanth,** "Mechanism and Controlled Growth of Shape and Size Variant Core/Shell FeO/Fe_3O_4 Nanoparticles", *Nanoscale* 5, 7942 (2013)

25. **H. Khurshid**, *S. Chandra*, **P. Mukherjee**, and **H. Srikanth,** "Synthesis and Magnetic Properties of Hybrid Nanostructures of $Pt-Fe_xO_y$", *Journal of Materials Chemistry C* 1, 6553 (2013)

26. *N. A. Frey-Huls*, **M. H. Phan**, A. Kumar, S. Mohapatra, S. S. Mohapatra, **P. Mukherjee** and **H. Srikanth**, "Transverse susceptibility as a biosensor for detection of nanoparticle-embedded human embryonic kidney cells", *Sensors* 13, 8490 (2013)

27. *J. Devkota*, *A. Ruiz*, **P. Mukherjee**, **H. Srikanth**, and **M.H. Phan**, "Magneto-resistance, magneto-reactance, magneto-impedance effects in single and multi-wire systems", *Journal of Alloys and Compounds* **549**, 295 (2013)

28. *J. Devkota*, *A. Ruiz*, C. Wang, S. Mohapatra, **P. Mukherjee**, **H. Srikanth**, and **M.H. Phan**, "Detection of low-concentration superparamagnetic nanoparticles using an integrated radio frequency magnetic biosensor," *Journal of Applied Physics* **113**, 104701 (2013)

29. *A. Ruiz*, **D. Mukherjee**, *J. Devkota*, *M. Hordagoda*, **S. Witanachchi**, **P. Mukherjee**, **H. Srikanth**, and **M.H. Phan**, "Enhanced GMI effect in soft ferromagnetic amorphous ribbons with pulsed laser deposition of cobalt ferrite", *Journal of Applied Physics* **113**, 17A323 (2013)

30. **H. Khurshid**, *S. Chandra*, W. Li, G. C. Hadjipnayis, **P. Mukherjee**, **M. H. Phan**, and **H. Srikanth,** "Synthesis and magnetic properties of core/shell FeO/Fe_3O_4 nano-octopods", *Journal of Applied Physics* **113**, 17B508 (2013)

31. *J. Devkota*, *A. Ruiz*, **P. Mukherjee**, **H. Srikanth**, and **M.H. Phan**, "Magneto-impedance biosensor with enhanced sensitivity for highly sensitive detection of Nanomag-D beads", *IEEE Transactions on Magnetics 49,* 4060 (2013)

32. *J. Devkota, A. Ruiz, J. Wingo*, F.X. Qin, **P. Mukherjee**, **H. Srikanth**, **M.H. Phan**, "Soft ferromagnetic microribbons with enhanced GMI properties for high frequency sensor applications," *Physics Express* 4, 10 (2013)

33. N.H. Hong, A.T. Raghavender, O. Ciftja, **M.-H. Phan,** *K. Stojak,* **H. Srikanth,** Y.H. Zhang, "Ferrite nanoparticles for future heart diagnostics", *Applied Physics A: Materials Science and Processing 112*, 323 (2013).

34. S. Datta, *S. Chandra,* S. Samanta, K. Das, **H. Srikanth,** B. Ghosh, "Growth and physical property study of single nanowire (diameter 45 nm) of half doped manganite " - *Journal of Nanomaterials 2013*, 162315 (2013)

35. **D. Mukherjee**, *M. Hordagoda*, *R. Hyde*, *N. Bingham*, **H. Srikanth**, **S. Witanachchi**, and **P. Mukherjee**, "Nano-columnar Interfaces and Enhanced Magnetic Coercivity in Preferentially-oriented Cobalt ferrite Thin Films grown using Oblique-angle Pulsed Laser Deposition", **ACS Applied Materials and Interfaces**, 5(15), 7450 (2013)

36. **A. Datta**, **D. Mukherjee**, *M. Hordagoda*, **S. Witanachchi**, and **P. Mukherjee**, "Controlled Ti Seed Layer Assisted Growth and Field Emission Properties of $Pb(Zr_{0.52}Ti_{0.48})O_3$ Nanowire Arrays", **ACS Applied Materials and Interfaces**, 5(13), 6261 (2013)

37. A. Ruiz, **D. Mukherjee**, *J. Devkota*, *M. Hordagoda*, **S. Witanachchi**, **P. Mukherjee**, **H. Srikanth**, and **M.H. Phan**, "Enhanced GMI effect in soft ferromagnetic amorphous ribbons with pulsed laser deposition of cobalt ferrite", **Journal of Applied Physics**, 113, 17A323 (2013)

38. **A. Datta**, **D. Mukherjee**, **S. Witanachchi**, and **P. Mukherjee**, "Low temperature synthesis, optical and photoconductance properties of nearly monodisperse thin In_2S_3 nanoplatelets", **RSC Advances** 3, 141 (2013)

39. **A. Datta** and **G.S. Nolas**, "Nanostructuring and Porosity in Anisotropic Thermoelectric Materials Prepared by Bottom-Up Processing" in Thermoelectric Nanomaterials, eds. K. Koumoto and T. Mori, Springer-Verlag, Berlin, 2013

40. **H. Khurshid,** W. Li, **M.H. Phan, P. Mukherjee, H. Srikanth**, and G.C. Hadjipanayis, "Surface spin disorder and exchange-bias in hollow maghemite nanoparticles", *Applied Physics Letters 101*, 022403 (2012)

41. *S. Chandra*, **H. Khurshid,** W. Li, G. C. Hadjipnayis, **M. H. Phan,** and **H. Srikanth**, "Spin dynamics and criteria for onset of exchange bias in superspin glass Fe/γ-Fe$_2$O$_3$ core-shell nanoparticles", *Physical Review B 86*, 014426 (2012)

42. - *A. Chaturvedi, K. Stojak, N. Laurita,* **P. Mukherjee**, **H. Srikanth** and **M. H. Phan**, "Enhanced magnetoimpedance effect in Co-based amorphous ribbons coated with carbon nanotubes", *Journal of Applied Physics* **111**, 07E507 (2012)

43. *S. Chandra,* A. I. Figueroa, Barnali Ghosh, A. K. Raychaudhuri, **M. H. Phan, P. Mukherjee** and **H. Srikanth**, "Fabrication and magnetic response probed by RF transverse susceptibility in La$_{0.67}$Ca$_{0.33}$ MnO$_3$ nanowires", *Physica B: Condensed Matter* **407**, 175 (2012)

44. *S. Chandra*, **H. Khurshid, M.H. Phan,** and **H. Srikanth,** "Asymmetric hysteresis and its dependence on magnetic anisotropy in exchange biased Co/CoO core-shell nanoparticles", *Applied Physics Letters* **101**, 232405 (2012)

45. **D. Mukherjee**, *N. Bingham*, *M. Hordagoda*, **M. H. Phan**, **H. Srikanth**, **S. Witanachchi**, and **P. Mukherjee**, "Influence of microstructure and interfacial strain on the magnetic properties of epitaxial Mn$_3$O$_4$/La$_{0.7}$Sr$_{0.3}$MnO$_3$ layered-composite thin films", **Journal of Applied Physics** 112, 083910 (2012)

46. **D. Mukherjee**, *M. Hordagoda*, *N. Bingham*, **H. Srikanth**, **P. Mukherjee** and **S. Witanachchi**, "Challenges in the polycrystalline and epitaxial growth of stoichiometric PbZr$_{0.52}$Ti$_{0.48}$O$_3$/La$_{0.7}$Sr$_{0.3}$MnO$_3$ multiferroic heterostructures using pulsed laser ablation", **Journal of Applied Physics** 112, 064101 (2012)

47. **D. Mukherjee**, **S. Witanachchi**, *R. Hyde*, and **P. Mukherjee**, "Advantages of Dual-laser Ablation in the Growth of Multicomponent Thin Films", **American Institute of Physics Conference Proceedings** 1464, 325 (2012)

48. **D. Mukherjee**, *R. Hyde*, **P. Mukherjee**, **H. Srikanth**, and **S. Witanachchi**, "Role of dual-laser ablation in controlling the Pb depletion in epitaxial growth of Pb(Zr$_{0.52}$Ti$_{0.48}$)O$_3$ thin films with enhanced surface quality and ferroelectric properties", **Journal of Applied Physics** 111, 064102 (2012)

49. **D. Mukherjee**, **P. Mukherjee**, **H. Srikanth**, and **S. Witanachchi**, "Carrier-mediated Interaction of Magnetic Moments in Oxygen Vacancy Controlled Epitaxial Mn doped ZnO Thin Films.", **Journal of Applied Physics** 111, 07C318 (2012)

50. **D. Mukherjee**, *N. Bingham*, **M. H. Phan**, **H. Srikanth**, **P. Mukherjee**, and S**. Witanachchi**, "Ziz-zag interface and strain-influenced ferromagnetism in epitaxial $Mn_3O_4/La_{0.7}Sr_{0.3}MnO_3$ thin films grown on SrTiO3 (100) substrates", **Journal of Applied Physics** 111, 07D730 (2012)

51. N.H. Hong, C.-K. Park, A. T. Raghavender, O. Ciftja, *N.S. Bingham,* **M.H. Phan**, and **H. Srikanth,** "Room temperature ferromagnetism in monoclinic Mn-doped ZrO_2 thin films", *Journal of Applied Physics 111,* 07C302 (2012)

52. *N.S. Bingham, P. Lampen,* T.L. Phan, **M.H. Phan**, S.C. Yu, and **H. Srikanth**, "Magnetocaloric effect and refrigerant capacity in $Sm_{1-x}Sr_xMnO_3$ (x=0.42, 0.44, 0.46) manganites", *Journal of Applied Physics 111*, 07D705 (2012)

53. *P. Lampen,* A. Puri, **M.H. Phan**, and **H. Srikanth**, "Structure, magnetic, and magnetocaloric properties of amorphous and crystalline $La_{0.4}Ca_{0.6}MnO_{3+\delta}$ nanoparticles", *Journal of Alloys and Compounds* 94, 512 (2012)

54. **A. Datta,** *A. Popescu,* **L. Woods,** and **G.S. Nolas**, "The Bottom-Up Approach To Bulk Thermoelectric Materials with Nano-Scale Domains", Ch. 14, CRC Handbook: Thermoelectrics and its Energy Harvesting, edited by D.M. Rowe, CRC Press, Boca Raton, 2012

55. **A. Datta** and **G.S. Nolas**, "Solution-Based Synthesis & Low-Temperature Transport properties of $CsBi_4Te_6$", Applied Materials & Interfaces. **4**, 772 (2012)

56. **A. Datta** and **G.S. Nolas**, "Synthesis and Characterization of Nanoncrystalline $FeSb_2$ for Thermoelectric Applications", Eur. J. Inorg. Chem. 55 (2012)

57. *K. Stojak,* **S. Pal**, **H. Srikanth**, C. Morales, J. Dewdney, J. Wang, T. Weller, "Polymer nanocomposites exhibiting magnetically tunable microwave properties", *Nanotechnology* **22**, 135602 (2011)

58. C. Morales, J. Dewdney, **S. Pal***, K. Stojak*, **H. Srikanth**, J. Wang and T. Weller, "Magnetically tunable nanocomposites for microwave applications", *IEEE Transactions of Microwave Theory and Techniques* 59, 302 (2011)

59. *N. Laurita, A. Chaturvedi*, C. Bauer, P. Jayathilaka, Alex Leary, C. Miller, **M.H. Phan**, M.E. McHenry and **H. Srikanth**, "Enhanced GMI effect and field sensitivity in Co-coated soft ferromagnetic amorphous ribbons", *Journal of Applied Physics 109*, 07C706 (2011)

60. *A. Chaturvedi***,** *N. Laurita*, A. Leary, **M.H. Phan**, M.E. McHenry and **H. Srikanth**, "Giant magnetoimpedance and field sensitivity in amorphous and nanocrystalline $(Co_{1-x}Fe_x)_{89}Zr_7B_4$ (x =0, 0.025, 0.05, 0.1) ribbons", *Journal of Applied Physics 109*, 07B508 (2011)

61. A.I. Figueroa, *S. Chandra*, **M.H. Phan**, **H. Srikanth**, C. M. Bonilla, L.M. García, F. Bartolomé, J. Bartolomé, and J. Herrero-Albillos, **"**Magnetic switching and magnetic transitions in $ErCo_2$ probed by radio frequency transverse susceptibility", ***Journal of Applied Physics 109***, 07E118 (2011)

62. *M.B. Morales*, **S. Pal**, *N.A. Frey*, **M.H. Phan**, **P. Mukherjee**, and **H. Srikanth,** "Origin of Magnetic Anomalies in the Liquid, Mixed and Frozen States of Ferrofluids" ***Physics Express*** 2011;1:247 (5 pages)

63. **D. Mukherjee**, **T. Dhakal**, **M. H. Phan**, **H. Srikanth**, **P. Mukherjee**, and **S. Witanachchi**, "Role of crystal orientation on the magnetic properties of $CoFe_2O_4$ thin films grown on Si (100) and Al_2O_3 (0001) substrates using pulsed laser deposition", **Physica B: Condensed Matter** 406, 2663 (2011)

64. *T. Wangensteen*, **T. Dhakal**, *M. Merlak***, M .H. Phan**, **P. Mukherjee, and S. Witanachchi**, "Growth of uniform ZnO nanoparticles by a microwave plasma process", **Journal of Alloys and Compounds**, 509   Issue: 24   Pages: 6C859-6863 (2011)

65. *A. Chaturvedi, S. Stefanoski,* **M.H. Phan**, **George S. Nolas**, and **H. Srikanth**, "Table-like magnetocaloric effect and enhanced refrigerant capacity in $Eu_8Ga_{16}Ge_{30}$-EuO composite materials", ***Applied Physics Letters*** 99, 162513 (2011)

66. **M.H. Phan**, V. Franco, *A. Chaturvedi, S. Stefanoski,* **G.S. Nolas**, and H. **Srikanth,** "Origin of the magnetic anomaly and tunneling effect of europium on the ferromagnetic ordering in $Eu_8Ga_{16}Ge_{30}$ type-I clathrates", ***Physics Review B,*** 84, 054436 (2011)

67. *A. Popescu*, **A. Datta, G. S. Nolas,** and **L. M. Woods**, "Thermoelectric properties of Bi-doped PbTe composites", J. Appl. Phys. 109, 103709 (2011)

68. **A. Datta**, and **G. S. Nolas**, "Composition controlled synthesis of Bi rich Bi1-xSbx alloy nanocrystals by a low temperature polyol process", **Cryst. Eng. Comm.** 13, 2753 (2011).

69. *A. Chaturvedi*, **T. Dhakal**, A.-T. Le, **S. Witanachchi**, **M.H. Phan** and **H. Srikanth,** "Critical length and giant magnetoimpedance in Co-Fe-Ni-Si-B amorphous ribbons", ***Materials Science and Engineering B 172***, 146 (2010)

70. *A. Chaturvedi*, **T. Dhakal**, A.-T. Le, **S. Witanachchi**, **M.H. Phan** and **H. Srikanth**, "Correlation between magnetic softness, sample surface and magneto-impedance in $Co_{69}Fe_{4.5}X_{1.5}Si_{10}B_{15}$ (X = Ni, Al, Cr) amorphous ribbons", ***Physica B: Condensed Matter 405***, 2836 (2010)

71. A. T. Le, N. Q. Hoa, D. G. Park, **M. H. Phan**, **H. Srikanth** and S. C. Yu, "Enhancement of the giant magnetoimpedance effect and its magnetic response in ion-irradiated amorphous ribbons", ***Materials Science and Engineering B 166***, 89 (2010)

72. V. Franco, A. Conde, D. Sidhaye, B. L. V. Prasad, P. Poddar, S. Srinath, **M. H. Phan** and **H. Srikanth**, "Field dependence of the magnetocaloric effect in core-shell nanoparticles", *Journal of Applied Physics 107*, 09A910 (2010)

73. *D. Mukherjee*, **T. Dhakal**, *R. Hyde*, **P. Mukherjee**, **H. Srikanth**, and **S. Witanachchi**, "Role of Epitaxy in Controlling the Magnetic and Magnetostrictive Properties of Cobalt Ferrite-PZT Bilayers", *Journal of Physics D: Applied Physics* 43, 485001 (2010)

74. *D. Mukherjee*, **T. Dhakal**, **H. Srikanth**, **P. Mukherjee**, and **S. Witanachchi**, "Evidence of Carrier-Mediated Magnetism in Mn-Doped ZnO Thin Films", *Physical Review B* 81, 205202 (2010)

75. **T. Dhakal**, *D. Mukherjee*, *R. Hyde*, **P. Mukherjee**, **M. H. Phan**, **H. Srikanth**, and **S. Witanachchi**, "Magnetic anisotropy and field-switching in cobalt ferrite thin films deposited by pulsed laser ablation", *Journal of Applied Physics* 107, 053914 (2010)

76. *H. Verma*, *D. Mukherjee*, **S. Witanachchi**, **P. Mukherjee**, and **M. Batzill**, "Comparative Study of ZnO Thin Film and Nano-Pillar Growth on YSZ(111) and Sapphire (0001) Substrates by Pulsed Laser Deposition", *Journal of Crystal Growth* 312, 2012 (2010)

77. Khadka, Dhan B.; **Haynie, Donald T**., "Insoluble Synthetic Polypeptide Mats from Aqueous Solution by Electrospinning", ACS APPLIED MATERIALS & INTERFACES Volume: 2   Issue: 10   Pages: 2728-2732 (2010)

78. **A. Datta,** *J. Paul*, A. Kar, A. Patra, Z. Sun, L. Chen, J. Martin and **G.S. Nolas**, 'Facile chemical synthesis of nanocrystalline thermoelectric alloys based on Bi-Sb-Te-Se', Crystal Growth and Design. 10, 3983 (2010)

79. **S. Pal**, *S. Chandra,* **M. H. Phan**, **P. Mukherjee** and **H. Srikanth**, "Carbon Nanostraws: Nanotubes filled with superparamagnetic particles", *Nanotechnology 20*, 485604 (2009)

80. V. Alexandrakis, G. Basina, D. Niarchos, G. Hadjipanayis, **S. Pal**, **H. Srikanth**, I. Panagiotopoulos, V. Tzitzios, "Chemical synthesis and magnetic properties of cubic CoO nanocrystals and 3D nanostructures", *Crystal Growth and Design 9*, 3353 (2009)

81. **M. H. Phan**, *M. B. Morales*, C. N. Chinnasamy, V. G. Harris and **H. Srikanth,** "Magnetism and magnetocaloric effect in gadolinium-iron garnet nanostructures", *Journal of Physics D: Applied Physics 42*, 115007 (2009)

82. **S. Pal,** *M. B. Morales*, **P. Mukherjee, H. Srikanth**, "Synthesis and magnetic properties of gold-coated iron oxide nanoparticles", *Journal of Applied Physics 105*, 07B504 (2009)

83. *M. B. Morales,* **M. H. Phan**, *S. Pal*, *N. A. Frey* and **H. Srikanth**, "Particle blocking and carrier fluid freezing effects on magnetic properties of Fe_3O_4-based ferrofluids", *Journal*

of Applied Physics 105, 07B511 (2009)

84. *N. A. Frey, M. H. Phan*, **H. Srikanth**, *S. Srinath*, C. Wang, S. Sun, "Inter-particle interactions in coupled $Au-Fe_3O_4$ nanoparticles", ***Journal of Applied Physics 105***, 07B502 (2009)

85. *D. Mukherjee*, *R. Hyde*, **T. Dhakal**, **H. Srikanth**, **P. Mukherjee**, and **S. Witanachchi**. "Investigation of the Pb Depletion in Single and Dual Pulsed Laser Deposited Epitaxial PZT Thin Films and Their Structural Characterization", in *Multiferroic and Ferroelectric Materials* (A. Gruverman, C.J. Fennie, I. Kunishima, B. Noheda, T.W. Noh, eds.) ***Materials Research Society Symposium Proceedings****, 1199, 1199-F03-37 (2009)*

86. **T. Dhakal**, *D. Mukherjee*, *R. Hyde*, **H. Srikanth**, **P. Mukherjee**, and **S. Witanachchi** "Enhancement in Ferroelectricity in V-Doped ZnO Thin Film Grown Using Laser Ablation", in *Multiferroic and Ferroelectric Materials* (A. Gruverman, C.J. Fennie, I. Kunishima, B. Noheda, T.W. Noh, eds.) ***Materials Research Society Symposium Proceedings****, 1199, 1199-F03-44 (2009)

87. *D. Mukherjee*, **T. Dhakal**, **H. Srikanth**, **P. Mukherjee**, and **S. Witanachchi**, "Growth of Epitaxial ZnO:Mn/ZnO:V Heterostructures and Ferroelectric-Ferromagnetic Characterization", ***Materials Research Society Symposium Proceedings***, 1161, 1161-I02-02, 2009

88. *H. Kirby,* J. Martin*, **A. Datta***, L. Chen, **G.S. Nolas**, "Enhanced thermoelectric properties in PbTe nanocomposites", ***Materials Research Society Symposium Proceedings***, 1166, 1166-NO3-27 (2009)

89. P. Poddar, *M. B. Morales*, *N. A. Frey*, S. A. Morrison, E. E. Carpenter and **H. Srikanth**, "Transverse susceptibility study of the effect of varying dipolar interactions on anisotropy peaks in a 3D assembly of soft ferrite nanoparticles", **Journal of Applied Physics 104**, 063901 (2008)

90. S. Srinath, P. Poddar, D. S. Sidhaye, B. L. V. Prasad, *J. Gass* and **H. Srikanth**, "Static and dynamic magnetic properties of Co nanoparticles", **Journal of Nanoscience and Nanotechnology 8**, 4086 (2008)

91. **G.S. Nolas**, *M. Beekman*, *J. Martin*, D. Wang and **X.S. Lin**, "Bulk materials research for thermoelectric power generation applications", ***Materials Research Society Symposium Proceedings***, Vol. 1044, 1044-U05-01 (2007)

92. *J. Martin*, *S. Stefanoski*, L. Wang, L. Chen and **G.S. Nolas**, "Synthesis and thermoelectric properties of lead chalcogenide nanocomposites", ***Materials Research Society Symposium Proceedings***, Vol. 1044, 1044-U01-05 (2007)

Journal Publications (under review):

93. "Enhanced magnetic hyperthermia and biodetection of functional manganese ferrite/graphene oxide nanocomposites," - A.T. Le, C.D. Giang, V.N. Phan, **J. Alonso**, *J. Devkota*, **H. Srikanth**, and **M.H. Phan** *Nanotechnology* 2015 (under review)

94. "Anisotropic mechanical, magnetic, and giant magneto-impedance properties of Co-rich amorphous ribbons," - H.T. Tran, *J. Devkota*, *T. Eggers*, *J. Wingo*, W. Cai, I. Skorvanek, **H. Srikanth**, **M.H. Phan**, *Journal of Electronic Materials* 2015 (under review)

95. "Iron Oxide Nano-Octopods with Tunable Sizes for Enhanced Hyperthermia," *Z. Nemati*, **J. Alonso**, L. M. Martinez, **H. Khurshid**, E. Garaio, J.A. Garcia, **M.H. Phan**, and **H. Srikanth**, *Nanoscale* 2015 (under review)

96. "Tunable High Aspect Ratio Iron Oxide Nanorods for Enhanced Hyperthermia," **R. Das**, **J. Alonso**, *Z.N. Porshokouh, V. Kalappattil, D. Torres*, **M.H. Phan**, Eneko Garayo, José Ángel García, J.Luis Sanchez Llamazares, and **H. Srikanth**, *Advanced Functional Materials* 2015 (under review)

Conference Presentations (contributed):

1. "Magneto-impedance based detection of magnetically labeled cancer cells and bio-proteins," *J. Devkota*, M. Howell, S. Mohapatra, T.H. Nhung, **P. Mukherjee**, **H. Srikanth**, and **M.H. Phan** (oral), APS March meeting, March 1-6, San Antonio, TX (2015).

2. "Effect of annealing on the surface magnetic and magneto-impedance properties of Co-based amorphous microwires," *V. Kalappattil*, *J. Devkota*, *E. Clements*, **S. Chandra**, J.S. Liu, H.X. Shen, J.F. Sun, **H. Srikanth**, and **M.H. Phan** (oral), APS March meeting, March 1-6, San Antonio, TX (2015).

3. "Magnetic Interaction Study on Multi-Walled Carbon Nanotubes filled with Core/Shell Iron/Iron Oxide Nanoparticles," *K. Stojak Repa*, *D. Israel*, **H. Khurshid**, **J. Alonso**, **M.H. Phan**, **H. Srikanth** (oral), APS March meeting, March 1-6, San Antonio, TX (2015).

4. "Iron oxide nanoparticles with controlled morphology for advanced hyperthermia," *Z. Nemati Porshokouh*, **H. Khurshid**, **J. Alonso Messa**, **M.H. Phan**, **H. Srikanth** (oral), APS March meeting, March 1-6, San Antonio, TX (2015).

5. "Magneto-reactance based detection of MnO nanoparticle-embedded Lewis lung carcinoma cancer cells," (poster) *J. Devkota*, M. Howell, S. Mohapatra, **P. Mukherjee**, **H. Srikanth**, and **M.H. Phan**, 59th annual conference on Magnetism and Magnetic Materials (MMM), Honolulu, Hawaii, (Nov. 3-7, 2014).

6. "Manipulating specific absorption rate of iron oxide nanoparticles by modifying shape anisotropy," (oral) **H. Khurshid**, **J. Alonso**, *Z. Nemati*, **M.H. Phan**, **P. Mukherjee**, M. L. Fdez-Gubieda, J. M. Barandiarán, and **H. Srikanth,** 59th annual conference on Magnetism and Magnetic Materials (MMM), Honolulu, Hawaii, (Nov. 3-7, 2014).

7. "FeCo nanowires for enhanced magnetic hyperthermia," (poster) **J. Alonso**, **H. Khurshid**, *V. Sankar*, *Z. Nemati*, **M.H. Phan**, E. Garayo, J.A. García, and **H. Srikanth,**

59th annual conference on Magnetism and Magnetic Materials (MMM), Honolulu, Hawaii, (Nov. 3-7, 2014).

8. "Superparamagnetic properties of carbon nanotubes filled with $NiFe_2O_4$ nanoparticles," (poster) *K. Stojak Repa*, *D. Israel*, ***J. Alonso***, **M.H. Phan**, E.M. Palmero, M. Vazquez, and **H. Srikanth,** 59th annual conference on Magnetism and Magnetic Materials (MMM), Honolulu, Hawaii, (Nov. 3-7, 2014).

9. "From core-shell to hollow $Fe/\gamma-Fe_2O_3$ nanoparticles: evolution of the magnetic behavior" – *Z. Nemati*, ***H. Khurshid***, ***J. Alonso***, **M.H. Phan**, and **H. Srikanth,** 59th annual conference on Magnetism and Magnetic Materials (MMM), Honolulu, Hawaii, (Nov. 3-7, 2014).

10. "Magnetic characteristics of Strain Modified $CoFe_2O_4$ Thin Films in $La_{0.7}Sr_{0.3}MnO_3/BaTiO_3/CoFe_2O_4$ Multiferroic Heterostructures", *M. Hordagoda*, **D. Mukherjee**, **M. H. Phan**, **H. Srikanth**, **S. Witanachchi**, and **P. Mukherjee**, Materials Research Society, 2014 MRS Spring Meeting & Exhibit, San Francisco, CA (April 21st - 25th, 2014).

11. "The Effect of Very Low Doping Concentrations of La in La Doped PZT Thin Films", *M. Hordagoda*, **D. Mukherjee**, **P. Mukherjee**, and **S. Witanachchi**, Materials Research Society, 2014 MRS Spring Meeting & Exhibit, San Francisco, CA (April 21st - 25th, 2014).

12. "Enhanced surface-quality, magnetic and ferroelectric properties in epitaxial PZT/LSMO multiferroic heterostructures grown using dual-laser ablation", **D. Mukherjee**, *M. Hordagoda*, **H. Srikanth**, **S. Witanachchi**, and **P. Mukherjee**, American Ceramic Society, 38th International Conference and Exposition on Advanced Ceramics and Composites, Daytona Beach, FL (Jan. 26th-31st, 2014) (invited).

13. "Physical/Chemical Combinatorial Strategy Towards Multi-dimensional Perovskite Nano- and Micro-structures with Enhanced Functionality", A. Datta, **D. Mukherjee**, **S. Witanachchi**, and **P. Mukherjee**, American Ceramic Society, 38th International Conference and Exposition on Advanced Ceramics and Composites, Daytona Beach, FL (Jan. 26th-31st, 2014) (invited).

14. "Role of dilute La-doping in enhancing the polarization in epitaxial $Pb1-xLaxZr_{0.52}Ti_{0.48}O_3$ thin films", *M. Hordagoda*, **D. Mukherjee**, D. Ghosh, J. L. Jones, **S. Witanachchi**, and **P. Mukherjee**, American Ceramic Society, 38th International Conference and Exposition on Advanced Ceramics and Composites, Daytona Beach, FL (Jan. 26th-31st, 2014).

15. "Magnetic and ferroelectric property enhancement of PZT/LSMO multiferroic thin films using dual laser ablation", *M. Hordagoda*, **D. Mukherjee**, R.Hyde, **P. Mukherjee**, and **S. Witanachchi**, American Ceramic Society, Electronic Materials and Applications 2014, Orlando, FL (Jan. 22nd-24th, 2014).

16. "The effect of La doping on the ferroelectric and magnetic properties of PZT/LSMO multiferroic heterostructures", *M. Hordagoda*, **D. Mukherjee**, D. Ghosh, J. L. Jones, **P. Mukherjee**, and **S. Witanachchi**, American Ceramic Society, Electronic Materials and Applications 2014, Orlando, FL (Jan. 22nd-24th, 2014).

17. "Enhanced ferroelectric properties in epitaxial La-doped PZT films at low concentrations of La-doping", *M. Hordagoda*, **D. Mukherjee**, D. Ghosh, J. L. Jones, **P. Mukherjee**, and **S. Witanachchi**, American Ceramic Society, Electronic Materials and Applications 2014, Orlando, FL (Jan. 22nd-24th, 2014).

18. "Controlled seed-layer assisted growth of hierarchically-ordered $PbZr_{0.52}Ti_{0.48}O_3$ nanostructure arrays with improved ferroelectric properties", A. Datta, **D. Mukherjee**, **S. Witanachchi**, and **P. Mukherjee**, American Ceramic Society, 38th International Conference and Exposition on Advanced Ceramics and Composites, Daytona Beach, FL (Jan. 26th-31st, 2014).

19. **D. Mukherjee**, *M. Hordagoda*, **M. H. Phan**, **H. Srikanth**, **S. Witanachchi**, and **P. Mukherjee**, "Enhanced magnetism and ferroelectricity in high-quality epitaxial $PbZr_{0.52}Ti_{0.48}O_3/CoFe_2O_4/La_{0.7}Sr_{0.3}MnO_3$ multiferroic heterostructures grown using the dual-laser ablation technique" Magnetism and Magnetic Materials, 58th Annual Conference on MMM, Denver, CO (Nov. 4th - 8th, 2013)

20. **D. Mukherjee**, *M. Hordagoda*, **M. H. Phan**, **H. Srikanth**, **S. Witanachchi**, and **P. Mukherjee**, " Strain modification of magnetization using the structural transitions of the ferroelectric $BaTiO_3$ sandwich-layer in high-quality epitaxial $CoFe_2O_4/BaTiO_3/La_{0.7}Sr_{0.3}MnO_3$ multiferroic heterostructures grown using the dual-laser ablation technique", Magnetism and Magnetic Materials, 58th Annual Conference on MMM, Denver, CO (Nov. 4th - 8th, 2013)

21. **H. Khurshid**; *S. Chandra*; **M.H. Phan**; **P. Mukherjee**; **H. Srikanth**, "Static and dynamic magnetic properties of hollow spherical γFe_2O_3 nanoparticles", The 58th Annual Magnetism and Magnetic Materials (MMM) Conference, November 4-8, 2013, Denver, Colorado, USA

22. **H. Khurshid**; **M.H. Phan**; **P. Mukherjee**; **H. Srikanth**, "Tuning Exchange Bias in Core/Shell $Fe/\gamma Fe_2O_3$ Nanoparticles: Role of Frozen Interfacial and Surface Spins", The 58th Annual Magnetism and Magnetic Materials (MMM) Conference, November 4-8, 2013, Denver, Colorado, USA

23. *S. Chandra*, A. Biswas; **M.H. Phan**; **H. Srikanth**, "Magnetic properties of polycrystalline and nanocrystalline NdMnO3", The 58th Annual Magnetism and Magnetic Materials (MMM) Conference, November 4-8, 2013, Denver, Colorado, USA

24. *J. Devkota*; *K. Stojak*; J. Wingo; T.T. Mai T; P.T. Ha; H.N. Pham; X.P. Nguyen; **P. Mukherjee**; **H. Srikanth**; **M.H. Phan**, "Synthesis, inductive heating, and magnetoimpedance-based detection of multifunctional Fe_3O_4 nanoconjugates", The 58th Annual Magnetism and Magnetic Materials (MMM) Conference, November 4-8, 2013, Denver, Colorado, USA

25. *S. Chandra*; A. Biswas; **H. Khurshid**; W. Li; G.C. Hadjipanayis; **H. Srikanth**, "Spin freezing and inverse magnetocaloric effect in core/shell and hollow nanostructures", The

58th Annual Magnetism and Magnetic Materials (MMM) Conference, November 4-8, 2013, Denver, Colorado, USA

26. *J. Devkota*; P. Colosimo; J. Wingo; A. Chen; **H. Srikanth**; **M.H. Phan**, "Tailoring magnetic and microwave absorption properties of glass-coated soft ferromagnetic microwires for microwave energy sensing applications", The 58th Annual Magnetism and Magnetic Materials (MMM) Conference, November 4-8, 2013, Denver, Colorado, USA

27. *A. Ruiz,* **D. Mukherjee,** *J. Devkota, M. Hordagoda,* **S. Witanachchi, P. Mukherjee, H. Srikanth, M.H. Phan, "**Enhanced GMI effect in soft ferromagnetic amorphous ribbons with pulsed laser deposition of cobalt ferrite,**"** 12th Joint MMM/Intermag Conference, Jan 14 – 18, 2013, Chicago, IL, USA

28. *J. Devkota, A. Ruiz,* **P. Mukherjee, H. Srikanth, M.H. Phan,** W. Wang, S. Mohapatra, "Magneto-impedance biosensor with enhanced sensitivity for highly sensitive detection of superparamagnetic nanoparticles," 12th Joint MMM/Intermag Conference, Jan 14 – 18, 2013, Chicago, IL, USA

29. *P. Lampen*, **H. Khurshid**, *S. Chandra*, **M.H. Phan**, **H. Srikanth**, J. Borchers, K. Krycka, B. Kirby, M.Wasbrough, S.Watson and W. Chen, "Surface pinning and exchange bias phenomena in core/shell structured Fe/γ-Fe$_2$O$_3$ nanoparticles", 12th Joint MMM/Intermag Conference, Jan 14 – 18, 2013, Chicago, IL, USA

30. *S. Chandra*, **H. Khurshid**, **M.H. Phan**, and **H. Srikanth**, "Asymmetric hysteresis and its dependence on magnetic anisotropy in exchange biased Co/CoO core-shell nanoparticles", 12th Joint MMM/Intermag Conference, Jan 14 – 18, 2013, Chicago, IL, USA

31. *H. Khurshid*, W. Li, *S. Chandra*, **M.H. Phan**, G. Hadjipanayis, **P. Mukherjee**, and **H. Srikanth**, "Shape controlled synthesis and magnetic properties of core/shell structured FeO/Fe$_3$O$_4$ nanoparticles", 12th Joint MMM/Intermag Conference, Jan 14 – 18, 2013, Chicago, IL, USA

32. *K. Stojak, S. Chandra,* **H. Khurshid**, **M.H. Phan**, **H. Srikanth,** "Enhanced Magnetic Properties in Nanoparticle-Filled CNTs," American Physical Society March Meeting 2013, March 18-22, 2013, Baltimore, MD, USA

33. *J. Devkota, A. Ruiz,* **P. Mukherjee**, **H. Srikanth**. **M.H. Phan**, *W. Wang,* and *S. Mohapatra,* "Detection of low-concentration superparamagnetic nanoparticles using a functional biosensor based on magneto-impedance technology," APS March Meeting, March 18 – 22, 2013, Baltimore, MD, USA

34. **M.H. Phan**, *J. Devkota*, **H. Srikanth**, P. Colostro, and A. Chen, "Sensing RF and microwave energy with fiber Bragg grating heating via soft ferromagnetic glass-coated microwires," APS March Meeting, March 18 – 22, 2013, Baltimore, MD, USA

35. *A. Ruiz, J. Devkota*, **P. Mukherjee, H. Srikanth**, and **M.H. Phan**, "Giant magnetoimpedance effect of Co-based magnetic ribbon as a chemical sensing probe," APS March Meeting, March 18 – 22, 2013, Baltimore, MD, USA

36. *M. Hordagoda*, **D. Mukherjee**, **R. Hyde**, D. Ghosh, J. L. Jones, **P. Mukherjee**, and **S. Witanachchi**, "Ferroelectric proerties of La doped PZT thin films deposited using dual laser ablation", *American Chemical Society (Florida Section)*, *2013 Florida Annual Meeting and Exposition (FAME)*, Tampa, FL (May 10th, 2013)

37. **A. Datta**, **D. Mukherjee**, **S. Witanachchi** and **P. Mukherjee**, "Growth of low-dimensional $Pb(Zr_xTi_{1-x})O_3$ nanostructures by combined physical and wet-chemical synthesis approaches with enhanced electronic properties", *Materials Research Society, 2013 MRS Spring Meeting & Exhibit*, San Francisco, CA (April 1st - 5th, 2013)

38. **D. Mukherjee**, *M. Hordagoda*, *N. Bingham*, **H. Srikanth**, **S. Witanachchi**, and **P. Mukherjee**, "Challenges and solutions to the stoichiometric growth of high quality epitaxial $PbZr_{0.52}Ti_{0.48}O_3/La_{0.7}Sr_{0.3}MnO_3$ multiferroic heterostructures using single and dual laser ablation processes", *Materials Research Society, 2013 MRS Spring Meeting & Exhibit*, San Francisco, CA (April 1st - 5th, 2013)

39. **D. Mukherjee**, **R. Hyde**, *M. Hordagoda*, *N. Bingham*, **M. H. Phan**, **H. Srikanth**, **S. Witanachchi**, and **P. Mukherjee**, "Growth and characterization of high quality epitaxial $La_{0.7}Sr_{0.3}MnO_3$ thin films using dual-laser ablation technique", *Magnetism and Magnetic Materials, 12th Joint MMM/INTERMAG Conference*, Chicago, IL (Jan. 14th - 18th, 2013)

40. *M. Hordagoda*, **D. Mukherjee**, *N. Bingham*, D. Ghosh, J. L. Jones, **H. Srikanth**, **P. Mukherjee**, and **S. Witanachchi**, "Effect of La doping in PZT on the magnetic and ferroelectric properties of epitaxial PZT/LSMO multiferroic heterostructures", *Magnetism and Magnetic Materials, 12th Joint MMM/INTERMAG Conference*, Chicago, IL (Jan. 14th - 18th, 2013)

41. **D. Mukherjee**, **R. Hyde**, *M. Hordagoda*, *N. Bingham*, **H. Srikanth**, **P. Mukherjee**, and **S. Witanachchi**, "Magnetic properties of preferentially-oriented nanostructured cobalt ferrite thin films grown using oblique-angle pulsed laser deposition", *Magnetism and Magnetic Materials, 12th Joint MMM/INTERMAG Conference*, Chicago, IL (Jan. 14th - 18th, 2013)

42. **D. Mukherjee**, *M. Hordagoda*, **R. Hyde**, *D. S. Hromalik*, *N. Bingham*, **H. Srikanth**, **S. Witanachchi**, and **P. Mukherjee**, "Magnetic polaron percolation in epitaxial Mn doped ZnO thin films grown at higher doping concentrations using dual-laser ablation technique", *Magnetism and Magnetic Materials, 12th Joint MMM/INTERMAG Conference*, Chicago, IL (Jan. 14th - 18th, 2013)

43. *A. Ruiz*, **D. Mukherjee**, *J. Devkota*, *M. Hordagoda*, **P. Mukherjee**, **S. Witanachchi**, **H. Srikanth**, **M. H. Phan**, "Enhanced GMI effect in soft ferromagnetic amorphous ribbons with pulsed laser deposition of cobalt ferrite", *Magnetism and Magnetic Materials, 12th Joint MMM/INTERMAG Conference*, Chicago, IL (Jan. 14th - 18th, 2013)

44. *A. Ruiz,* **D. Mukherjee,** *J. Devkota, M. Hordagoda,* **S. Witanachchi, P. Mukherjee, H. Srikanth, M.H. Phan, "**Enhanced GMI effect in soft ferromagnetic amorphous ribbons with pulsed laser deposition of cobalt ferrite,**"** 12th Joint MMM/Intermag Conference, Jan 14 – 18, 2013, Chicago, IL, USA

45. *J. Devkota, A. Ruiz,* **P. Mukherjee, H. Srikanth, M.H. Phan,** W. Wang, S. Mohapatra, "Magneto-impedance biosensor with enhanced sensitivity for highly sensitive detection of superparamagnetic nanoparticles," 12th Joint MMM/Intermag Conference, Jan 14 – 18, 2013, Chicago, IL, USA

46. *P. Lampen*, **H. Khurshid**, *S. Chandra*, **M.H. Phan**, **H. Srikanth**, J. Borchers, K. Krycka, B. Kirby, M.Wasbrough, S.Watson and W. Chen, "Surface pinning and exchange bias phenomena in core/shell structured Fe/γ-Fe$_2$O$_3$ nanoparticles", 12th Joint MMM/Intermag Conference, Jan 14 – 18, 2013, Chicago, IL, USA

47. *S. Chandra*, **H. Khurshid**, **M.H. Phan**, and **H. Srikanth**, "Asymmetric hysteresis and its dependence on magnetic anisotropy in exchange biased Co/CoO core-shell nanoparticles", 12th Joint MMM/Intermag Conference, Jan 14 – 18, 2013, Chicago, IL, USA

48. *H. Khurshid*, W. Li, *S. Chandra*, **M.H. Phan**, G. Hadjipanayis, **P. Mukherjee**, and **H. Srikanth**, "Shape controlled synthesis and magnetic properties of core/shell structured FeO/Fe$_3$O$_4$ nanoparticles", 12th Joint MMM/Intermag Conference, Jan 14 – 18, 2013, Chicago, IL, USA

49. *S. Chandra*, **H. Khurshid**, W. Li, G.C. Hadjipanayis, **M.H. Phan**, and **H. Srikanth**, "Spin dynamics and criteria for onset of exchange bias in superspin glass Fe/γ-Fe$_2$O$_3$ core-shell nanoparticles", 12th Joint MMM/Intermag Conference, Jan 14 – 18, 2013, Chicago, IL, USA

50. "Recent Advances and Future Research Directions in Giant Magneto-impedance Materials" Invited Talk by **M.H. Phan**, in the Special Session: "Tunable metamaterials,

Giant Magnetoimpedance and GMI-related Applications" at Advanced Electromagnetics Symposium, April 16-19, 2012, Paris, France

51. *M. Hordagoda*, **D. Mukherjee**, D. Ghosh, J. L. Jones, **P. Mukherjee**, **S. Witanachchi**, "Growth and characterization of La doped lead zirconium titanate epitaxial thin films", Materials Research Society, 2012 MRS Fall Meeting & Exhibit, Boston, MA (Nov. 25th - 30th, 2012)

52. **D. Mukherjee**, *M. Hordagoda*, **R. H. Hyde**, *N. Bingham*, **H. Srikanth**, **P. Mukherjee**, and **S. Witanachchi**, "Epitaxial Growth of Multiferroic Heterostructures of Magnetic and Ferroelectric Oxides using the Dual-laser Ablation Technique", American Vacuum Society, 59th International AVS Symposium and Exhibition, Tampa, Fl (Oct. 28th - Nov. 2nd, 2012)

53. **D. Mukherjee**, *M. Hordagoda*, **R. H. Hyde**, *N. Bingham*, **H. Srikanth**, **P. Mukherjee**, and **S. Witanachchi**, "Role of Dual-laser Ablation in Controlling Mn Oxide Precipitation during the Epitaxial Growth of Mn Doped ZnO Thin Films with Higher Doping Concentrations", American Vacuum Society, 59th International AVS Symposium and Exhibition, Tampa, Fl (Oct. 28th - Nov. 2nd, 2012)

54. *C. Hettiarachchi*, *D. M. Feliciano*, **D. Mukherjee**, **P. Mukherjee**, and **S. Witanachchi**, "Improvement of Carrier Transport in PbSe Quantum Dot-Embedded Polymeric Solar Cells Fabricated by a Laser Assisted Spray Process", American Vacuum Society, 59th International AVS Symposium and Exhibition, Tampa, Fl (Oct. 28th - Nov. 2nd, 2012)

55. **D. Mukherjee**, **S. Witanachchi**, **R. Hyde**, and **P. Mukherjee**, "Advantages of Dual-laser Ablation in the Growth of Multicomponent Thin Films", 2012 HPLA International High-Power Laser Ablation Conference, Santa Fe, NM (April 30th - May 3rd, 2012)

56. **D. Mukherjee**, *M. Hordagoda*, **R. Hyde**, **P. Mukherjee**, **H. Srikanth**, and **S. Witanachchi**, "Dual Laser Ablation: A Novel Technique for the In-situ Growth of Epitaxial Multiferroic Heterostructures of Ultra-thin Films", NANOSMAT-USA-2012 Conference, Tampa, FL (March 27th - 30th, 2012)

57. *C.L. Hettiarachchi*, *D. Ferizovic*, **D. Mukherjee**, **R. Hyde**, **S. Witanachchi**, and **P. Mukherjee**, "Structural and Optical Properties of Surfactant-free Coatings of PbSe Quantum Dots deposited by a Laser Assisted Spray Process", NANOSMAT-USA-2012, Tampa, FL, (March 27th - 30th, 2012)

58. *M. Hordagoda*, **D. Mukherjee**, **R. Hyde**, **P. Mukherjee**, and **S. Witanachchi**, "Growth and Characterization of Epitaxial Pb(Zr0.52Ti0.48)O3 Ultra-thin Films using a Novel Dual Laser Deposition Technique", NANOSMAT-USA-2012, Tampa, FL, (March 27th - 30th, 2012)

59. **A. Datta**, *M. Hordagoda*, **D. Mukherjee**, **S. Witanachchi**, and **P. Mukherjee**, "Growth of one-dimensional Pb(ZrxTi1-x)O3 nanostructures by combined physical and wet-chemical synthesis approaches for enhanced ferroelectric properties", NANOSMAT-USA-2012, Tampa, FL, (March 27th - 30th, 2012)

60. *J. Devkota*, *A. Ruiz*, **H. Khurshid,** *A. Chaturvedi, A. Puri,* **P. Mukherjee, H. Srikanth**, **M.H. Phan**, "Detection of Functional Magnetic Nanoparticles using Ferromagnetic Microwires-based Giant Magneto-impedance Sensors", Nano-Bio Collaborative International Conference, March 22-24, 2012, Tampa, Florida, USA

61. *A. Ruiz, J. Devkota, A. Chaturvedi, K. Stojak,* **P. Mukherjee, H. Srikanth**, **M.H. Phan**, "GMI sensors with superparamagnetic nanoparticles for highly sensitive detection of cancer cells and biomolecules", Nano-Bio Collaborative International Conference, March 22-24, 2012, Tampa, Florida, USA

62. *K. Stojak,* **P. Mukherjee, H. Srikanth**, **M.H. Phan**, "Synthesis of carbon nanotubes filled with magnetic nanoparticles for biomedical applications", Nano-Bio Collaborative International Conference, March 22-24, 2012, Tampa, Florida, USA

63. *K. Stojak, S. Chandra, A. Ruiz,* **M.H. Phan, P. Mukherjee,** and **H. Srikanth**, "Filled Carbon Nanotubes with Novel Magnetic Properties for Biomedical Applications", NanoFlorida Conference, September 28-29, 2012 Tampa, Florida, USA

64. *J. Devkota, A. Ruiz,* **P. Mukherjee, H. Srikanth**, **M.H. Phan**, C. Wang and S. Mohapatra, "Amorphous Ribbon-based Magnetic Biosensor with Enhanced Sensitivity for Highly Sensitive Detection of Nanomag-D Beads", NanoFlorida Conference, September 28-29, 2012 Tampa, Florida, USA

65. *A. Popescu,* **A. Datta, G.S. Nolas** and **L. Woods**, 'Tailoring Thermoelectric Properties of Bismuth: Theoretical Investigations', American Institute of Physics Conference Proceedings 1449, 9th European Conference on Thermoelectrics, pp. 45 – 48, 2012.

66. *A. Ruiz, J. Devkota,* **P. Mukherjee, H. Srikanth**, **M.H. Phan**, "Improving the magnetic response of giant magneto-impedance in single and multi-wire systems", NanoFlorida Conference, September 28-29, 2012 Tampa, Florida, USA

67. *A. Chaturvedi, N. Laurita, K. Stojak*, **M.H. Phan**, **P. Mukherjee**, and **H. Srikanth**, "Carbon nanotube-based gas sensors using the magnetoimpedance effect", 56th Annual MMM Conference on Magnetism and Magnetic Materials, October 30 to November 3, 2011, Scottsdale, Arizona, USA

68. *N. Laurita, A. Chaturvedi, P. Jayathilaka,* **M.H. Phan**, **H. Srikanth**, and **C. W. Miller**, "Impact of field-induced exchange anisotropy on the magnetoimpedance effect in

FeMn/Metglas ribbons bilayer structures", 56th Annual MMM Conference on Magnetism and Magnetic Materials, October 30 to November 3, 2011, Scottsdale, Arizona, USA

69. *K. Stojak,* **S. Pal, H. Srikanth**, *C.Morales,* J. Dewdney, J.Wang and T.Weller, "Magnetic Polymer Nanocomposites with Tunable Microwave and RF Properties", 56th Annual MMM Conference on Magnetism and Magnetic Materials, October 30 to November 3, 2011, Scottsdale, Arizona, USA

70. **D. Mukherjee**, *R. Hyde*, **M. H. Phan**, *N. Bingham*, **H. Srikanth**, **P. Mukherjee** and **S. Witanachchi**, "Enhanced ferroelectricity and ferromagnetism in epitaxial $PbZr_{0.52}Ti_{0.48}O_3/La_{0.7}Sr_{0.3}MnO_3$ thin films with a $CoFe_2O_4$ sandwich layer" *Materials Research Society, 2011 MRS Fall Meeting & Exhibit*, Boston, MA (Nov. 28th - Dec 2nd, 2011)

71. **D. Mukherjee**, *R. Hyde*, **M. H. Phan**, *N. Bingham*, **H. Srikanth**, **P. Mukherjee** and **S. Witanachchi**, "Hetero-epitaxial Growth of Ferromagnetic Mn doped ZnO Thin Films on Al_2O_3 (0001) Substrates with Higher Doping Concentrations using Dual-laser Deposition", *Materials Research Society, 2011 MRS Fall Meeting & Exhibit*, Boston, MA (Nov. 28th - Dec. 2nd, 2011)

72. **D. Mukherjee**, *R. Hyde*, **P. Mukherjee** and **S. Witanachchi**, "Dual-laser Ablation for the Growth of Epitaxial Pb(Zr0.52Ti0.48)O3 Ultrathin Films", *Materials Research Society, 2011 MRS Fall Meeting & Exhibit*, Boston, MA (Nov. 28th - Dec. 2nd, 2011)

73. **D. Mukherjee**, **R. Hyde**, *N. Bingham*, **M. H. Phan**, **H. Srikanth**, **P. Mukherjee** and **S. Witanachchi**, "Ziz-zag Interface and Strain-influenced Ferromagnetism in Epitaxial $Mn_3O_4/La_{0.7}Sr_{0.3}MnO_3$ Thin Films grown on MgO (100) and $SrTiO_3$ (100) substrates", *Magnetism and Magnetic Materials, 56th Annual MMM Conference*, Scottsdale, AZ (Oct. 30th – Nov. 3rd 2011)

74. **D. Mukherjee**, **P. Mukherjee**, **H. Srikanth**, and **S. Witanachchi**, "Carrier-mediated Interaction of Magnetic Moments in Oxygen Vacancy Controlled Epitaxial Mn doped ZnO Thin Films", *Magnetism and Magnetic Materials, 56th Annual MMM Conference*, Scottsdale, AZ (Oct. 30th – Nov. 3rd 2011)

75. **D. Mukherjee**, *R. Hyde*, *N. Bingham*, **M. H. Phan**, **H. Srikanth**, **P. Mukherjee**, and **S. Witanachchi**, "Interfacial magnetoelectric coupling in epitaxial LSMO and Mn doped PZT heterostructures", *Materials Research Society, 2011 MRS Spring Meeting & Exhibit*, San Francisco, CA (April 25th - 29th, 2011)

76. *L. Nicholas, A. Chaturvedi, K. Stojak, S. Chandra*, **M. H. Phan**, **H. Srikanth**, "Giant magnetoimpedance in magnetic nanoparticles patterned Co-based amorphous ribbons for biosensing applications", the APS March Meeting, March 21 - 25, 2011, Dallas, Texas

77. *A. Chaturvedi, T. Dhakal*, **S. Witanachchi**, **M.H. Phan**, **H. Srikanth**, and A.T. Le, "Correlation between magnetic softness, sample surface and magnetoimpedance in $Co_{69}Fe_{4.5}X_{1.5}Si_{10}B_{15}$ (X = Ni, Al, Cr) amorphous ribbons", the APS March Meeting, March 21 - 25, 2011, Dallas, Texas

78. "Synthesis and characterization of graphene patterned with Fe_3O_4 nanoparticles" - *S. Chandra, K. Stojak*, D. Ferizovic, M. Munoz, **M. H. Phan** and **H. Srikanth**, the APS March Meeting, March 21 - 25, 2011, Dallas, Texas

79. *N. Laurita, A. Chaturvedi*, A. Leary, P. Jayathilaka, C. Bauer, Casey W. Miller, **M.H. Phan**, M.E. McHenry, **H. Srikanth**, "Enhanced magnetoimpedance effect in $Co_{89}Zr_7B_4$ ribbon/$Fe_{80}Ni_{20}$ bilayer structures", the Symposium on Magnetic Materials for Energy Applications, February 27 to March 3, 2011, San Diego, California, USA

80. **D. Mukherjee**, **T. Dhakal**, **H. Srikanth**, **P. Mukherjee**, and **S. Witanachchi**, "Complementary Ferromagnetic Mechanisms in Mn doped ZnO Thin films deposited using Pulsed Laser Ablation", *American Physical Society, APS March Meeting 2011*, Dallas, TX (March 21st - 25th, 2011).

81. **D. Mukherjee**, **T. Dhakal**, *R. Hyde*, **P. Mukherjee**, **H. Srikanth**, and **S. Witanachchi**, "Effect of substrate induced strains on the magnetic and ferroelectric properties of epitaxial bilayer thin films of lead zirconate titanate and cobalt ferrite", *American Physical Society, APS March Meeting 2011*, Dallas, TX (March 21st - 25th, 2011).

82. J. Duscha, *R. Hyde*, **D. Mukherjee**, **S. Witanachchi**, "Growth and characterization of $Ba_8Ga_{16}Ge_{30}$ Type I clathrate thin films grown by pulsed laser deposition", *American Physical Society, APS March Meeting 2011*, Dallas, TX (March 21st - 25th, 2011).

83. **A. Datta**, *K. Wei, A. Popescu,* **L. Woods** and **G.S. Nolas**, 'Processing Dependence on the Thermoelectric Properties of Nanostructured Thermoelectric Materials', Materials Research Society Conference, November 29, Boston, Massachusetts, 2011.

84. **A. Datta**, 'Bottom-Up Strategy For Thermoelectric Nanocomposites', American Physical Society Annual Meeting, Dallas, Texas, March 22, 2011.

85. **George S. Nolas**, **Anuja Datta**, *Jagannath Paul*, Adrian Popescu, and Lilia Woods "Bottom-Up Approach for the Synthesis of Thermoelectric Materials with Nano-Scale Domains" 35th International Conference and Exposition on Advanced Cermics and Composites, Daytona Beach, Florida, January 27, 2011.

86. *A. Chaturvedi*, S. Stefanoski, **M. H. Phan**, **G. Nolas** and **H. Srikanth**, "Magnetocaloric effect and refrigeration capacity in $Eu_8Ga_{16}Ge_{30}$ – EuO composites", 54th annual Magnetism and Magnetic Materials (MMM) conference, Nov. 14-18, 2010, Atlanta GA

87. *S. Chandra*, A. Figueroa, **M. H. Phan**, **H. Srikanth**, B. Ghosh and A. K. Raychaudhuri, "Phase coexistence and magnetic anisotropy in polycrystalline and nanocrystalline LaMnO$_{3+d}$", 54th annual Magnetism and Magnetic Materials (MMM) conference, Nov. 14-18, 2010, Atlanta GA

88. *A. Chaturvedi*, A. Leary, *N. Laurita*, **M. H. Phan**, M. E. McHenry and **H. Srikanth**, "Giant magnetoimpedance and field sensitivity in amorphous and nanocomposite (Co$_{1-x}$Fe$_x$)$_{89}$Zr$_7$B$_4$ ribbons", 54th annual Magnetism and Magnetic Materials (MMM) conference, Nov. 14-18, 2010, Atlanta GA

89. *K. Stojak*, **S. Pal**, **H. Srikanth**, S. Skidmore, C. Morales, J. Dewdney, J. Wang and T. Weller, "Magnetic polymer composites with tunable microwave properties", APS March meeting, Portland OR (March 15 – 19, 2010)

90. *S. Chandra*, *N. A. Frey*, **M. H. Phan**, **H. Srikanth**, C. Wang and S. Sun, "Probing magnetic anisotropy and exchange bias in coupled Au-Fe$_3$O$_4$ nanoclusters", APS March meeting, Portland OR (March 15 – 19, 2010)

91. **S. Pal**, *K. Stojak, S. Chandra*, **M. H. Phan**, **P. Mukherjee** and **H. Srikanth**; "Fabrication and magnetic properties of CNT filled with Fe$_3$O$_4$ nanoparticles", APS March meeting, Portland OR (March 15 – 19, 2010)

92. **M. H. Phan**, *A. Chaturvedi*, S. Stefanoski, H. Kirby. **G. S. Nolas** and **H. Srikanth**; "Ferromagnetism and large MCE in EuGaGe clathrates", APS March meeting, Portland OR (March 15 – 19, 2010)

93. *D. Mukherjee*, *R. Hyde*, **T. Dhakal**, **H. Srikanth**, **P. Mukherjee**, and **S. Witanachchi**, "Dual-Laser Deposition of Stoichiometric PZT/CoFe$_2$O$_4$ Epitaxial Heterostructures", *Materials Research Society, 2010 MRS Spring Meeting & Exhibit*, San Francisco, CA (April 5th - 9th, 2010)

94. *A. Chaturvedi*, **M. H. Phan**, **H. Srikanth**, A. Leary and M. McHenry; "Optimization of GMI in amorphous CoFeZrB ribbons", APS March meeting, Portland OR (March 15 – 19, 2010)

95. *S. Pal, K. Stojak, S. Chandra*, **M. H. Phan**, **P. Mukherjee** and **H. Srikanth**, "High-aspect ratio magnetic nanotubes,"11th joint MMM-INTERMAG conference, Washington DC (Jan 18-22, 2010)

96. *D. Mukherjee*, *R. Hyde*, **T. Dhakal**, **S. Hariharan**, **P. Mukherjee**, and **S. Witanachchi**, "Enhanced Ferroelectric Properties in Highly Epitaxial and Fatigue-Resistant PZT Thin Films Deposited Using Dual-laser Ablation", *Materials Research Society*, *2010 MRS Fall Meeting & Exhibit*, Boston, MA (Nov. 29th - Dec. 3rd, 2010)

97. **A. Datta**, *J. Paul, A. Popescu*, **L. Woods, G.S. Nolas**, "Synthesis and Transport properties of Dimensional Nanocomposite Chalcogenides", *The American Physical Society Annual Meeting*, March 15-19, 2010, Portland, Oregon.

98. **A. Datta,** *J. Paul* and **G.S. Nolas**, "Solution Phase Synthesis Routes In Preparing Chalcogenide Nanocomposites With Enhanced Thermoelectric Properties", *The 86th American Chemical Society Florida Annual Meeting and Exposition*, May 13-15, 2010.

99. *H. Kirby, J. Martin,* L. Chen, **G.S. Nolas**, "Synthesis and Characterization of Doped and Undoped PbTe Nanocomposites", *The 86th American Chemical Society Florida Annual Meeting and Exposition*, May 13-15, 2010.

100. *D. Mukherjee*, *R. Hyde*, **T. Dhakal**, **S. Hariharan**, **P. Mukherjee**, and **S. Witanachchi**, "Investigation of the Pb Depletion in Single and Dual Pulsed Laser Deposited Epitaxial PZT Thin Films and Their Structural Characterization", *Materials Research Society, 2009 MRS Fall Meeting & Exhibit*, Boston, MA (Nov. 3rd - Dec. 4th, 2009)

101. **T. Dhakal**, *D. Mukherjee*, *R. Hyde*, **H. Srikanth**, **P. Mukherjee**, and **S. Witanachchi**, "Enhancement in Ferroelectricity in V-Doped ZnO Thin Film Grown Using Laser Ablation", *Materials Research Society, 2009 MRS Fall Meeting & Exhibit*, Boston, MA (Nov. 3rd - Dec. 4th, 2009)

102. *D. Mukherjee*, **T. Dhakal**, *R. Hyde*, **P. Mukherjee**, **S. Hariharan**, and **S. Witanachchi**, "Growth of Epitaxial ZnO:Mn/ZnO:V Heterostructures and Ferroelectric-Ferromagnetic Characterization", *Materials Research Society, 2009 MRS Spring Meeting & Exhibit*, San Francisco, CA (April 13th - 17th, 2009)

103. *M. Morales*, **M.H. Phan**, **S. Pal** and **H. Srikanth**, "Origin of glass-like relaxation in Fe_3O_4 ferrofluids", 2009 INTERMAG Conference, Sacramento CA (May 4-8, 2009)

104. **M. H. Phan**, *M. B. Morales*, C. N. Chinnasamy, B. Latha, V. G. Harris and **H. Srikanth**, "Magnetic frustration and particle size effects in nanostructured gadolinium iron garnets", 2009 INTERMAG Conference, Sacramento CA (May 4-8, 2009)

105. *M. B. Morales*, **M. H. Phan**, *N. A. Frey*, **S. Pal** and **H. Srikanth**, "Origin of magnetic anomalies and relaxation mechanisms in ferrofluids", APS March Meeting, Pittsburgh, PA (March 16-20, 2009)

106. **M. H. Phan**, *M. B. Morales*, **H. Srikanth**, C. N. Chinnasamy and V. G. Harris, "Competing effects of blocking and spin frustration in nanostructured gadolinium iron garnets", APS March Meeting, Pittsburgh, PA (March 16-20, 2009)

107. *K. Stojak*, **S. Pal**, M. J. Miner, **H. Srikanth**, S. Skidmore, J. Wang and T. Weller, "Functional nanocomposite polymer films with uniform nanoparticle dispersions", APS March Meeting, Pittsburgh, PA (March 16-20, 2009)

108. *A. Chaturvedi*, *S. Stefanoski*, **M. H. Phan**, G. T. Woods, **G. Nolas** and **H. Srikanth**, "Magnetic transitions and giant magnetocaloric effect in EuGaGe clathrates", 2009 APS March Meeting, Pittsburgh, PA (March 16-20, 2009)

109. *H. Kirby,* J. Martin*, **A. Datta***, L. Chen, **G.S. Nolas**, 'Enhanced thermoelectric properties in PbTe nanocomposites', *Mater. Rec. Soc.*, Boston, 2009.

110. Joshua Martin, **Anuja Datta**, Hillary Kirby, Adrian Popescu, Lilia Woods, Nathan Crane and **George S Nolas** "Enhanced Power Factor in Nanocomposite Chalcogenides". DOE Thermoelectric Applications Workshop, San Diego, October 1, 2009.

111. ***M. B. Morales***, *N. A. Frey*, **M. H. Phan** and **H. Srikanth**, "Magnetic properties of Fe_3O_4 and $CoFe_2O_4$ based ferrofluids"52nd annual Magnetism and Magnetic Materials (MMM) conference, Tampa, FL (November 7 – 11, 2008)

112. *M. B. Morales*, *N. A. Frey*, P. Poddar and **H. Srikanth**, "Transverse susceptibility probe of magnetic anisotropy and dipolar interactions in ferrite nanoparticles" 2008 APS March meeting (New Orleans, LA)

113. **H. Srikanth**, *M. B. Morales*, *N. A. Frey*, P. Poddar, **M. H. Phan**, "Radio frequency transverse susceptibility in magnetic nanoparticles", INTERMAG conference, May 4 – 8, 2008 (Madrid, Spain)

114. "Magnetism and magnetocaloric effect in ferrite and garnet nanoparticles" –**Invited talk by H. Srikanth** at the workshop on "Research trends in novel magnets for electromagnetic applications" –Santorini, Greece (Sep 2-5, 2008)

115. **M. H. Phan**, *M. B. Morales*, *N. A. Frey* and **H. Srikanth** , "Origin of magnetic anomalies in the liquid, frozen and mixed states of ferrofluids" the 53rd annual MMM conference, Nov. 2008 (Austin, TX)

116. **S. Pal**, *M. B. Morales*, **M. H. Phan**, **P. Mukherjee** and **H. Srikanth**, "Synthesis and magnetic properties of gold-coated core-shell $Au@Fe_3O_4$ nanoparticles", the 53rd annual MMM conference, Nov. 2008 (Austin, TX)

117. *N. A. Frey*, **M. H. Phan**, S. Srinath, C. Wang, S. Sun and **H. Srikanth**, "Anomalous magnetism and exchange bias in coupled $Au-Fe_3O_4$ nanoparticles", 2008 MRS Fall meeting, Dec. 1-5, 2008 (Boston, MA)

118. **M. H. Phan**, *M. B. Morales*, **S. Pal**, *N. A. Frey* and **H. Srikanth**, "Origin of magnetic anomalies in the liquid, frozen and mixed states of ferrofluids", 53rd annual MMM conference, Nov. 10-14, 2008 (Austin, TX)

119. **M.H. Phan**, *M. B. Morales*, **H. Srikanth**, C. N. Chinnasamy and V. G. Harris, "Magnetization dynamics and magnetocaloric effect in nanostructured $Gd_3Fe_5O_{12}$ garnets" , –53rd annual MMM conference, Nov. 10-14, 2008 (Austin, TX)

120. **S. Pal**, *M. B. Morales*, **M. H. Phan**, **P. Mukherjee** and **H. Srikanth**, "Synthesis and magnetic properties of gold-coated core-shell $Au@Fe_3O_4$ nanoparticles", 53rd annual MMM conference, Nov. 10-14, 2008 (Austin, TX)

121. M. J. Miner, **S. Pal**, *K. Stojak*, **H. Srikanth**, S. Skidmore, J. Wang and T. Weller, "Synthesis of surface functionalized magnetic nanoparticles and their polymer composites", 53rd annual MMM conference, Nov. 10-14, 2008 (Austin, TX).

122. *D. Mukherjee*, **T. Dhakal**, *R. Hyde*, **P. Mukherjee**, **S. Hariharan**, and **S. Witanachchi**, "Growth of Epitaxial CoFe2O4/PZT Heterostructures and Ferroelectric-Ferromagnetic Characterization", *Materials Research Society, 2008 MRS Fall Meeting*, Boston, MA (Dec. 1st - 5th, 2008).

123. *J. Martin*, L. Wang, L. Chen and **G.S. Nolas**, "Enhanced thermoelectric properties of PbTe nanocomposites", presented at the 27th International Thermoelectrics Conference, Corvallis, OR, August 7, 2008.

124. **G.S. Nolas**, *J. Martin*, S. Stefanoski, L. Wang and L. Chen, "Transport Properties of Lead Chalcogenide Nanocomposites", presented at the American Physical Society March Meeting, New Orleans, LA, March 13, 2008.

Invited presentations:
1. **M. H. Phan**, Invited Speaker, TMS Conference, Fifth Symposium on Magnetic Materials for Energy Applications, Orlando, FL (March 2015)

2. "Tunable Exchange Bias in Magnetic Nanostructures for Spintronics and Nanomedicine", Invited Talk (**M.H. Phan**), at The Magnetically Stimulated Soft Materials Conference, May 11- 12, 2015, Georgia, USA

3. **H. Srikanth**, Keynote Speaker, Workshop on nano and biomaterials, University of San Luis Potosi, San Luis Potosi, Mexico (December 2014)

4. "Functional nanoparticles for energy and nanomedicine applications" - Invited talk (**Hari Srikanth**), Nano and Giga challenges in Electronics, Photonics and Renewable Energy symposium 2014, Arizona State University, Phoenix, AZ (March 2014)

5. "Hybrid nanoparticles for hyperthermia and biosensing applications," – Invited talk (**Hari Srikanth**), Zing Bionanomaterials Conference, Nerja (Spain), April 2014

6. Seminar at Slovak Academy of Sciences "Functional Magnetic Nanostructures" - Invited talk (**Hari Srikanth**), Kosice, Slovak Republic (July 1, 2014)

7. "Magnetic nanostructures for microwave devices and biosensors," Invited talk (**Hari Srikanth**), European Magnetic Sensors and Actuators (EMSA) conference, Vienna, Austria (July 6-9, 2014)

8. "Advanced magnetoimpedance based biosensing using functionalized nanoparticles," Invited Talk (**M.H. Phan**) at the 59th Annual Magnetism and Magnetic Materials (MMM) Conference, November 3-7, 2014, Hawaii, USA

9. "Exchange bias and novel phenomena in hybrid nanostructures" –Invited talk (**Hari Srikanth**), Donostia International Conference on Nanoscaled Magnetism and Applications, San Sebastian (SPAIN), September 9-13, 2013

10. "Tunable exchange bias in core-shell and coupled nanoparticles" –Invited talk (**Hari Srikanth**), Magnetic Materials and Applications (MagMA-2013) conference, Guwahati (INDIA), December 5-7, 2013

11. "Magneto-impedance based detection of magnetic biomarkers: Opportunities and Challenges" Invited Talk (**M.H. Phan**) at the Energy Materials Nanotechnology (EMN) Fall Meeting, December 7 – 10, 2013 Orlando, Florida, USA

12. **M.H. Phan**, "Magneto-impedance based detection of magnetic biomarkers: Opportunities and Challenges" Invited Talk at the Energy Materials Nanotechnology (EMN) Fall Meeting, December 7 – 10, 2013 Orlando, Florida, USA

13. **G. S. Nolas**, "Structure-property Relationships in Skutterudites, Clathrates and Other Open-structured Materials", Plenary Presentation, 27th International Conference on Thermoelectrics, Corvallis, OR, August 4, 2007.

14. **G. S. Nolas**, "Enhanced Power Factor in Nanocomposite Chalcogenides", 2009 Department of Energy Thermoelectric Applications Workshop, October 1, 2009, San Diego, California.

15. **G. S. Nolas**, "Enhanced Power Factor in Nanocomposite Materials and Magnetocaloric Materials", Invited, 8th Pacific Rim Conference on Ceramic and Glass Technology (PacRim8), Vancouver, Canada, May 31 – June 5, 2009.

16. **G. S. Nolas**, "Thermoelectric Nanocomposite Chalcogenides", 451st WE-Heraeus-Seminar: Nanostructured Thermoelectric Materials, February 23, 2010, Bad Honnef, Germany.

17. **G.S. Nolas**, "Bottom-up Approach for Enhanced Thermoelectric Properties in Materials with Nano-scale Domains", Colloquium at the Department of Physics, Central Michigan University, September 2nd, 2010, Mount Pleasant, Michigan.

18. **G. S. Nolas**, "New Synthesis Techniques and Strategies for Materials Research towards Solid-state Power Conversion and Refrigeration Applications", Seminar for Inorganic Chemistry, Max-Planck Institute for Chemical Physics of Solids, Dresden, Germany, March 18, 2011.

19. **G.S. Nolas**, "A Bottom-up Approach for Nanostructured Thermoelectrics", Invited, 9th European Conference on Thermoelectrics, September 30, Thessaloniki, Greece, 2011.

20. **G.S. Nolas**, "New Crystal Growth Techniques in Investigating Single-crystal Inorganic Clathrates", Invited, to be presented at the Collaborative Conference on Crystal Growth, Orlando, Florida, December 11-14, 2012.

21. **G.S. Nolas**, 'Synthesis and Characterization of Nanostructured Thermoelectric Materials Prepared by a Two-step Bottom-up Synthetic Process', European Materials Research Society Conference, May 15, Strasbourg, France, 2012.

22. **H. Srikanth**, Invited speaker, Defense Sciences Research Council (DSRC –a division of DARPA) sponsored 'Advanced Materials for Enhanced Passive Components' Workshop, Oct. 30-31, 2008

23. **H. Srikanth**, Condensed Matter Seminar, Department of Physics, University of Delaware, Newark, DE (October 14, 2008)

24. **H. Srikanth**, Center for Integrated Electronics Seminar, Department of ECE, Rensselaer Polytechnic Institute, Troy, NY (October 1, 2008)

25. **H. Srikanth**, Invited Speaker, Novel Trends in Magnetic Materials for Electromagnetic Applications Workshop, Santorini, Greece (September 3 – 5, 2008)

26. **H. Srikanth**, Invited talk, "Surface and Interface magnetism in nanostructures and heterostructures", at the 2008 APS March meeting (New Orleans, LA)

27. **H. Srikanth**, Invited talk, "Interface magnetism in magnetic oxide nanostructures", at the 2008 MRS Spring meeting (San Francisco, CA)

28. **H.Srikanth**, Invited Speaker, International Conference on Materials for Advanced Technologies (ICMAT 2009), Singapore (June 2009)

29. **H. Srikanth**, Invited Speaker, US-Indo Technology Forum on "New Directions and Novel Applications in Magnetism", Mumbai, India (March 1 – 4, 2009)

30. **H. Srikanth**, Invited Speaker, "Functional magnetic nanostructures", Workshop on Magnetic Nanomaterials, S. N. Bose Center for Basic Sciences, Kolkata, India (January 26-28, 2009)

31. **H. Srikanth**, Condensed Matter Seminar, Department of Physics, University of Florida, Gainesville FL (November 16 2009)

32. **H. Srikanth**, Colloquium, Advanced Materials Research Institute, University of New Orleans, October 6, 2009

33. **H. Srikanth**, Invited Speaker, Conference on Strongly Correlated Materials (iConQuest 2010), New Delhi, INDIA (December 20-23, 2010)

34. **H. Srikanth**, Seminar, Northwestern University, Department of Physics, Evanston, IL (Oct. 14, 2010)

35. **H. Srikanth**, Invited Speaker, Symposium on Magnetic and Transport Properties of Oxides, CIMTEC 2010, Montecatini Terme, ITALY (June 6-11, 2010)

36. **H. Srikanth**, Seminar, "Functional magnetic nanostructures", CNR-ISMN, Bologna, ITALY (June 11, 2010)

37. **H. Srikanth**, Seminar, "Functional magnetic nanostructures", University of Uppsala, Uppsala, SWEDEN (June 4, 2010)

38. **H. Srikanth**, Seminar, "Functional magnetic nanostructures", KTH –Royal Institute of Technology, Stockholm, SWEDEN (June 3, 2010)

39. **H. Srikanth**, Seminar, "Functional magnetic nanostructures", IFW-Dresden, Dresden, GERMANY (May 31, 2010)

40. **H. Srikanth**, Invited Speaker, Focus Topic on "Bulk properties of oxides", APS March Meeting, Portland, OR (March 15-19, 2010); Title "Magnetism in complex oxides probed by transverse susceptibility and magnetocaloric effect"

41. **H. Srikanth**, Invited Speaker, "Magnetocaloric effect in oxide nanostructures" - H. Srikanth and M. H. Phan, the Symposium on Magnetic Materials for Energy Applications, February 27 to March 3, 2011, San Diego, California, USA (Invited Talk)

42. **H. Srikanth**, Invited Speaker, Multifunctional Materials-6 Workshop organized by DoD agencies, Kodiak, Alaska (July 31-Aug03, 2011)

43. **H. Srikanth**, Seminar on magnetic nanostructures, CSIC, University of Autonoma – Madrid, Spain (May 30, 2011)

44. **H. Srikanth**, Seminar, Cavendish Lab, Cambridge University, UK (June 6, 2011)

45. **H. Srikanth**, Seminar, Physics Department, Imperial College, London UK (June 7, 2011)

46. **H. Srikanth**, Invited Speaker, Soft Magnetic Materials (SMM 20) Conference, Kos

Island, Greece (September 2011)

47. **H. Srikanth**, Invited talk, "Tunable Microwave Properties in Magnetic Polymer Nanocomposites", 12th Joint MMM/Intermag Conference, Jan 14 – 18, 2013, Chicago, IL, USA

Patent-related activity:
1. **G.S. Nolas**, "Bulk Dimensional Nanocomposites for Thermoelectrics Applications", Patent Pending, US Provisional Patent Application # 12/104,016, filed April 2, 2009.

Other noteworthy professional activities by CIFM researchers:
- George Nolas was appointed Distinguished University Professor at USF and a Dresden Senior Fellow in 2015.

- Hari Srikanth was elected Fellow of the American Physical Society (APS) in 2014.

- George Nolas was elected Fellow of the American Physical Society (APS) in 2013.

- George Nolas was elected Fellow of the American Association for the Advancement of Science (AAAS) in 2012.

- Hari Srikanth was nominated as a Member of the IEEE Magnetics Society Administrative Committee. Election results due in October 2008.

- FML researcher Dr. Natalie Frey was selected with partial financial support from NSF to present her CIFM-affiliated research at the Gordon Research Conference on Magnetic Nanostructures (Aussois, France, Aug 31-Sept 8, 2008)

- Hari Srikanth is a member of the Program Committee and a Publication Editor for the 53rd Magnetism and Magnetic Materials (MMM) conference held in Austin, TX (Nov. 2008)

- Hari Srikanth, Scientific Committee Member, Symposium E: Magnetic materials at the nanoscale, 11th International Conference on Advanced Materials (ICAM 2009), Rio de Janeiro, Brazil (Sept 2009)

- Hari Srikanth co-organized the symposium on 'Functional oxide nanostructures and heterostructures" at the 2010 MRS Spring Meeting in April 2010 in San Francisco

- Hari Srikanth served as a Program Committee member and Publication Editor for the annual Magnetism and Magnetic Materials (MMM) conference held in Austin, TX in Nov. 2008. He continued to serve as a publication editor for the 2010 joint MMM/Intermag conference in January 2010 in Washington DC

- Hari Srikanth was an Invited Speaker, "Functional Magnetic Nanostructures" –Evening with a Scholar lecture to the Tampa Bay community leaders/entrepreneurs, November 6, 2009

- Hari Srikanth, Publication Chair and Steering Committee Member, 2011 MMM Conference, Scottsdale, AZ (November 2011)

- Hari Srikanth, Session Chair, Session AT: Magnetocaloric Materials I, joint MMM/INTERMAG conference, January 2010, Washington DC

- Hari Srikanth, Co-organizer of MRS 2010 Spring Meeting Symposium N, "Functional oxide nanostructures and heterostructures", April 2010, San Francisco, CA

- Hari Srikanth, Publications Editor of 11th Joint INTERMAG/MMM conference, Washington DC, January 2010

Students graduated:

15 CIFM students (14 of whom were funded from the CIFM grants) received graduate degrees including 10 Ph.D. degrees in Applied Physics and 5 Master's degrees in Physics. They are:

- Mr. Joshua Martin graduated with a Ph.D. degree in 2008
- Ms. Marienette Morales graduated with a M.S. degree in 2009
- Mr. Devajyoti Mukherjee graduated with a Ph. D. degree in 2010
- Mr. Gayan Dedigamuwa graduated with a Ph.D. degree in 2010
- Mr. Robert Hyde graduated with a Ph.D. degree in 2011
- Mr. Anurag Chaturvedi graduated with a Ph.D. degree in 2011
- Mr. Ted Wangensteen graduated with a Ph.D. degree in 2012
- Mr. Dino Ferizovic graduated with a Ph. D. degree in 2012
- Mr. Nicholas Bingham graduated with a Ph.D. degree in 2013.
- Ms. Kristen Stojak graduated with an M.S. degree in 2013
- Mr. Jason Rejman graduated with an M.S. degree in 2013
- Mr. Sayan Chandra graduated with a Ph.D. degree in 2013.
- Ms. Zohreh Nemati-Porshokouh was awarded an M.S. degree in 2014
- Mr. Jagannath Devakota graduated with a Ph.D. degree in 2015
- Mr. Vijayasankar Kalappatil was awarded an M.S. degree in 2015

CIFM students' awards/scholarships:

- Research Experience for Undergraduates (REU) students (Valery Ortiz Jimenez, David Torres, and Evelyn Vila) won *NSF-USF Travel Awards* to attend and present their research at the American Physical Society Meeting, Baltimore, MD, March 14-18, 2016

- Ms. Kristen Stojak, *NASA Florida Space Grant Consortium (FSGC) Award*, 2015

- Mr. Brian Casas, *GMAG-APS Student Travel Award*, the American Physical Society Meeting, San Antonio, TX, March 2-6, 2015

- Mr. Jagannath Devkota, *EMN Fall Meeting Best Poster Award*, Orlando, Florida, USA, November 22-25, 2014; *IEEE Magnetics Society Summer [School](#) Travel Award*, Rio de Janeiro, Brazil, August 10-16, 2014

- Dr. J. Alonso, *Best Poster Award*, The 59th Annual Conference on Magnetism and Magnetic Materials, Hawaii, USA, November 3-7, 2014

- Ms. Kristen Stojak, *59th Conference on Magnetism and Magnetic Materials (MMM) Travel Award,* Honolulu, Hawaii, USA, November 3 - 7, 2014

- Ph.D. student Jagannath Devkota received the GMAG-APS Student Travel Award to attend the American Physical Society Meeting, Baltimore, Maryland, March 18-22, 2013

- Undergraduate research student Alex Ruiz received the presidential graduate research fellowships for Ph.D. in Applied Physics from the University of California – Berkeley, Yale University, and Penn State University, 2013

- M.S. student Kristen Stojak and undergraduate student Alex Ruiz won the Best Poster Presentation Award at NanoFlorida conference, USF, Sept. 2012

- Ph.D. student Nicholas Bingham received the Travel Grant Award to attend the 1st Centennial of Superconductivity: Trends on Nanoscale Superconductivity and Magnetism International Workshop (June 28-July 1st, 2011), Cali, Colombia, USA; the Travel Grant Award to attend the 2nd Annual IEEE Magnetics Society Summer School (September 20-25, 2009), China

- Ph.D. student Paula Lampen received the NSF Travel Grant Award to attend the IEEE Magnetics Society Summer School (May 22-28, 2011), New Orleans, LA, USA

- Undergraduate research student Nicholas Laurita received the Ph.D. fellowship from Johns Hopkins University, 2011

- M.S. student Marienette Morales received financial support to attend the IEEE Magnetics Society summer school at UCCS, Colorado Springs in August 2008.

- M.S. student Marienette Morales completed an Industrial Practicum in Summer 2008 at SINMAT, Inc. in Gainesville, FL where she worked on ceramic nanoparticle slurries for tribological applications.

Impact of grant-funded research:

According to the Web of Science, the number of publications from this grant is higher than that from any other single grant in the history of the Physics Department at the University of South Florida. As of November 17, 2015 these publications have garnered 876 citations with a trajectory of increasing annual citations. The annual history of citations for publications from this grant at USF according to the Web of Science is indicated below:
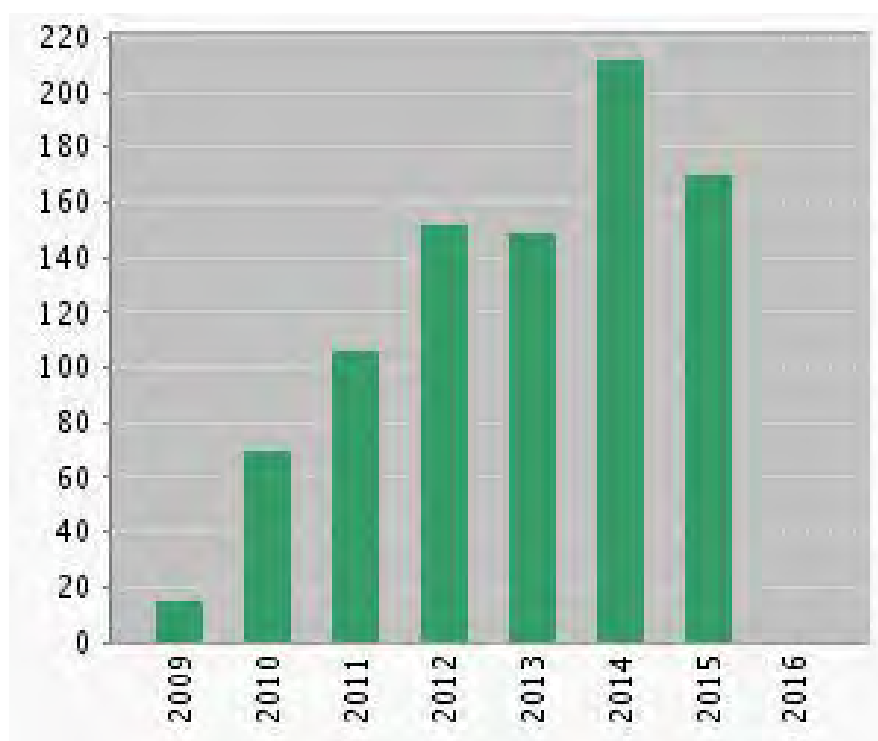
V. Conclusion

As previously described, the four remaining milestones were grouped into two Tasks as shown below:

Task I: Nanostructured materials for biomedical diagnostics and chemical sensing

1. Synthesis of PEG, Dextran coated nanoparticles and clusters for hyperthermia experiments and their structural and magnetic characterization.

2. Measurements and comparative analysis of specific absorption rates and AC power losses of ferrofluids for magnetic hyperthermia applications.

3. Magnetoimpedance measurements and sensing of biomolecules.

Task II: Formation and delivery of functionalized artificial platelets for rapid cessation of internal bleeding

4. Formation and delivery of functionalized artificial platelets for rapid cessation of internal bleeding.

As described in *Section II: Technical Description of Research* all of the milestones for the grant have been completed. In addition to the key research accomplishments outlined in Section III and the outcomes reported in Section IV, a major accomplishment of the grant has been to establish a multi-investigator Center for Integrated Functional Materials (CIFM) in the Physics Department at the University of South Florida (USF). CIFM is physically located in multiple laboratories on the fifth floor of the seven-story Interdisciplinary Sciences building at USF and provides an ongoing resource for the synthesis of novel materials using physical and chemical processes, and their characterization and development for multi-functional applications and devices. It is anticipated that this Center and associated researchers will continue to address the development of technologically significant materials for military and commercial applications well beyond the conclusion of this particular grant.

VI. References

(1) M. Shibayama and T. Tanaka, *Adv. Polym Sci.* **109**, 1 (1993).

(2) D. Denmark, D. Mukherjee, J. Bradley, S. Witanachchi, and P. Mukherjee, in *2014 MRS Fall Meeting Proceedings*, Boston, Massachusetts, 30 November–5 December 2014, edited by A. Lendlein (Materials Research Society, to be published)

(3) N. A. Peppas, P. Bures, W. Leobandung, and H. Ichikawa, *Eur. J. Pharm. Biopharm.* **50**, 27 (2000).

(4) F. Brandl, N. Hammer, T. Blunk, J. Tessmar, and A. Goepferich, *Biomacromolecules* **11**, 496 (2010).

(5) C. S. Satish, K. P. Satish, and H. G. Shivakumar, *Indian J. Pharm. Sci.* **68**, 133 (2006).

(6) F. Ganji and E. Vasheghani-Farahani, *Iran. Polym. J.* **18**, 63 (2009).

(7) H. G. Schild, *Prog. Polym. Sci.* **17**, 163 (1992).

(8) F. M. Winnik, *Macromolecules* **23**, 233 (1990).

(9) H. G. Schild and D. A. Tirrell, *J. Phys. Chem.* **94**, 4352 (1990).

(10) M. Babincová, V. Altanerová, C. Altaner, P. Cicmanec, and P. Babinec, *Medical Physics* **31**, 2219 (2004).

(11) A. Jordan, R. Scholz, P. Wust, H. Faehling, and R. Felix, *Journal of Magnetism and Magnetic Materials* **201**, 413 (1999).

(12) J. O. Martinez, B. S. Brown, N. Quattrocchi, M. Evangelopoulos, M. Ferrari, and E. Tasciotti, *Chin. Sci. Bull.* **57**, 3961 (2012).

(13) T. Y. Liu, S. H. Hu, D. M. Liu, S. Y. Chen, and I. W. Chen, *Nano Today* **4**, 52 (2009).

(14) D. Schmaljohann, *Adv. Drug Delivery Rev.* **58**, 1655 (2006).

(15) Q. A. Pankhurst, J. Connolly, S. K. Jones, and J. Dobson, *J. Phys. D: Appl. Phys.* **36**, R167 (2003).

(16) H. Khurshid, M. H. Phan, P. Mukherjee, and H. Srikanth, *Applied Phys Letters* **104**, 072407 (2014).

(17) H. Khurshid, W. Li, M.-H. Phan, P. Mukherjee, G. C. Hadjipanayis, and H. Srikanth, *Applied Physics Letters* **101**, 022403 (2012).

(18) C. L. Dennis and R. Ivkov, *Int. J. Hyperthermia* **29**, 715 (2013).

(19) WT Coffey and YP Kalmykov, *J. Appl. Phys.* **112**, 121301 (2012).

(20) L. D. Taylor and L. D. Cerankowski, *J. Polym. Sci., Pt. A: Polym. Chem.* **13**, 2551 (1975).

(21) C. Binns, editors B. Atkas and F. Mikailzade, (Springer, Berlin, 2013) pp.199-212.

(22) A. Zadrazil, V. Tokarova, and F. Stepanek, *Soft Matter* **8**, 1811 (2012).

(23) J. Alonso, H. Khurshid, V. Sankar, Z. Nemati, M. H. Phan, E. Garayo, and H. Srikanth, *J. of Appl. Phys.* **117**, 17D113 (2015).

(24) Z. Li, M. Kawashita, N. Araki, M. Mitsumori, M. Hiraoka, and M. Doi, *Materials Science and Engineering C* **30**, 990 (2010).

(25) Y. Xia, N. Burke, and H. Stover, *Macromolecules* **39**, 2275 (2006).

(26) H. G. Schild, M. Muthukumar, and D. Tirrell, *Macromolecules* **24**, 948 (1991).

(27) R. Freitag and G. Garret-Flaudy, *Langmuir* **18**, 3434 (2002).

(28) G. Vallejo-Fernandez, O. Whear, A. Roca, S. Hussain, J. Timmis, V. Patel, and K. O'Grady, *J. Phys. D: Appl. Phys.* **46**, 312001 (2013).

(29) D. Ortega and Q. A. Pankhurst, *Nanoscience* **1**, 60 (2013).

(30) R. Hergt, S. Dutz, R. Mueller, and M. Zeisberger, *J. Phys: Condens. Matter* **18**, S2919 (2006).

(31) D. Serantes, K. Simeonidis, M. Angelakeris, O. Chubykalo-Fesenko, M. Marciello, M. Morales, D. Baldomir, and C. Martinez-Boubeta, *J. Phys. Chem. C* **118**, 5927 (2014).

(32) Z. Ahmed, E. A. Gooding, K. V. Pimenov, L. Wang, and S. A. Asher, *J. Phys. Chem. B* **113**, 4248 (2009).

(33) C. Binns, "Magnetic nanoparticle hyperthermia treatment of tumors." Nanostructured Materials for Magnetoelectronics. Springer Berlin Heidelberg, 197-215 (2013).

(34) T. Y. Liu, S.H. Hu, D. M. Liu, S. Y. Chen, and I. W. Chen, Biomedical nanoparticle carriers with combined thermal and magnetic responses, Nano Today, 2009 4(1), 52-65.

(35) J. O. Martinez, B. S. Brown, N. Quattrocchi, M. Evangelopoulos, M. Ferrari, and E. Tasciotti, Multifunctional to multistage delivery systems: The evolution of nanoparticles for biomedical purposes, Chin. Sci. Bull., 2012, 57(31), 3961-3971.

(36) I. Brigger, C. Dupernet, and P. Couvreur, Nanoparticles in cancer therapy and diagnosis, Adv. Drug Deliv. Rev., 2002, 54(5), 631-651.

(37) M. Hamidi, A. Azadi, and P. Rafiei, Hydrogel nanoparticles in drug delivery, Adv. Drug Deliv. Rev., 2008, 60(15), 1638-1649.

(38) J. Panyam and V. Labhasetwar, Biodegradable nanoparticles for drug and gene delivery to cells and tissue, Adv. Drug Deliv. Rev., 2003, 55(3), 329-347.

(39) S. M. Moghimi, A. C. Hunter, and J. C. Murray, Long-circulating and target-specific nanoparticles: theory to practice, Pharmacol. Rev., 2001, 53(2), 283-318.

(40) P. R. Lockman, R. J. Mumper, M. A. Khan, D. D. Allen, Drug Dev. Ind. Pharm., Nanoparticle technology for drug delivery across the blood-brain barrier, 2002, 28(1), 1-13.

(41) K. H. Min, K. Park, Y. S. Kim, S. M. Bae, S. Lee, H. G. Jo, R. W. Park, I. S. Kim, S. Y. Jeong, K. Kim, I. C. Kwon, Hydrophobically modified glycol chitosan nanoparticles-encapsulated camptothecin enhance the drug stability and tumor targeting in cancer therapy, J. Control Release, 2008, 127(3), 208-218.

(42) K. Cho, X. Wang, S. Nie, Z. G. Chen, and D. M. Shin, Therapeutic nanoparticles for drug delivery in cancer, Clin. Cancer Res., 2008, 14(5), 1310-1316.

(43) A. Ragusa, I. García, and S. Penadés, Nanoparticles as nonviral gene delivery vectors, IEEE Trans. Nanobioscience, 2007, 6(4), 319-330.

(44) J. D. Kingsley, H. Dou, J. Morehead, B. Rabinow, H. E. Gendelman, and C. J. Destache, Nanotechnology: A focus on nanoparticles as a drug delivery system, J. Neuroimmune Pharmacol., 2006, 1(3), 340-350.

(45) M. Nahar, T. Dutta, S. Murugesan, A. Asthana, D. Mishra, V. Rajkumar, M. Tare, S. Saraf, and N. K. Jain, Functional polymeric nanoparticles: an efficient and promising tool for active delivery of bioactives, Crit. Rev. Ther. Drug Carrier Syst., 2006, 23(4), 259-318.

(46) Q. A. Pankhurst, J. Connolly, S. K. Jones, and J. Dobson, Applications of magnetic nanoparticles in biomedicine, Journal of Physics D: Applied Physics, 2003, 36(13), R167-R181

(47) Q. A. Pankhurst, J. Connolly, S. K. Jones, and J. Dobson, Progress in applications of magnetic nanoparticles in biomedicine, J. Phys. D: Appl. Phys. 2009, 42, 224001

(48) M. Shibayama and T. Tanaka, Volume phase transition and related phenomena of polymer gels Adv. in Polym Sci.,1993, 109, 1-62.

(49) D. J. Denmark, D. Mukherjee, J. Bradley, S. Witanachchi, and P. Mukherjee, Systematic study on the remote triggering of thermoresponsive hydrogels using RF heating of Fe3O4 nanoparticles, Materials Research Society Symposium Proceedings, 2015, 1718, 1718-b04-30.

(50) N. A. Peppas, P. Bures, W. Leobandung, and H. Ichikawa, Hydrogel in pharmaceutical formulations, Eur. J. Pharm. Biopharm., 2000, 50(1), 27-46. F. Brandl, N. Hammer, T. Blunk, J. Tessmar, and A. Goepferich, Biodegradable hydrogels for time-controlled release of tethered peptides or proteins, Biomacromolecules, 2010, 11(2), 496-504.

(51) C. S. Satish, K. P. Satish, and H. G. Shivakumar, Hydrogels as controlled drug delivery systems: Synthesis, crosslinking, water and drug transport mechanism, Indian J. Pharm. Sci., 2006, 68(2), 133-140.

(52) F. Ganji and E. Vasheghani-Farahani, Hydrogels in controlled drug delivery systems, Iran. Polym. J., 2009, 18(1), 63-88].

(53) H. G. Schild, Poly(N-isopropylacrylamide: Experiment, theory, and application, Prog. Polym. Sci., 1992, 17(2), 163-249.

(54) F. M. Winnik, Fluorescence studies of aqueous solutions of poly(N-isopropylacrylamide) below and above their LCST, Macromolecules, 1990, 23(1), 233-242.

(55) H. G. Schild and D. A. Tirrell, Microcalorimetric detection of lower critical solution temperatures in aqueous polymer solutions, J. Phys. Chem., 1990, 94(10), 4352-4356.

(56) J. Carrey, B. Mehdaoui, and M. Respaud, Simple models for dynamic hysteresis loop calculations of magnetic single-domain nanoparticles: Application to magnetic hyperthermia optimization. Journal of Applied Physics, 2011, 109(8), 083921.

(57) M. Babincová, V. Altanerová, C. Altaner, P. Cicmanec, and P. Babinec, In vivo heating of magnetic nanoparticles in alternating magnetic field, Medical Physics, 2004, 31(8), 2219-2221

(58) A. Jordan, R. Scholz, P. Wust, H. Faehling, and R. Felix, Magnetic Fluid Hyperthermia (MFH): Cancer treatment with AC magnetic field induced excitation of biocompatible superparamagnetic nanoparticles, Journal of Magnetism and Magnetic Materials, 1999, 201(1), 413-419

(59) D. Ortega and Q. Pankhurst, "Magnetic hyperthermia," in Nanoscience: Volume 1: Nanostructures through Chemistry, Cambridge, Royal Society of Chemistry, 60 (2013)

(60) C. Binns, "Magnetic Nanoparticle Hyperthermia Treatment of Tumours," in Nanostructured Materials for Magnetoelectronics, Berlin, Springer-Verlag, 197 (2013)

(61) A. K. Gupta, and M. Gupta, Synthesis and surface engineering of iron oxide nanoparticles for biomedical applications, Biomaterials, 2005, 26(18), 3995-4021.

(62) T. Neuberger, B. Schopf, H. Hofmann, M. Hoffmann, and B. von Rechenberg, Superparamagnetic nanoparticles for biomedical applications: possibilities and limitations of a new drug delivery system, J. Magn. and Magn. Mat., 2005, 293(1), 483-496.

(63) M. Mahmoudi, S. Sant, B. Wang, S. Laurent, and T. Sen. "Superparamagnetic iron oxide nanoparticles (SPIONs): development, surface modification and applications in chemotherapy." Advanced drug delivery reviews 2011, 63, no. 1, 24-46.

(64) C. L. Dennis and R. Ivkov, Physics of heat generation using magnetic nanoparticles for hyperthermia, Int. J. Hyperthermia, 2013, 29(8), 715-729

(65) A. Zadrazil, V. Tokarova, and F. Stepanek, Remotely triggered release of composite hydrogel sponges, Soft Matter, 2012, 8(6), 1811-1816.

(66) J. Cejková, V. Tokárová, A. Pittermannová, and F. Stepánek, Remotely controllable microcapsules for site-specific delivery of a chemical payload, http://www.iros2011.org/WorkshopsAndTutorialsProceedings/SW9/iros_11_sw9_17_final.pdf

(67) K. Simeonidis, C. Martinez-Boubeta, Ll. Balcells, C. Monty, G. Stavropoulos, M. Mitrakas, A. Matsakidou, G. Vourlias and M. Angelakeris, J. Appl. Phys., 2013, 114(10), 103904.

(68) Z. Ahmed, E. A. Gooding, K. V. Pimenov, L. Wang, and S. A. Asher, UV resonance Raman determination of molecular mechanism of poly(N-isopropylacrylamide) volume phase transition, J. Phys. Chem. B, 2009, 113(13), 4248-4256

(69) I. Andreu, E. Natividad, L. Solozábal, O. Roubeau, Nano-objects for Addressing the Control of Nanoparticle Arrangement and Performance in Magnetic Hyperthermia, ACS Nano 2015, 9, 1408.

(70) Y. Xia, N. Burke, and H. Stover, End group effect on the thermal response of narrow disperse poly(N-isopropylacrylamide) prepared by atom transfer radical polymerization, Macromolecules, 2006, 39(6), 2275-2283.

(71) R. Freitag and G. Garret-Flaudy, Salt effects on the thermoprecipitation of poly(N-isopropylacrylamide) oligomers from aqueous solution, Langmuir, 2002, 18(9), 3434-3440

(72) B. W. Garner, T. Cai, S. Ghosh, Z. Hu, and A. Neogi, Refractive index change due to volume-phase transition in polyacrylamide gel nanospheres for optoelectronics and bio-photonics, Applied Physics Express, 2009, 2(5), 057001.